Acta Metallurgica Sinica (English Letters)
https://doi.org/10.1007/s40195-024-01758-1

Iron-Based Metal Matrix Composite: A Critical Review on the Microstructural Design, Fabrication Processes, and Mechanical Properties

Sai Chen[1] · Shuangjie Chu[1,2] · Bo Mao[1]

Received: 3 March 2024 / Revised: 19 April 2024 / Accepted: 29 April 2024
© The Chinese Society for Metals (CSM) and Springer-Verlag GmbH Germany, part of Springer Nature 2024

Abstract
Iron-based metal matrix composites (IMMCs) have attracted significant research attention due to their high specific stiffness and strength, making them potentially suitable for various engineering applications. Microstructural design, including the selection of reinforcement and matrix phases, the reinforcement volume fraction, and the interface issues are essential factors determining the engineering performance of IMMCs. A variety of fabrication methods have been developed to manufacture IMMCs in recent years. This paper reviews the recent advances and development of IMMCs with particular focus on microstructure design, fabrication methods, and their engineering performance. The microstructure design issues of IMMC are firstly discussed, including the reinforcement and matrix phase selection criteria, interface geometry and characteristics, and the bonding mechanism. The fabrication methods, including liquid state, solid state, and gas-mixing processing are comprehensively reviewed and compared. The engineering performance of IMMCs in terms of elastic modulus, hardness and wear resistance, tensile and fracture behavior is reviewed. Finally, the current challenges of the IMMCs are highlighted, followed by the discussion and outlook of the future research directions of IMMCs.

Keywords Iron-based metal matrix composites · Microstructure · Fabrication methods · Mechanical properties

1 Introduction

Iron and steels are the most widely utilized structural materials in human society due to their wide spectrum of properties, low manufacturing cost, and excellent recyclability [1]. However, traditional steels are substantially replaced by lightweight metallic materials with higher specific strength due to the increasing demand for saving weight in engineering applications [2]. The specific strength of steels can be increased significantly by advanced alloying [3] and thermal–mechanical processing techniques [4]. However, those strategies have a limited effect on improving the elastic modulus of steel, which has been considered a critical design criterion. Embedding the ceramic phases to the steel matrix is one of the most efficient approaches to enhance both the specific stiffness and strength of steel [5, 6]. In this regard, iron-based metal-matrix matrix composites (IMMCs), also known as high modulus steels, have been developed in recent years to meet the critical demands of steel industries [7].

The incorporation of low-density, high-stiffness, and high-strength reinforcing particles into the matrix has not only reduced material density but also elevated its elastic modulus, hardness, wear resistance, and high-temperature performance [8, 9]. For this reason, IMMCs have attracted extensive research attention in both academia and industry in recent decades. Figure 1 depicts a few typical examples of their current applications and typical fabrication methods. High strength non-metallic materials, such as ceramic powders, fibers, and 2-D materials can be introduced into the iron matrix through plenty of fabrication approaches. Due to the various choices of reinforcement and matrix phases, the resulting high strength-to-weight ratio, enhanced mechanical and thermal properties over conventional materials and

Available online at http://link.springer.com/journal/40195.

✉ Shuangjie Chu
sjchu@baosteel.com

✉ Bo Mao
bmao@sjtu.edu.cn

1 School of Materials Science and Engineering, Shanghai Jiao Tong University, Shanghai 200240, China

2 Baoshan Iron and Steel Cooperation Limited, Shanghai 201900, China

Published online: 12 September 2024

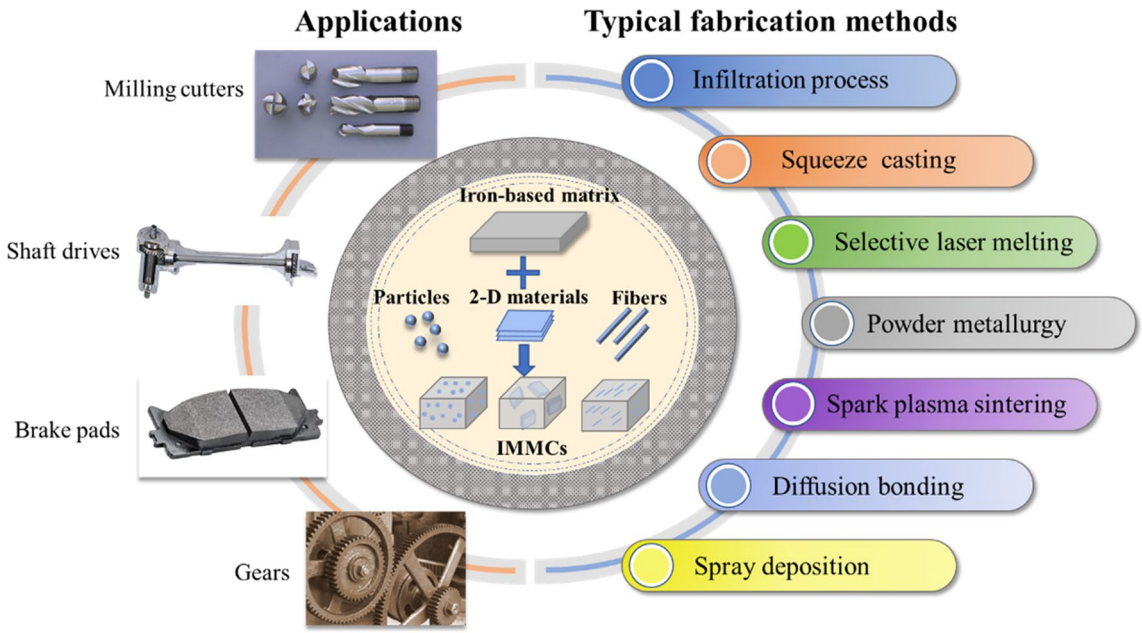

Fig. 1 Applications, microstructural design, and typical manufacturing processes of IMMCs

the other metal matrix composites (MMCs), make IMMCs very attractive in a variety of applications. Currently, the most widely used are IMMC reinforced by TiC particles, exemplified by trademarks like Ferro-TiC, Alloy-TiC, and Ferro-Titanit. IMMCs serve as wear-resistant parts and high-temperature structural materials, such as gears, bushings, and bearings, exhibiting significantly superior performance compared to existing tool steels. In addition, IMMCs can also be utilized in aerospace applications, such as structural components and aircraft engine parts to enhance strength and reduce weight. Furthermore, the in situ synthesized NbC and V_2C nano-particle-reinforced IMMC, has demonstrated an 18% increase in elastic limit compared to normal spring steel and been deployed in practical applications. Table 1 summarizes some milestone inventions of IMMCs and their aimed applications. IMMCs exhibit certain unique advantages and characteristics in comparison to the other MMCs, especially in specific strength, specific modulus, high-temperature resistance, and wear resistance. However, the preparation, microstructure, and properties of IMMCs show significant distinctions from MMCs as well. The melting point of iron has a certain impact on the difficulty of preparation, especially in cases involving melting processing and heat treatment. Nevertheless, IMMCs retain the advantages of steel in terms of microstructure. For example, the complex multiphase microstructure enables IMMCs to possess both high strength and good plasticity and toughness simultaneously compared to other MMCs. Additionally, the failure of IMMC is not attributed to interfacial debonding but rather to particle fracture under both tensile and shear loading. This failure mechanism markedly differs from that of MMCs, where the primary causes of fracture failure are particles cracking and interfacial debonding between the reinforcement and matrix [10, 11]. This disparity is primarily ascribed to the heightened interfacial strength of IMMC, preventing crack initiation at interfaces [12]. The fatigue failure mechanism of IMMCs is of paramount importance for the durability of mechanical structures. These distinctive features may render IMMCs more competitive in specific application domains. However, the selection of materials is typically contingent upon specific application requirements, with different materials showcasing more pronounced advantages in various facets.

A variety of methods have been developed in recent years to fabricate IMMCs based on the state in which the reinforcements were formed [17]. Typical fabrication methods can be classified into three categories: liquid-state methods, solid-state methods, and gas-mixing methods. Liquid-state methods involve infiltration process, squeeze casting, liquid phase sintering, and selective laser melting. Solid-state methods include powder metallurgy, spark plasma sintering, self-propagating high-temperature synthesis, diffusion bonding, exothermic dispersion, and mechanical alloying. The most common gas-mixing procedures used to produce IMMCs are vapor–liquid-solid and spray deposition [18]. Extensive studies have shown that IMMCs can yield high levels of mechanical and physical properties due to novel microstructure design and a variety of processing routines. Guan et al. [19] fabricated polycarbosilane (PCS)/316 L steel composites via spark plasma sintering. The yield strength

Table 1 Development and application of IMMCs

Reinforcement	Microstructure	Targeted properties	Aimed applications	Years	Developers and references
TiB_2	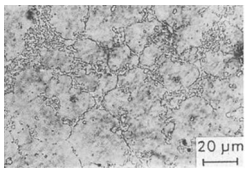	High-temperature stability and hot compressive yield strength	Cutting tool	1993	Saha et al. [13]
Al_2O_3-fiber	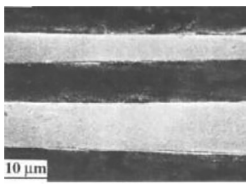	Good conductivity and dynamic shear modulus	Coil springs	1998	Masahiro Inoue et al. [14]
2-D materials	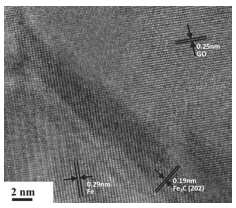	High fatigue life and fracture toughness	The mining industry and railway switches	2014	Lin et al. [15]
ZrO_2	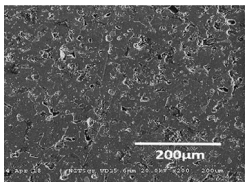	Excellent wear resistance	Bearing materials	2021	Parveez et al. [16]

(YS) and ultimate tensile strength (UTS) of the composite were 526 ± 9 and 898 ± 9 MPa, representing 49.4% and 38.6% improvement compared with unreinforced materials, respectively. Moreover, it is noteworthy that the addition of ceramic particles plays a beneficial role in refining the microstructure of the iron matrix. Song et al. [20] investigated the microstructure and mechanical property of Cr_3C_2 reinforced IMMCs via selective laser melting (SLM). Due to the rapid cooling rate during the solidification of SLM, extremely fine grains were obtained throughout the composites. The ultimate tensile strength (UTS) could reach up to 1158 MPa. Grairia et al. [21] studied the wear resistance of WC-Fe composites (85 Fe-5 Ni-10 WC) manufactured by powder metallurgy. The COF (coefficient of friction) of samples increases as the number of wear particles rapidly increases. The COF is 1.15 ± 0.02 when the load/sliding speed is 5 N/5 cm/s and sample against aluminum balls. Zhong et al. [22] investigated the abrasive wear resistance of IMMCs reinforced with V_8C_7, which was manufactured via infiltration casting. It was found that the wear resistance value was 21.2 times greater than gray cast iron under 20 N load, when the volume fraction of the reinforcement particles achieved 24%.

Due to their scientific significance and practical applications, several reviews in literature focused on the processing and mechanical properties of IMMCs. Earlier review published by Parashivamurthy et al. [23] summarized the effect of processing parameters on the TiC reinforced steel composite. Das et al. [24] reviewed 6 different routes for the synthesizing Fe–TiC IMMCs and compared the advantages and disadvantages of each manufacturing processes. Akhtar [25] critically reviewed the basic manufacturing processes of IMMCs as well as their microstructure and mechanical properties, and described the reinforcements for the IMMCs with superior properties from a thermodynamic perspective. In recent years, a variety of innovative manufacturing and processing techniques, such as electro pulsing-assisted flash sintering [26], have evolved to optimize and microstructure and mechanical properties of IMMCs. Moreover, some novel reinforcement phases, such as 2D materials and fibers, have been explored to incorporate into iron matrix, which resulted in superior engineering performance to those of traditional IMMCs. However, a complete summary on the state-of-the-art of the microstructural design, manufacturing processes, and mechanical properties of IMMCs is still lacking. Therefore, it is of great importance to have a comprehensive review of the current advances of the research of IMMCs.

The objective of this paper is to present a comprehensive review of the current stage of the development of IMMCs. The microstructure design issues of IMMC are

first discussed, including the reinforcement and matrix phase selection, interface geometry and characteristics, and the bonding mechanism. Secondly, a variety of fabrication methods are comprehensively reviewed and compared, including liquid state, solid state, and gas-mixing processing. Then, the mechanical properties in terms of elastic modulus, hardness and wear resistance, tensile and fracture behavior are reviewed. Finally, the future directions of the IMMCs are highlighted, followed by the discussion and outlook of the current challenges associated with the fabrication and applications of IMMCs.

2 Microstructural Design of IMMC

The microstructural design of IMMCs is a critical aspect that significantly influences the mechanical, thermal, and other properties of the composite. The microstructure of IMMCs consists of reinforcement, interfaces, and iron matrix. The variety of the versatile matrix phases and reinforcements in IMMC enables the extensive choice of microstructural design. The microstructural design of IMMC is essential for producing valuable composites with good performance. Figure 2 represents various types of reinforcements and matrix of IMMCs, demonstrating how they can be arranged in different configurations to modify the characteristics of IMMCs, which also highlights the adaptability and tunability of IMMCs [27]. In addition, the microstructural design strategy of IMMCs is discussed in terms of reinforcement and matrix phases in this section. Moreover, the geometry and reaction of the interface between reinforcement and matrix are presented.

2.1 Reinforcement Phases

It is notable that the specific modulus of well applied structural materials, from magnesium alloys to steels, is around 26 GPa cm^3/g and almost identical. However, the specific modulus of some ceramic particles and 2-D materials could rich to a value as high as above 100 GPa cm^3/g, allowing the modification and optimization of physical and mechanical properties of steel matrix in a wide range. Oxides, intermetallic compounds, carbides, borides, and some 2-D materials have been exploited to improve the engineering performance of IMMCs. Usually, the choice of reinforcement (particles, fibers, etc.) significantly impacts the microstructure. Table 2 summarizes the physical and mechanical properties of the commonly studied reinforcement phases. It can be seen that most of the reinforcement phases have a lower density and higher elastic modulus and melting point than those of iron matrix. These characteristics allows the strengthening and lightening of IMMCs in a wide range. The reinforcement phase can be classified into three categories, i.e., particles, fibers, and 2-D materials based on the morphologies it presents in the IMMCs.

2.1.1 Particle Reinforcement Phases

Ceramic particles, including oxides (Al_2O_3, Zr_2O_3, Cr_2O_3, etc.), nitrides (TiN, BN, etc.), carbides (SiC, B_4C, TiC, WC, VC, etc.), borides (TiB_2 and ZrB_2) and even complex ceramic such as zirconia toughened alumina (ZTA), are the most widely utilized reinforcement phases in IMMCs owing to their low cost, high specific modulus, and high hardness [9, 44]. The volume percentage of the reinforcement can vary from very low to nearly 50%. Achieving a

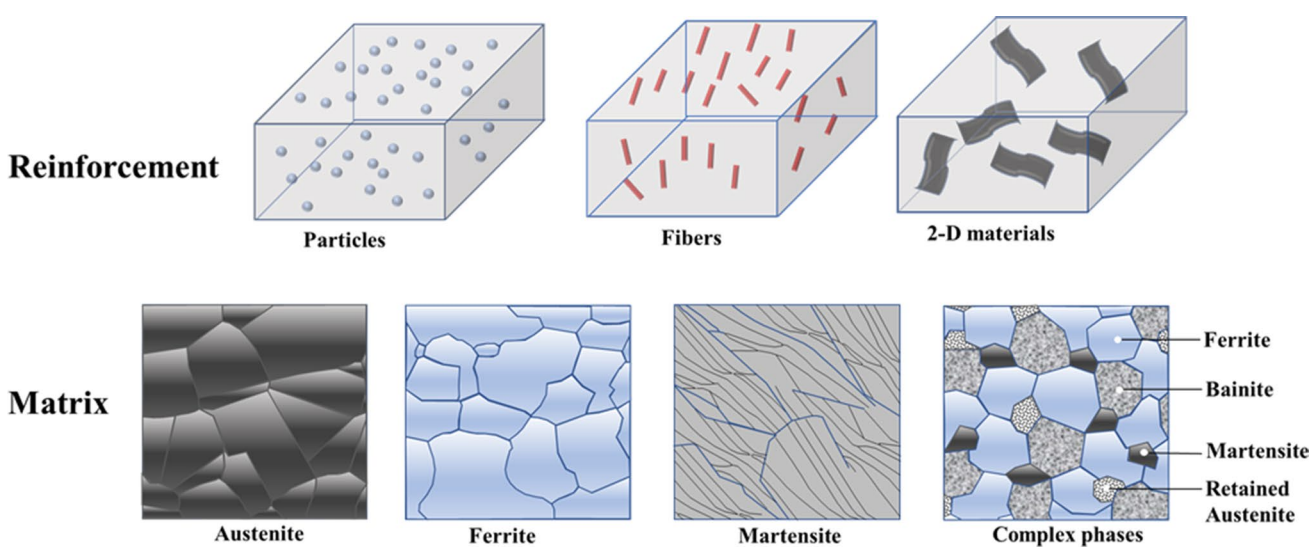

Fig. 2 A schematic illustration showing the microstructural design of IMMCs

Table 2 Summary of the commonly used reinforcement phases of IMMCs

Type	Reinforcement	Structure or crystal structure	Density, ρ (g/cm^3)	Elastic modulus, *E* (GPa)	Melting point (°C)	*E*/ρ ratio (GPa cm^3/g)	References
Oxide	Al_2O_3	Trigonal	3.98	370	2063	92.96	[28]
	ZrO_2	Monoclinic	5.68	210	2715	36.97	[16]
	SiO_2	Tetrahedral	2.648	75	1716	28.32	[29]
Nitride	BN	Hexagonal	2.1	865	2973	411.9	[30]
	TiN	Cubic	5.21	251	2950	48.18	[31]
Carbide	SiC	Tetrahedron	3.21	401	2730	124.92	[32]
	B_4C	Rhombohedra	2.52	460	2450	182.54	[33]
	WC	Hexagonal	15.6	650	2870	41.67	[34]
	VC	Cubic	5.77	380	1910	65.86	[35]
	Cr_3C_2	Orthorhombic	6.68	228	1890	34.13	[36]
	TiC	Cubic	4.93	400	3067	81.14	[37]
Boride	TiB_2	Hexagonal	4.51	565	2900	125.28	[38]
	ZrB_2	Hexagonal	6.085	~550	~3246	~90.39	[39]
Composite	Zirconia toughened alumina (ZTA)	Tetragonal	4.1–4.38	400	1980	91.32–97.56	[40]
Fibers	E-glass fiber	Weave	2.58	76	1135	29.46	[41]
	Kevlar fiber	Several repeating inter-chain	1.4	131	560	93.57	
	Carbon fiber	Long, tightly interlocked chains of carbon atoms	1.75–1.93	228	3652–3697	118.13–130.29	[42]
2-D materials	Graphene	Hexagonal	2.09–2.33	1000	3652	~454.55	[15]
	Carbon nanotube	Hexagonal	1.3–1.4	1000	3550	714.29–769.23	[43]

uniform distribution of reinforcement throughout the matrix is essential. Additionally, controlling the size, shape, and orientation of the reinforcement, whether aligned or random, can affect the anisotropic behavior of the IMMCs. Aparicio et al. [45] investigated the morphology, size, and dispersion of TiB_2 particles produced in situ from Fe-Ti-B based melts, as well as their chemical composition, crystal structure, and mechanical properties are studied in detail. In addition, an alloying except Ni reduced the size of the eutectic TiB_2 particles, although their aspect remained unaffected.

Self-propagating high-temperature synthesis technique was used to fabricate ductile austenitic steel reinforced with 23 wt% Al_2O_3 particles through thermite reaction in Fe_2O_3-Cr_2O_3–NiO–Al–Fe reaction system [46]. The reaction can be described as: $x\,Fe + (0.66 - x/2)\,Fe_2O_3 + 0.175\,Cr_2O_3 + 0.135\,NiO + (1.760–x)\,Al = 1.32\,Fe + 0.35\,Cr + 0.135\,Ni + (0.88 - x/2)\,Al_2O_3$. The results of the energy dispersive spectroscopy analysis revealed a uniform distribution of Al_2O_3 particles in the steel matrix, which were trapped in the melt during matrix material solidification. Manowar et al. [47] fabricated TiN particles reinforced 316 stainless steel through laser sintering technique in different atmosphere (nitrogen and argon). The TiN particles are uniformly dispersed in different layers of matrix due to the layer-by-layer deposition process, and fine gaps are not found between TiN and SS316. The addition of hard TiN increased the wear resistance of composites, the coefficient of friction reaches 0.54 under the TiN content of 6 wt%.

Liang et al. [48] developed austenite manganese steel-matrix composites reinforced with in situ TiC/TiB_2 particles using SHS and casting techniques in a Cu-Ti-B_4C system. Enhanced carbon diffusion and influenced particle size and wear resistance, which was optimal at a wear rate of 0.92 10^{-10} m^3/m with 30 wt% Cu, promoting uniform particle distribution. The thermal properties of the particles significantly affected the composites' performance. Song et al. [20] chosen Cr_3O_2 which has a low melting point and close thermal expansion coefficient to iron matrix as the particle reinforcement to reinforce iron matrix. Those characteristics enables the uniform distribution and structure integrity of the composite fabricated. Table 3 illustrates the crystal structures of various reinforcing phases, as well as the IMMC prepared through different methods, showcasing their microstructure and properties.

Table 3 Typical examples of IMMCs in terms of their reinforcement phases, fabrication methods, and microstructure

IMMC type	TiB_2 reinforced IMMC [49]	Al_2O_3 reinforced SS304 [46]	TiN reinforced SS316 IMMC [47]	TaC reinforced IMMC [50]
Reinforcement	TiB_2	Al_2O_3	TiN	TaC
Crystal structure of the reinforcement	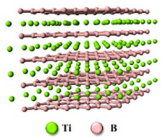	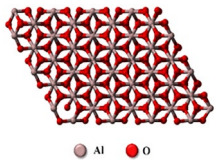	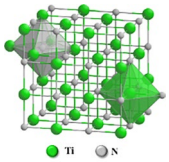	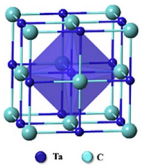
Fabrication methods	Eutectic solidification	Self-propagating high temperature synthesis process	Laser sintering technique	In situ solid-phase diffusion
Microstructure	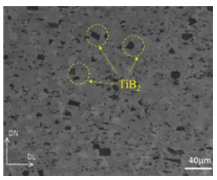	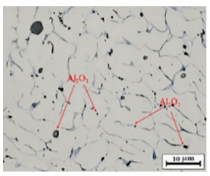	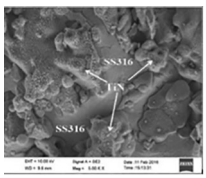	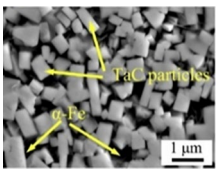
Properties	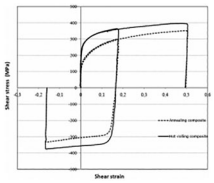	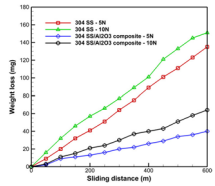	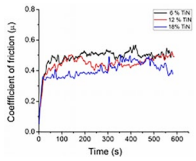	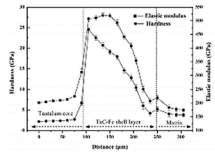

2.1.2 Fiber Reinforcement Phases

Particles-reinforced IMMC has many advantages, but also faces some problems such as poor fatigue resistance and interfacial bond strength. Regarding this, fiber-reinforced IMMC often has high specific strength and stiffness. Any materials (polymers, metals, or ceramics) can transform into fibrous form. Fibers exhibit distinctive attributes (remarkable flexibility and superior strength) primarily derived from their relatively small cross section and large aspect ratio. Fiber-reinforced MMC which contains either continuous [51] or discontinuous [52]. The bonding of fiber reinforcements and matrix is an essential factor in the transmission of stresses between the matrix and fiber [53]. As the reinforcement phases of IMMCs, fiber provides the major strength [53, 54]. The final properties of fiber reinforced IMMCs are determined by fiber characteristics such as orientation [42], length [55], and distribution [56]. Currently, the liquid state technique is mostly employed to manufacture fiber reinforced MMCs [57]. The details on the definition, classification, and benefits of fiber reinforced IMMCs are discussed in this section.

Sueyoshi et al. [58] studied continuous ceramic fiber-reinforced iron composites using hot isostatic pressing (HIPing), finding that alumina fibers are aligned and uniformly dispersed based on their diameter and the particle size of the iron powder. Optimal conditions were identified with a particle size of 9 μm for 20 μm fibers. Further studies [59] on discontinuous alumina fiber-reinforced steel revealed nearly full density and minimal porosity, influenced by particle diameter and fiber volume fraction. Sakamoto et al. [60] utilized an infiltration process to develop Al_2O_3 short fiber reinforced hypo-eutectic and hyper-eutectic 25 Cr cast irons with varying fiber volume fractions. Microstructure observations (Fig. 3a and b) revealed a significant refinement in the composite specimens due to the presence of Al_2O_3 fibers. Additionally, the composite specimens exhibited higher hardness than their unreinforced counterparts, which can mainly be attributed to the hard Al_2O_3 fibers. The morphologies of the worn composite specimens were shown in Fig. 3c and d. In the hypo-eutectic specimen (Fig. 3c), the presence of Al_2O_3 fibers that protruded from the worn surface played a crucial role in wear resistance. The even distribution of these fibers also reduced the mean free path in the softer matrix and protected it from abrasion. In contrast, in the hyper-eutectic composite (Fig. 3d), the abrasion resistance was mainly controlled by the coarse primary carbides, with the contribution of Al_2O_3 fibers being limited by their low volume fraction and relatively smaller size. Figure 3e depicts the results of the abrasion tests, which demonstrated that the presence of Al_2O_3 fibers significantly improved the wear resistance of hypo-eutectic high Cr cast iron, reducing the wear rate to only 38% of that of the unreinforced alloy. However, for the hyper-eutectic composite, only a small improvement in abrasion resistance was observed. Furthermore, a higher content of Al_2O_3 fibers does not necessarily result

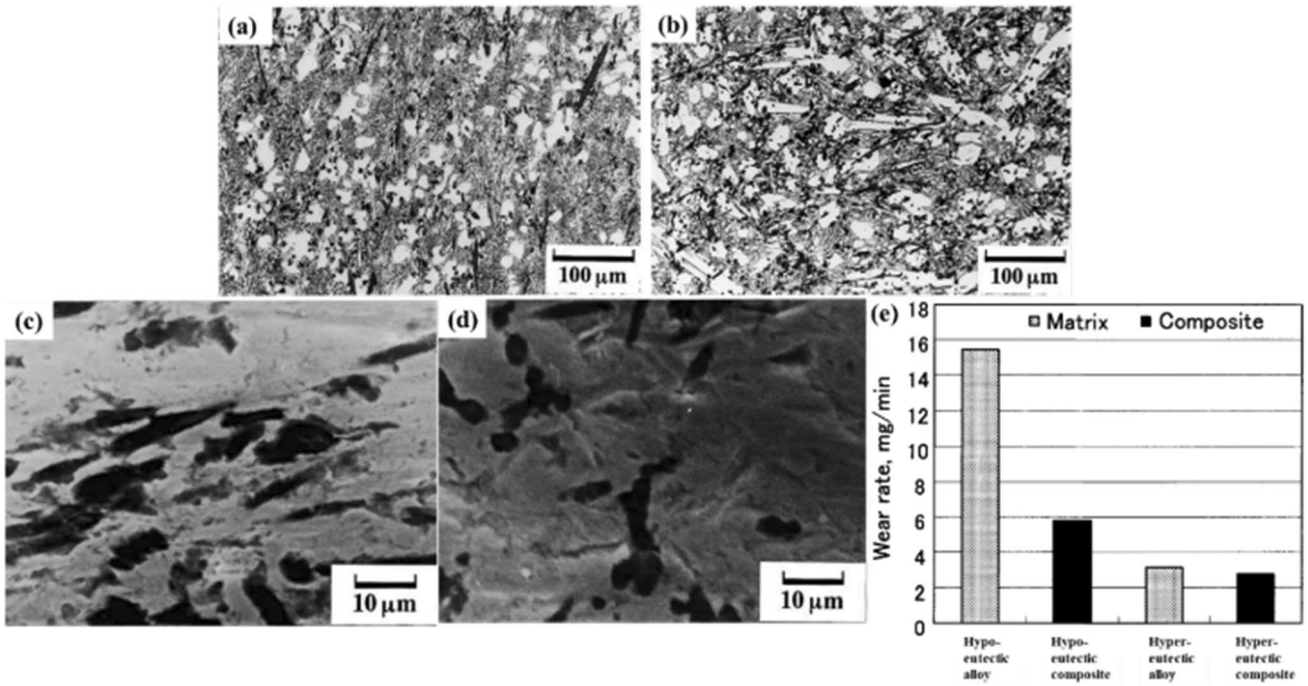

Fig. 3 Microstructures of **a** hypo-eutectic 25Cr composite and **b** hyper-eutectic 25Cr composite. SEM images of worn surface of composite specimens after abrasion test: **c** hypo-eutectic composite, **d** hyper-eutectic composite. **e** Wear rates of the alloy and composite specimens after abrasion test [60]

in improved wear resistance. At 923 K, the hypo-eutectic composite with a fiber volume fraction of 20% exhibited the smallest wear rate, and a decrease in wear rate with increasing fiber volume content was demonstrated in the hyper-eutectic composites. In conclusion, the presence of Al_2O_3 fibers in high Cr cast irons is beneficial for improving the abrasion resistance.

2.1.3 2-D Materials as Reinforcement Phases

Two-dimensional (2-D) materials as a promising reinforcement has been explored to fabricate IMMCs for their great potential [61]. Due to their unique physical and mechanical characteristics, graphene can be employed in a variety of applications, including as a reinforcement material in IMMCs [62, 63]. Many studies have revealed that the strength of composites increases by adding graphene. However, the agglomeration of graphene affects the mechanical properties of IMMCs negatively [64].

Zhao et al. [65] studied Fe/graphene oxide (GO) composites, observing that GO distribution within the iron matrix promoted uniform biodegradation rates and enhanced strength due to micro-galvanic corrosion. The corrosion rate matched pure iron at 0.38 mm/year. Wang et al. [66] found that graphene orientation in Fe composites significantly affects their mechanical properties, with strongly bonded $(11\bar{2})$ graphene increasing yield stress to 991 MPa, compared to a weaker bond one $\left(1\bar{1}0\right)$ 520 MPa. Mandal et al. [67] produced graphene-reinforced 316 L stainless steel via selective laser melting, resulting in a homogeneous microstructure without notable porosity. The microstructure featured cellular and columnar sub-grains organized as colonies. Adding just 0.2 wt% graphene significantly enhanced mechanical properties, increasing yield strength and hardness by up to 70% (502 to 850 MPa) and 25% (194 to 245 HV), respectively. Essa et al. [68] investigated the tribological behavior of Al_2O_3/graphene reinforced M50 steel. The addition of Al_2O_3/graphene to M50 steel efficiently reduces the density of composites (from 7.27 to 6.11 g/cm^3) and hardness (from 468.85 to 387.32 HV) when 15 wt% alumina and graphene are added. Besides, the thermomechanical stability of composites was enhanced due to the high thermal stability of Al_2O_3/graphene.

Lin et al. [15] investigated graphene oxides (GOs) reinforced IMMCs which were fabricated by selective laser sintering. The scanning electron microscopy (SEM) image of GOs in the composites after laser sintering is illustrated in Fig. 4a, where it can be seen that the GOs are surrounded by matrix and the continuous shape of GO. Figure 4b shows the comparison of surface microhardness of samples with different treatments. The surface hardness was significantly improved with laser sintering GO into iron matrix. It is shown in Fig. 4c that cracks propagate along with the

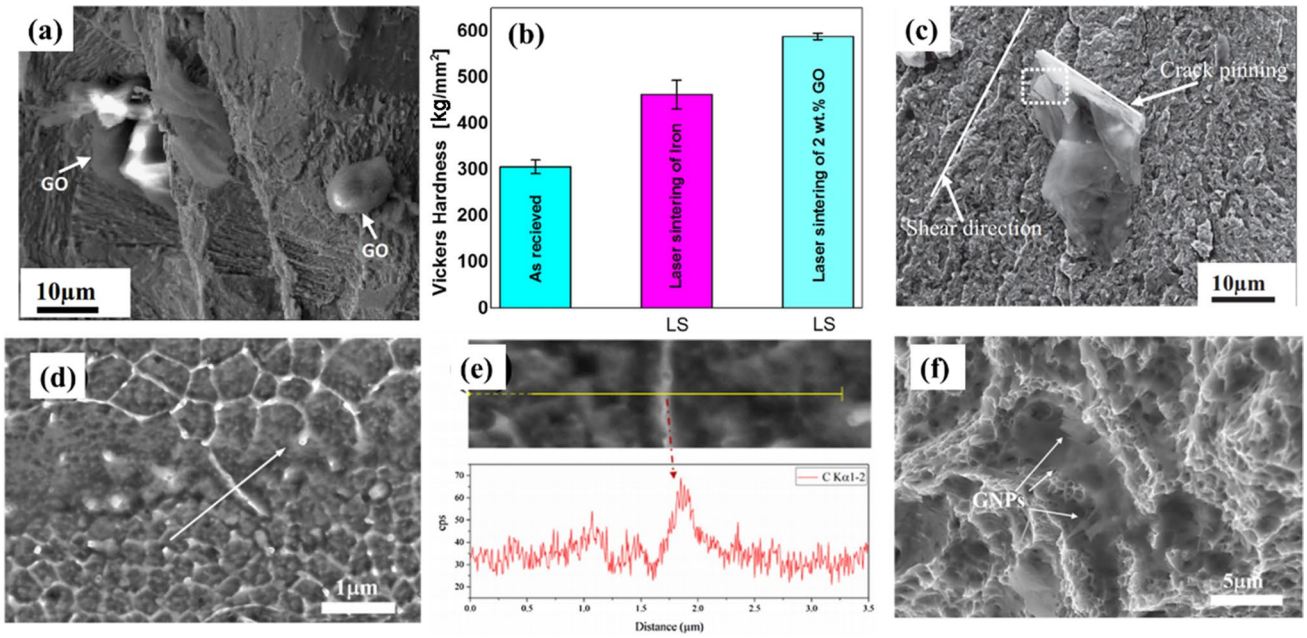

Fig. 4 **a** SEM of the morphologies of GOs in the composites, **b** surface microhardness of the as-received and laser processed samples, **c** crack pinning effect by embedded GO after bending fatigue test [15], **d** SEM images of the GNP at grain boundaries, **e** corresponding EDS analyst results, **f** fractured GNPs in dimples [69]

GO-Fe interface, and GOs were coherently integrated with the matrix. Previous studies by other scholars indicate that in the fabrication of graphene nanoplatelets (GNPs)-reinforced IMMC using SLM method, the incorporated GNPs tend to distribute along the grain boundaries, as depicted in Fig. 4d and e [69]. As the dendrites on both sides gradually develop and grow to form grain boundaries, the GNPs experience the forces exerted by dendrite growth on both sides. Figure 4f shows the fracture surface after tensile test. It was noted that the fracture mode of the IMMC is characterized by ductile failure, with dimples evident at the locations containing (GNPs). The fractured GNPs are pulled out from the matrix, indicating that GNPs serve as a medium for load transfer. This also suggests the formation of a well-bonded interface between GNPs and the matrix. The addition of 2-D materials (especially graphene) significantly makes effects on mechanical strength and fatigue life of composites.

2.2 Matrix Phases

The matrix of the IMMC plays a critical role in its mechanical properties and engineering performance. The solidification process, heat treatment, and other fabrication steps influence the distribution of phases and defects within the composite. For IMMCs, austenite, ferrite, martensite, and their numerous combinations allow the design of matrix in a variety of ways. In this section, the phases of iron matrix are discussed. The austenite phase is commonly thought to provide good plasticity and toughness. Good ductility results from the soft and ductile ferrite [70], while high strength is mainly attributed to martensite [71]. The combination of mechanical properties of multiphase iron matrix demonstrates better than the single-phase matrix of IMMCs. Additionally, the heat treatment and other fabrication steps are often employed to optimize the microstructure of matrix.

The performance of IMMCs (yield strength, hardness, corrosion rate, ductility, and wear resistance properties) are changed considerably when the phases of steel matrix are varied [72]. The mechanical properties of IMMCs composed of various matrix phases vary substantially [73]. Ferrite matrix composites have lower tensile strength than austenite matrix composites. The tensile properties of dual-phase steels are significantly better than single-phase austenitic composites, however, the multiplication of tensile strength and elongation of the latter is significantly higher than the former. IMMCs could have different mechanical properties, depending on different chemical compositions, microstructure, and fabrication routes. This section explains the design strategy by describing the mechanical properties applications that were chosen. Table 4 summarizes the various matrix microstructures of IMMCs.

2.2.1 Austenite Matrix Phase

Austenite phase typically possesses exceptional ductility and has been widely used as the matrix phase of IMMCs to

Table 4 Fabrication processes, microstructure, and mechanical properties of IMMCs with different matrixs

Matrix phases	Fabrication processes	Microstructure	Mechanical properties
Austenite matrix [74]	Conventional melting and casting route	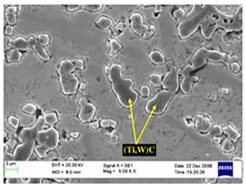	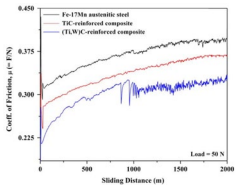
Ferrite matrix [75]	Eutectic solidification	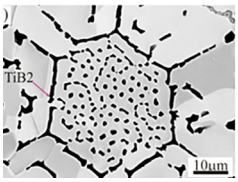	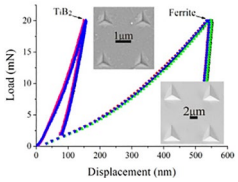
Martensite matrix [76]	Conventional melting and casting	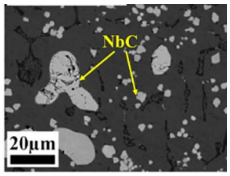	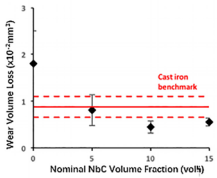
Complex matrix [77]	Electric arc welding	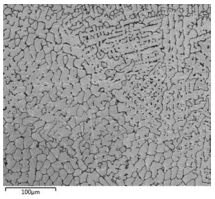	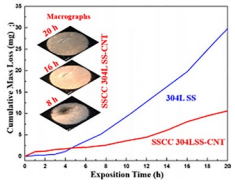

counterbalance the ductility loss due to the introduction of reinforcement phases. IMMCs with austenite matrix have been widely used due to their good ductility and superior stain-hardening capacity [78, 79]. IMMCs with austenite matrix might have high hardness and elastic modulus, which can be fabricated by different processing routes or have multiple chemical compositions and textures [80]. Gowtam et al. [81] effectively prepared in situ TiC reinforced Hadfield austenite matrix steel (Fe, (20, 22, 24%) Mn, (10, 20%) TiC, all in wt%) using conventional melting route, and found advantages in achieving high Mn recovery of the composite. The composite showed two microstructures clearly, ferrite (α) and $(Fe, Mn)_3C$ in the dendritic region, austenite (γ), and TiC particles in the interdendritic regions.

Srivastava et al. [81] effectively prepared in situ TiC reinforced Hadfield austenite matrix steel (Fe, (20%, 22%, 24%) Mn, (10%, 20%) TiC, all in wt%) using conventional melting route, and found advantages in achieving high Mn recovery of the composite. The composite showed two microstructures clearly, ferrite (α) and (Fe, Mn)3C in the dendritic region, austenite (γ), and TiC particles in the inter-dendritic regions. Scrivastava et al. [82] also fabricated the in situ TiC and (Ti, W)C-reinforced manganese austenitic steel matrix composites (0.049% C, 0.43% Mn, 0.028% Si, 0.023% P, 0.013% S, 0.003% Al, 0.035% Cr and balance Fe, all in wt%) using conventional casting route. The composites exhibit a high level of abrasive wear resistance.

Fe–Ni–Cr based austenite phases were widely explored as the matrix phase of IMMCs due to their exceptional ductility [83]. Ni et al. [84] investigated the microstructure and mechanical properties of in situ TiC particulate reinforced austenitic 304 stainless steel (304SS, 18.8% Cr, 8.1% Ni, < 2% Mn, < 1% Si, < 0.045% P, < 0.03% S, 0.05% C, balance Fe, all in wt%) during the conventional melting process. It is clearly seen in Fig. 5a that TiC particles in the matrix exhibit a polygonal morphology with sizes ranging between 2–10 μm. The distribution of these particulates is predominantly uniform, and no noticeable segregation of TiC particulates was observed. Figure 5b shows the creep curves of two steels, the creep tests were carried out at the temperature of 923 K and different stress (100 and 150 MPa). With the addition of TiC, the creep rate of composite decreased, from 6.9×10^{-9} to 1.2×10^{-9} S^{-1}. Figure 5c shows the microstructure of etched TiC-304SS, with finer grains than unreinforced steel, and TiC particles distributed uniformly in the matrix. TEM image of the interface and selected area electron diffraction pattern are shown in Fig. 5d and e, respectively, showing that the interface boundary between TiC

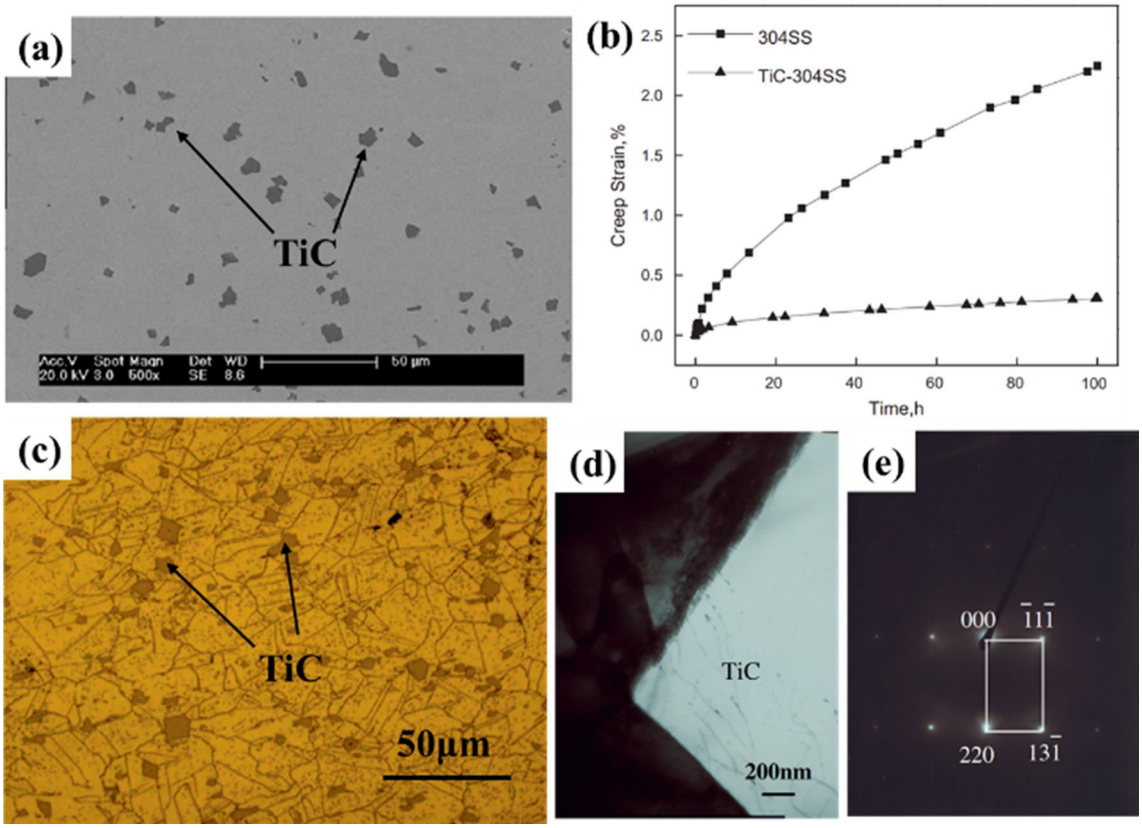

Fig. 5 **a** SEM micrograph showing the morphology and distribution of TiC-304SS, **b** creep curves of two steels, **c** optical micrographs of etched TiC-304SS, **d** TEM image of the interface between TiC and steel matrix, **e** electron diffraction pattern taken from TiC particulate [84]

and steel matrix is clean and no other impurity product has been found. The tensile strength of 304SS was significantly increased by adding TiC. The dislocation density around TiC particles increased with temperature changes during the fabrication process, and the interaction of these dislocation is beneficial for strength. Furthermore, the introduction of TiC is considered to contribute to grain refinement [85], which affects alloy strength according to the Hall–Petch equation, as shown in Eq. (1).

$$\sigma_y = \sigma_0 + kd^{-1/2}. \tag{1}$$

where σ_y is the yield strength of the material, σ_0 is a constant representing the friction stress or the strength when the grain size is infinitely large, k is the Hall–Petch slope or the strengthening coefficient, which depends on the material, d is the average grain size. However, this equation does not hold at very small grain size, especially in the nanometer scale.

2.2.2 Ferrite Matrix Phases

Ferritic steel is defined primarily by its microstructure and the dominance of ferrite in its composition. These steels typically have a lower carbon content, usually less than 0.10%. Wang et al. [86] studied TiB_2 reinforced steel matrix composite (6% Ti, 2.5% B, 0.2% Nb, balance Fe, all in wt%) fabricated using conventional casting process. The addition of TiB_2 promoted dynamic recrystallization, which increased the grain size and hot-formability of the composite. Huang et al. [75] fabricated the TiB_2 reinforced steel composite (6% Ti, 2.2% B, 0.2% Nb, balance Fe, all in wt%) by eutectic solidification, a conventional continuous casting method suitable for industrial production, and investigated the interfacial plasticity between TiB_2 reinforcement particles and the ferrite matrix in the composite fabricated through nanoindentation. Figure 6a shows the SEM image of the distribution of TiB_2 particles in the ferrite matrix. Figure 6b and c depict the EDX maps for Ti and Fe, respectively. In Fig. 6d, the EBSD phase map illustrates that the particles possess a hcp structure. A notably high index rate in EBSD measurement, utilizing the lattice constant of TiB_2, affirms that the particles are indeed TiB_2. Figure 6e represents the EBSD orientation map of TiB_2 particles, while Fig. 6f displays the orientation map of ferrite. The size of the TiB_2 particles depicted in Fig. 6a is approximately 1–2 μm. It can be seen in Fig. 6g that the typical nanoindentation load–displacement (P–h)

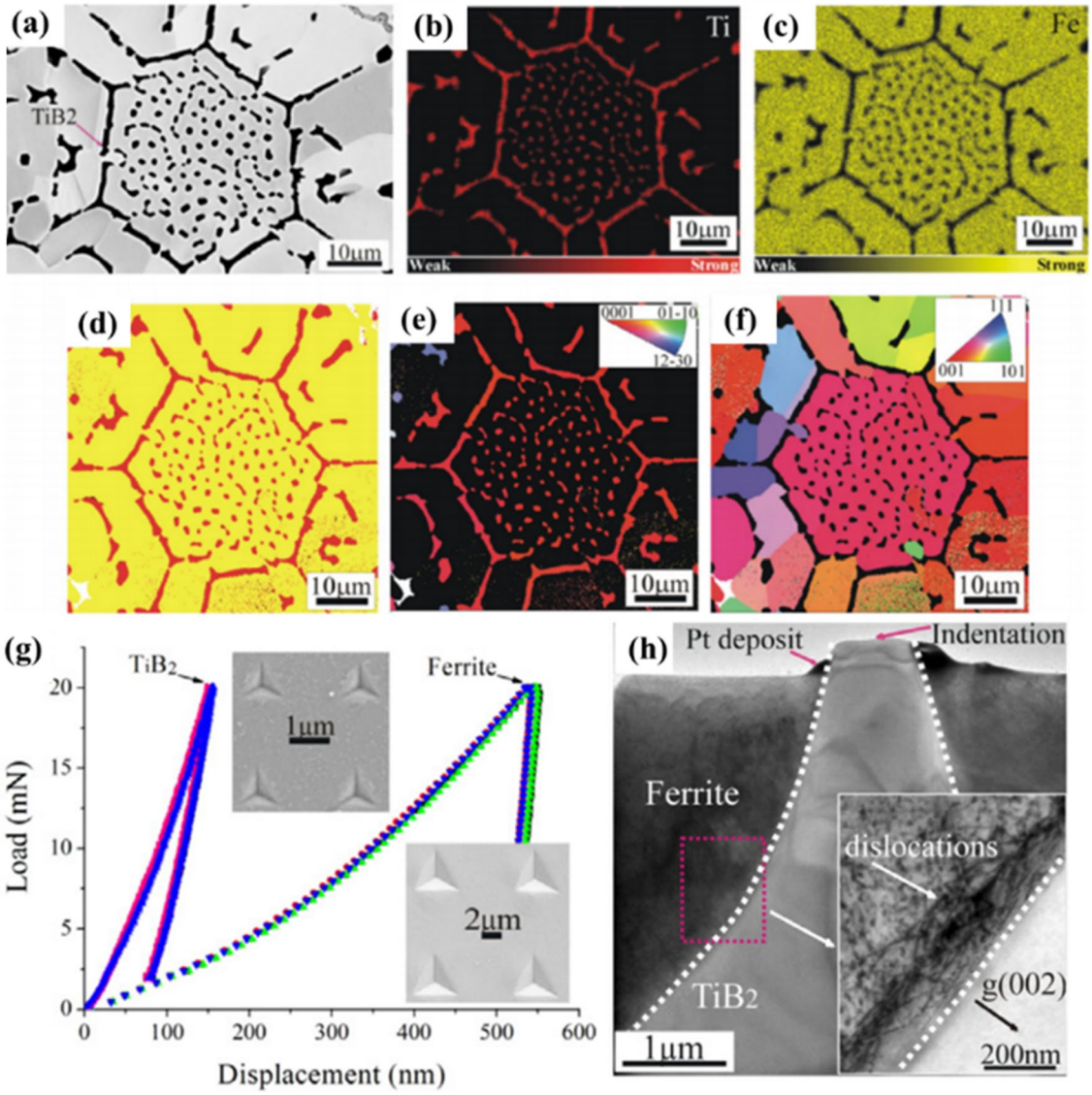

Fig. 6 **a** SEM image of the IMMC reinforced by TiB_2 particles, **b**, **c** EDX map of Ti and Fe atoms, **d** EBSD phase map (red: hcp, yellow: bcc); **e**, **f** EBSD orientation map of TiB_2 particles and ferrite, **g** load–displacement curves measured by nano-indentation tests for the TiB_2 particles and ferrite, **h** TEM image showing the interface between the matrix and reinforcement phases, the white dash lines indicate interfaces and the inserted image shows dislocation aggregates at the interface [75]

curves for the large TiB_2 particles and ferrite. Furthermore, a mixed law (Eq. (2)), which has been successfully utilized to predict the overall Young's modulus of IMMCs, is applied to estimate the Young's modulus of the current IMMC:

$$E_c = \frac{V_m E_m E_p^{1/2} + V_p E_p E_m^{1/2}}{V_m E_p^{1/2} + V_p E_m^{1/2}}. \quad (2)$$

where E represents the Young's modulus, V represents the volume fraction, and the subscripts c, m and p are the composite, ferrite matrix and TiB_2 particles, respectively. The Young's modulus of TiB_2 particles and ferrite are 565 ± 26 GPa and 221 ± 18 GPa, respectively. The bright-field TEM image is shown in Fig. 6h and the dashed white lines are the interfaces, in the magnified image, the high dislocation density was generated and stored at the TiB_2/ferrite interface. The interface of the investigated composites can be subjected to plastic deformation by introducing a high dislocation density. The eutectic solidification products are suitable for conventional continuous casting in industry.

2.2.3 Martensite Matrix Phase

Martensite matrix steel is widely utilized as a wear-resistant material due to their exceptional hardness [87]. The addition of reinforcement particles into the martensite matrix can result in remarkable improvement in wear resistance [83]. The micro-hardness of the martensite matrix shows minor changes when the heat treatment methods are different. Wen et al. [76] explored the mechanical properties of AISI 440B martensite stainless steels (17% Cr, 1.1% C, 0.6% Mn, 0.5% Si, balance Fe, all in wt%) reinforced with 15% NbC particles using a conventional melting process. The martensite was identifiable by grain morphology with primary austenite dendrites transforming into martensite post-heat treatment. The presence of NbC notably enhanced the sliding wear performance.

Chen et al. [88] showed that adding 2 wt% WC to IMMCs via laser additive manufacturing leads to grain refinement through a (Fe, W)6C carbide network and influences phase transformation between austenite and martensite, increasing retained austenite. This resulted in a UTS of ~ 1677 MPa and elongation of ~ 8.5%, improving over the unreinforced steel (~ 1548 MPa and ~ 6.2% elongation). Figure 7a displays a representation SEM microstructure image of LPBF-fabricated 2WC-composite. With the addition of 2 wt% WC, the microstructure changes to a cellular structure, with secondary phases precipitating along cell boundaries. The grains are more refined with the addition of WC compared with the unreinforced samples, as illustrated in Fig. 7b. The strain–stress curves are shown in Fig. 7c, the tensile strength of the 2WC-composite improves to 1677 ± 125 MPa. It can be seen in Fig. 7d that the refined dimples arising from the obtained ultra-fine grains are visible.

2.2.4 Complex Matrix Phase

To fabricate IMMCs with good comprehensive performances, the complex matrix phase of IMMCs was investigated. The duplex steel or multiphase steel shows higher yield strength than single-phase steel when the tensile

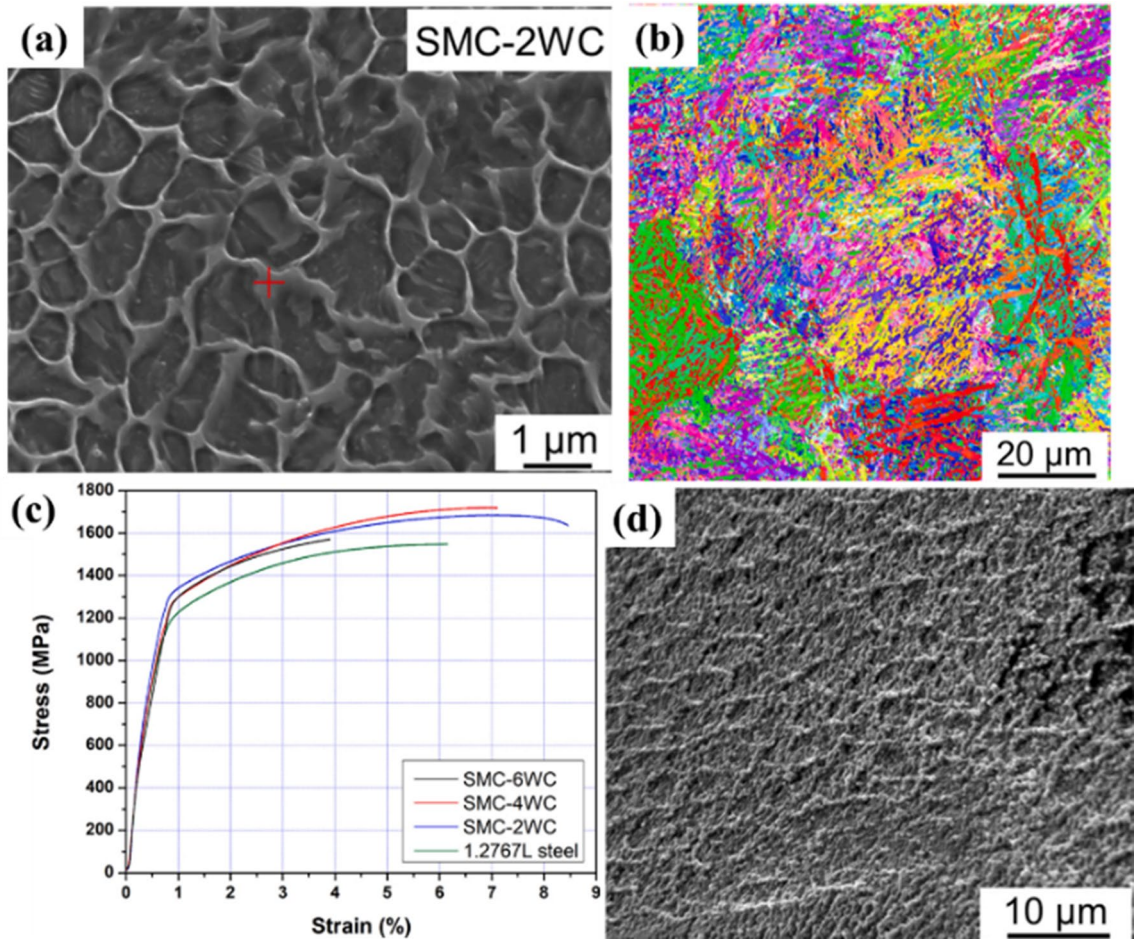

Fig. 7 **a** SEM image of the composite microstructure, **b** IPF map of composite, **c** engineering tensile stress–strain curves of samples with different content of WC, **d** SEM image of the fracture morphology of specimen reinforced with 2 wt% WC [88]

strength value is constant [89, 90]. The proportion of the constitutive phases can modify the properties of composites [91]. The typical characteristics of multiphase steel are high formability, high energy absorption, and high residual deformability [92, 93]. Nascimento et al. [94] have prepared 10 vol% WC/duplex stainless steel (0.04% C, 25.01% Cr, 5.53% Ni, 0.99% Si, 2.11% Mo, 0.006% S, 0.026% P, 3.10% Cu, balance Fe, all in wt%) through laser melt injection technique and studied the dry sliding wear behavior of composites. As a result, the microstructure is characterized by WC particles distributed in a duplex steel matrix which is bonded to the matrix strongly. In addition, this study demonstrates that the wear resistance of duplex steel can be improved by adding WC particles during laser surface remelting. Srivastava et al. [73] have fabricated 10 vol% TiC-reinforced manganese austenitic steel composite (0.049% C, 0.43% Mn, 0.028% Si, 0.023% P, 0.013% S, 0.003% Al, 0.035% Cr and balance Fe, all in wt%) through conventional casting process and found the wear rate of the reinforced composite (~0.12×10^{-4} (mm^3/m)) is higher than the unreinforced composite (~0.5×10^{-4} (mm^3/m)), at the load of 24.5 N. The corrosion rate of the composite is higher than unreinforced steel with an increasing percentage of TiC because of the galvanic effects between the matrix and reinforcement particles [95].

Oke et al. [72] have evaluated the addition of TiN nanoparticles on the densification and shrinkage of duplex stainless steel composite by spark plasma sintering method. The composite displayed low density with increasing TiN content. The microstructure of the duplex steel with 6% TiN contents containing α, γ, and nitride phases at grain boundaries. Moreover, the shrinkage rate increases with adding TiN nanoparticles. In addition, it is observed that the density of composites decreases with increasing TiN content.

Tan et al. [96] investigated SiC-reinforced precipitation hardening steel using additive manufacturing to induce in situ precipitation and duplex strengthening. The sample with 3 vol% SiC exhibited minor gas pores from high laser energy, and its SEM microstructure showed cellular structures with numerous nanosized particles. EDS analysis indicated higher Al, Ti, and Si levels in particles than in the matrix, suggesting SiC facilitated particle precipitation during manufacturing. EBSD results revealed no preferred orientation but a high presence of high-angle grain boundaries (88%), possibly due to SiC addition, influencing the austenite and martensite phase distribution. The inverse pole figure (IPF) of the martensite phase in Fig. 8f shows a typical lath morphology, which indicates a preferred orientation close to < 111 > direction. The engineering stress–strain curve

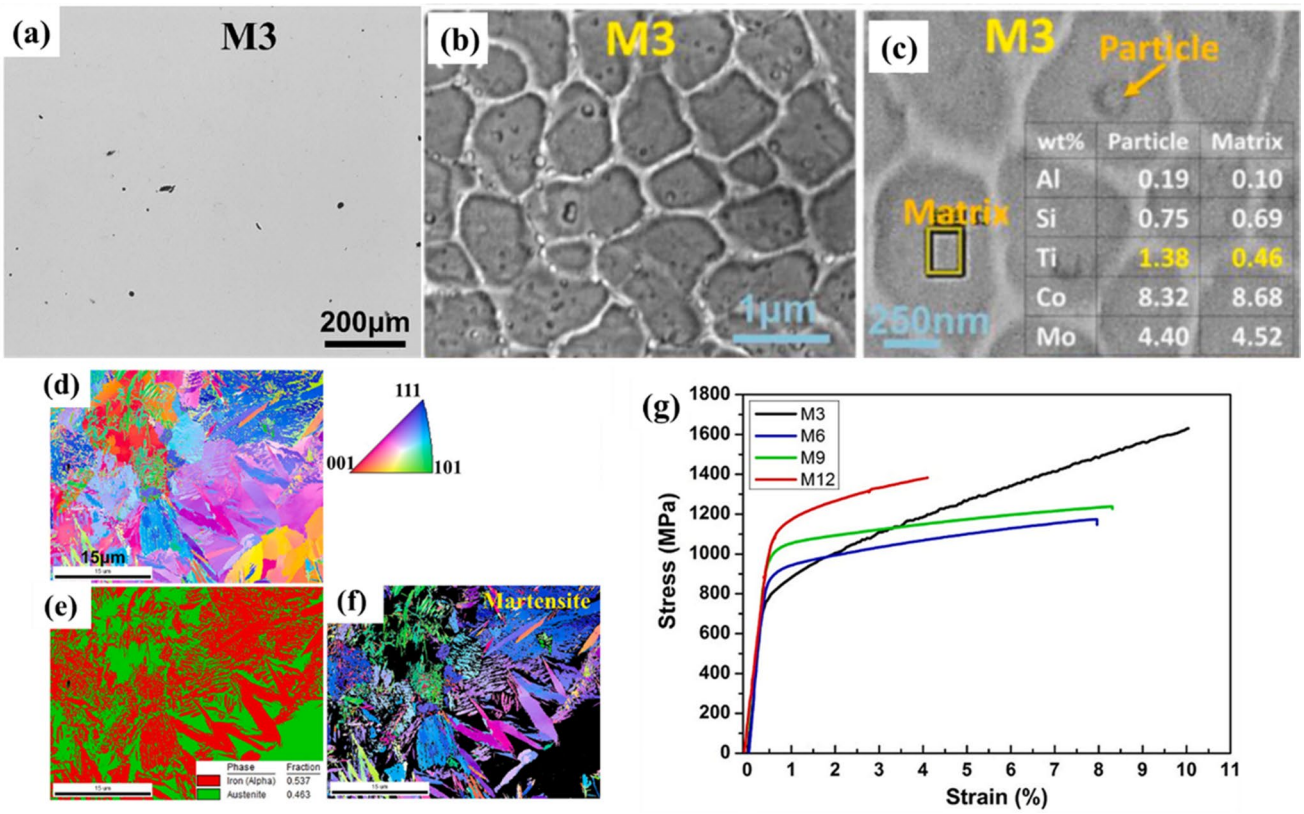

Fig. 8 **a** OM, **b** SEM, and **c** EDS analysis of M3 sample. EBSD analysis of M3 sample: **d** IPF, **e** phase distribution map, **f** IPF of martensite phase; **g** tensile engineering stress–strain curves of IMMCs [96]

of MMCs samples is shown in Fig. 8g, M3–12 represent different SiC contents (3–12 vol%) where the results show that the YS of MMCs gradually increased with the increase of SiC. Compared with unreinforced steel, the M3 sample has a lower YS but reached a much higher ultimate tensile strength (UTS) of 1611 MPa and elongation of 10.1%. Overall, the addition of SiC in the precipitation hardening steel matrix via additive manufacturing process promotes duplex strengthening and improves the mechanical properties of the material. Multiphase IMMCs contain several alloying elements like Mn, Al, and others, for this reason, the production costs will be higher.

2.3 Interface

The interface can be described as a micro-area that shows a significant change in chemical composition compared with the reinforcements and iron matrix. The properties of IMMCs are significantly influenced by the bonding of reinforcement/matrix interface. Due to the distinct physical and mechanical properties between reinforcement phases and iron matrix, interface has always been research focus for the development of IMMCs. The ability of the interface to transfer loads effectively depends on the bonding strength between the reinforcement and the matrix, with strong bonding facilitating the effective transfer of stress [97]. The superior interfacial strength of the reinforcement and the matrix avoids the micro-cracks forming at the interfaces [98]. As shown in Fig. 9a, the interface includes the original contact surface between the matrix and the reinforcement part, the elements of the matrix, the reinforcement, and impurity elements [99, 100]. The phase structure and chemical composition of interface are more complex than the matrix and the reinforcement. Notably, the bonding strength is greatly dependent on the wettability between the iron matrix and reinforcements, as shown in Fig. 9b and c. The interface acts an essential role in the stress, strain distribution, load transfer, fracture process, and thermal expansion in IMMCs. Therefore, the microstructure, reaction, and properties of the interface are a central topic for all kinds of IMMCs. Korinek et al. [101] studied the steel-based composites reinforced with TiB_2. Figure 9d shows the TEM images of TiB_2 and Fe matrix. The interface in Fig. 9e exhibits two kinds of facets parallel to prismatic $\left(10\bar{1}0\right)$ plane and a pyramidal $(10\bar{1}0)$, the third-densest plane of TiB_2. Additionally, the interface between Fe and TiB_2 is mainly parallel to the diboride, with prismatic planes $\left\{10\bar{1}0\right\}$ growing preferentially. At interfaces parallel to the prismatic planes, interfacial misfit dislocations develop. Figure 9f depicts the edge-on view of an interface parallel to the TiB_2 prismatic plane. Interface planes are $(10\bar{1}0)_{TiB_2}//(44\bar{5})_{Fe}$. The Fe and TiB_2 phases exhibit high coherency, according to atomic-scale studies of surfaces. The primary aspect in IMMCs fabrication lies in making interfaces with good bonding, without deterioration due to reaction. Typically, the formation of the interface is formed through the conversion of mechanical energy into interface energy. These important points, such as geometry, reaction and the role of the interface in governing overall performance, are discussed in more detail in this chapter.

2.3.1 Interface Geometry

The reinforcing effect is mainly related to the reinforcement-matrix interface quality, which is mainly controlled by its geometry, such as the morphology and thickness of the interface. A strong interfacial bond is desirable to transfer loads efficiently between the matrix and the reinforcement. The interfacial voids between reinforcements and matrix may cause the geometry issues [102]. In addition, the microcrack development and coalescence might be accelerated by interfacial voids, resulting in a decrease

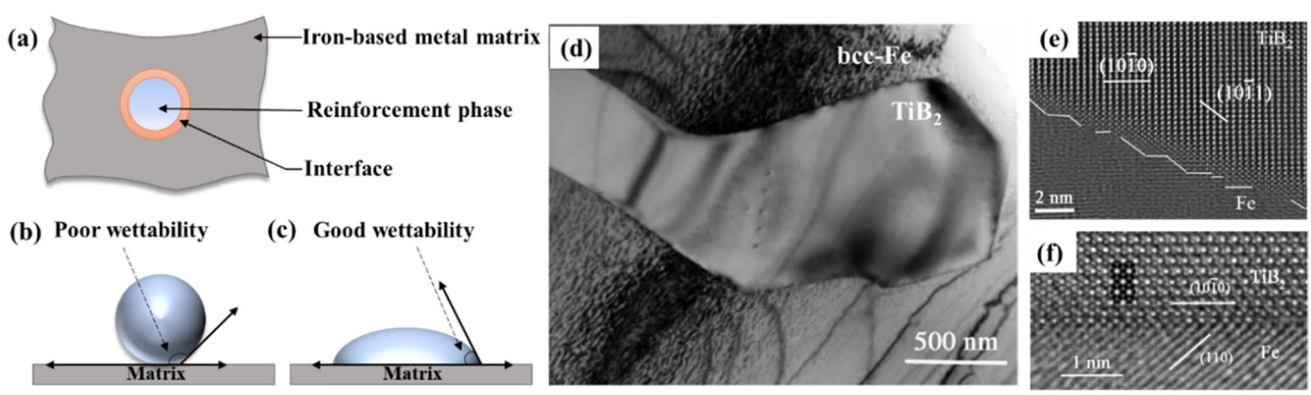

Fig. 9 **a** Schematic illustration of the structure of the interface in IMMC. Contact condition of **b** poor wettability and **c** good wettability between reinforcements and matrix, **d** TEM images of TiB_2 and Fe matrix, HR-TEM image of **e** a rounded interface and **f** an interface of Fe–TiB_2 parallel to the TiB_2 prismatic plane $\{10\bar{1}0\}$ [101]

in tensile strength. Cen et al. [103] produced TiC–Fe composites using the combined method of casting penetration technology and in *situ* synthesis. The whole in situ reaction of TiC formation is mainly controlled by diffusion. The results showed that the mutual penetration of Ti and Fe occurs at the interface between reaction zone and matrix. Besides, the TiC particles with average size of 2–5 μm uniformly distributed in the reaction zone, which may cause a good quality of interface between TiC particles and matrix. It was also found that there are no defects are observed in the interface. Joshua [104] analyzed the interface of Fe-SiC composites made by hot isostatic pressing (HIPing), finding the interface thickness between 0.5 and 1 mm, with its properties linked to matrix component dissolution. Li et al. [105] explored the interface between WC and IMMCs using spark plasma sintering (SPS). They observed that interface width increases with remelting temperature due to reinforcement growth driven by mutual diffusion at the interface, requiring an activation energy of 205.4 kJ/mol.

Chen et al. [34] overcome the predicament of strength-ductility trade-off which is the main challenge of fabricating IMMCs, combining high strength of about 2833 MPa and large ductility of about 32% utilizing the laser powder bed fusion (LPBF) method. It can be seen in Fig. 10a that WC particles are well bonded to the matrix. Figure 10b depicts the different angle grain boundaries respectively. A high-resolution TEM image of the interface between the particle and the surrounding matrix is shown in Fig. 10c. Figure 10d and e display the fast Fourier transformation (FFT) patterns from two regions, the red (nanoprecipitate) and blue (matrix) rectangle, respectively. The FFT spots confirm that the nanoparticle and steel matrix is indeed of Fe_2W_2C type carbide and austenitic structure. The $\left[1\bar{1}1\right]$

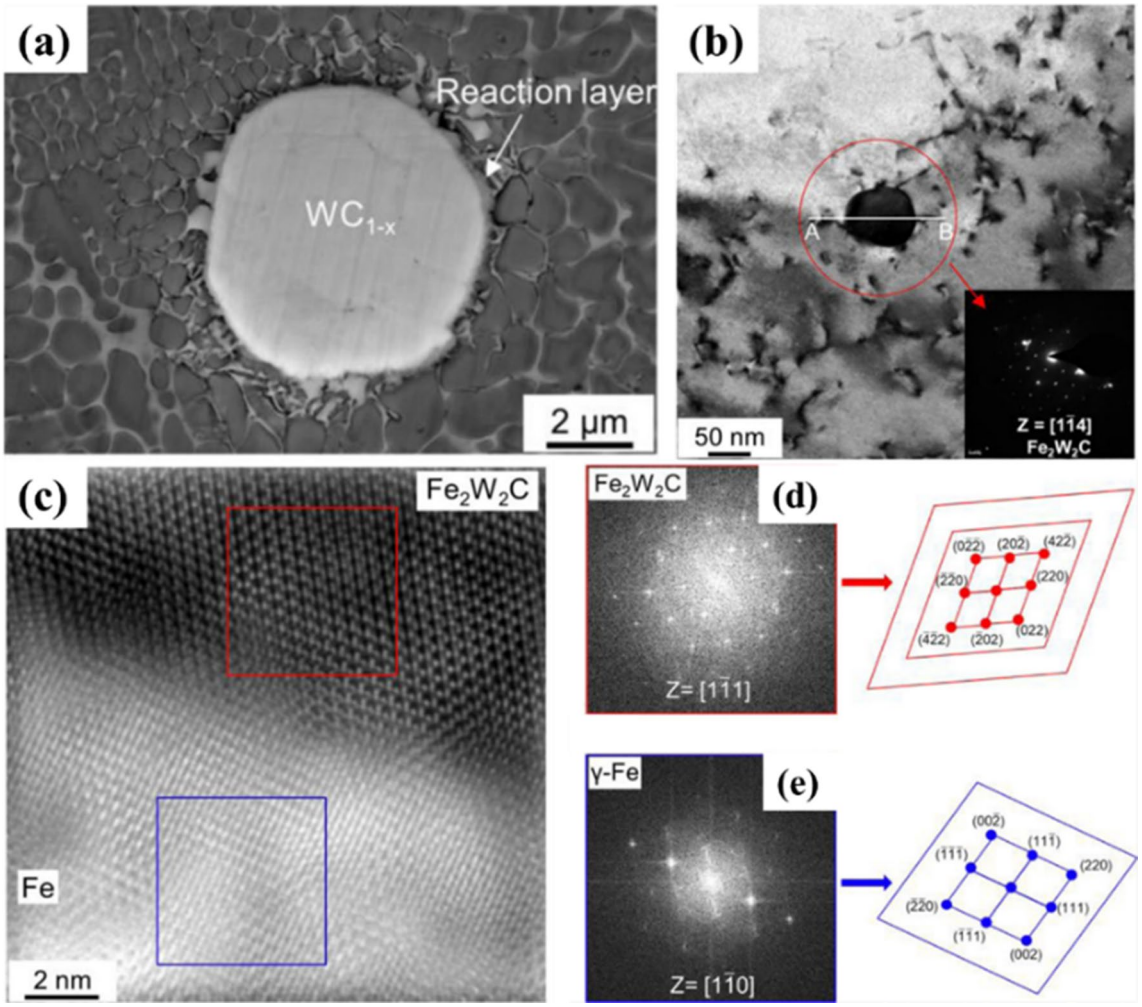

Fig. 10 **a** SEM image of WC particle, matrix, and reaction layer, **b** TEM images showing the magnified microstructure of IMMC and the indicated region shows the nano-sized Fe_2W_2C precipitation, **c** HR-TEM image of the interface between the nanoparticle and matrix, the orientation of **d** Fe_2W_2C nanoparticle, **e** austenite matrix [34]

direction of the Fe_2W_2C is parallel to $\left[1\bar{1}0\right]$ direction of iron matrix. Overall, understanding and optimizing these aspects of interface geometry are critical for tailoring IMMCs for specific applications. Researchers and engineers often utilize various processing techniques and characterization methods to control and analyze the interface in IMMCs.

2.3.2 Interface Reaction

The interface reaction involves the interactions between reinforcements and matrix. Depending on the specific composition, processing conditions, and the type of raw materials used, the reaction will be different. It has a significant influence on the properties of composites [99]. The products and degree of interface reaction are different with various reinforcement phases. Some of the reinforcement phases, such as alumina and ZTA particles, may react with the matrix metals whereas others do not [44]. Some interface reactions may cause deterioration of properties [106], therefore they should be properly controlled. The interface reaction during the preparation process can be divided into three categories: the reaction of reinforcement phase generation [103], and the reinforcement phase reaction with matrix [44]. However, when the molten matrix metal solidifies gradually, interface chemical reactions tend to occur, potentially leading to the degradation of the reinforcement. The studies of interface reactions mainly focus on thermodynamics and kinetics. Li et al. [105] used first-principles calculation to determine that the Fe_3W_3C compound was thermodynamically stable, which was then validated by experiments. Joshua [104] investigated the reaction kinetics of the Fe–SiC system and discovered that its growth is diffusion controlled, and that the reaction interface may act as a diffusion barrier, preventing fiber degradation under appropriate heat conditions.

Guicheteau et al. [97] fabricated iron-ferrite composites by powder metallurgy process. By adding a silica layer between the iron and ferrite layers, the redox interfacial reaction and iron diffusion were prevented at temperatures up to 800 °C, and the consumption of reinforcement was avoided. Figure 11a demonstrates a complex microstructure of the three phases, with pure Fe grains still present. The analyses of oxygen, iron, nickel, and zinc are presented in Fig. 11b. Figure 11c and d clearly shows the chemical reaction in the interface between iron and ferrite. The entire Fe film had diffused inside the ferrite substrate, through the SiO_2 layer, leading to the formation of a thin Fe_2SiO_4 layer, according to

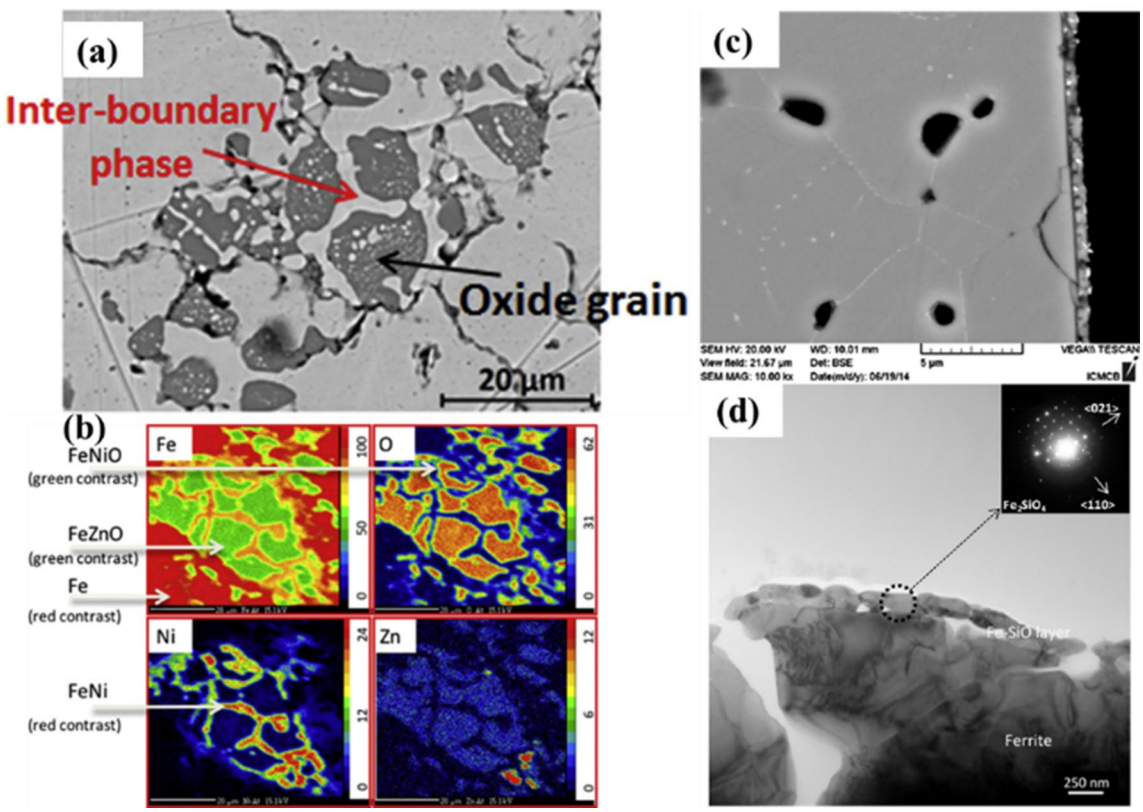

Fig. 11 **a** SEM micrographs of composite heat treated at 900 °C. **b** EPMA element cartography of Fe, Ni, O, Zn on ferrite mixed powders after treatment at 900 °C under N_2. SEM micrograph **c**, and TEM micrograph **d** of Fe-SiO_2-ferrite system heat treated 1 h at 900 °C under N_2 [97]

Table 5 Typical in situ reaction routines and Gibbs free energy of reactions for fabricating IMMC

Reinforcement phase	Chemical composition of the matrix	Reaction equations	Gibbs free energy under 1873 K (kJ/mol)
TiB_2 [107]	Fe-6 Ti-2.2 B-0.2 Nb (in wt pct)	$FeTi + 2FeB + Fe = TiB_2 + 4Fe$	−121.311
TiC [108]	Fe-3.61 C-2.5 Si-0.81 Cu-0.24 Mn-0.03 Ni-0.03 Cr-0.02 Ti-0.02 Mo-0.008 S-0.02 P (in wt pct)	$Ti + C = TiC$	−157.296
NbC [76]	Fe-16.7 Cr-1.1 C-0.6 Mn-0.5 Si (in wt pct)	$Nb + C = NbC$	−127.794
Al_2O_3 [46]	43.14 Fe-15.85 Fe_2O_3-19.52 Cr_2O_3-7.43 NiO-14.06 Al (in wt pct)	$Fe_2O_3 + 2Al = Al_2O_3 + 2Fe$	−727.151

SEM and TEM investigation. There is a heightened propensity for the emergence of intricate interface reactions in the in situ IMMCs. Furthermore, Table 5 depicts some typical in situ reaction routines and Gibbs free energy of reactions for fabricating IMMC. Understanding and controlling interface reactions are vital for tailoring the properties of IMMCs to meet specific application requirements. Some techniques such as microstructural analysis, diffraction methods, and thermodynamic modeling are used to study and optimize the interface reactions.

3 Fabrication Methods of IMMC

In recent years, a range of fabrication methods has been developed [109–111]. These can be categorized into three primary groups of techniques according to the state of the raw materials during the preparation process: 1) liquid-state (including squeeze casting; conventional casting; infiltration; liquid phase sintering; selective laser melting); 2) solid-state (including powder metallurgy; spark plasma metallurgy; self-propagating high temperature synthesis); 3) gas-mixing processing (mainly including vapor liquid synthesis; spray deposition). In addition, IMMCs fabricated by in situ processes have attracted considerable attention recently [5, 108, 112]. The reinforcement is synthesized by the spontaneous reaction between the matrix components. Moreover, the method of generating and growing reinforcements in the matrix during the manufacturing of composites is called in situ process [113]. On the contrary, the key of the ex situ method is that reinforcements are added externally [114]. Under certain conditions, the in situ synthesis methods can produce one or more particles reinforced metal matrix through chemical reactions of different elements. The reinforcement particles grow in the matrix, resulting in good solubility of the matrix and the reinforcement and strong interfacial bonding strength. Some in situ methods, such as self-propagating high temperature synthesis [115], vapor–liquid synthesis [116], and so on, also belong to the three primary categories. Table 6 summarizes the typical fabrication methods of IMMCs. In this section, recent developments in the major processes are presented and their characteristic features are described. Common phenomena associated with these processes are examined on a fundamental level, aiming to acquire a systematic comprehension of fabrication procedures.

3.1 Liquid-State Processing Techniques

This category encompasses procedures where reinforcements are incorporated in to liquid matrix, with ceramic reinforcements are usually used. Notably, these reinforcements exhibit limited wettability by molten iron or steel. When the contact angle between molten matrix and the reinforcement surpasses 90°, the task of mixing and dispersing the reinforcements within the molten metal becomes difficult. Some different types of methods are introduced to meet this challenge. Such as coating to the surface of the reinforcements, adding certain elements, and designing in situ reaction of reinforcements. These methods are implemented within various fabrication techniques which are discussed in detail in this part.

3.1.1 Infiltration Process

Molten metal infiltration in ceramics performs is among the most widely used approaches for fabricating MMCs. The basic idea of this fabrication process involves the infiltration of molten metal through the channels of a porous ceramic preform to fill the pores and generate the composite structure [125]. It stands out due to its capability to produce MMC with complex shapes, low residual porosity, and relatively low cost [126]. Based on the performing environment, infiltration process can be realized by spontaneous infiltration [127], gas pressure infiltration [128], and reactive infiltration [129]. Zhong et al. [130] investigated the microstructure and mechanical properties of in situ vanadium carbide reinforced IMMCs. The microhardness of composites is four times higher than iron matrix due to the formation of V_2C and V_8C_7 as reinforcement. Wang et al. [131] studied the feasibility of utilizing reactive infiltration for fabricating the TiB_2–TiC reinforced steel matrix composite. The process can be described as: a green cylinder preform consisting of a mixture of Ni, Ti, and B_4C powders prepared by powder

Table 6 Summary of the commonly used fabrication methods of IMMCs

Categories	Fabrication methods	Advantages	Disadvantages	References
Liquid state	Squeeze casting	Simple process, suitable for mass production	Inhomogeneous composite structure	[117]
	Conventional casting	Simple process, low manufacturing cost	Suitable for industrial production	[37]
	Liquid phase sintering	Better wettability between the reinforced phase and matrix	Large porosity of products, poor hardness, and wear resistance	[118]
	Infiltration casting	Low equipment requirements, small investment	Poor wettability between the reinforcement phases and matrix in the finished products	[25]
	Selective laser melting	High-quality products	High cost	[28]
Solid-state	Powder metallurgy	A large variety of available reinforcement phases and a large volume fraction of reinforcement phases	Complex production process and high cost	[119]
	Spark plasma metallurgy	Good dispersion and bonding of the reinforcement phases and matrix	Difficult to apply to the preparation of large parts, complex shape parts	[120]
	SHS (self-propagating high temperature synthesis)	The simple production process, rapid reaction, high product purity	Difficult to control the reaction, large porosity and poor denseness of the products	[121]
	Exothermic dispersion	Simple reaction process	Large porosity of the resulting composites	[122]
Gas-mixing processing	Vapor–liquid synthesis	Low cost, simple process	Inhomogeneous microstructure, high energy consumption	[123]
	Spray deposition	Low pollution, high productivity	Large porosity, low material recovery	[124]

metallurgy was first placed at the bottom of the sand mold with a zigzag shape. Subsequently, the steel melts with a temperature of about 1600 °C were poured into the sand mold to ignite the self-propagating high temperature synthesis (SHS) reaction, which can be described as: $x\mathrm{Ti} + \mathrm{Ni} \rightarrow \mathrm{Ti}_x\mathrm{Ni}$ and $2x\mathrm{Ti} + \mathrm{Ti}_x\mathrm{Ni} + x\mathrm{B}_4\mathrm{C} \rightarrow 2x\mathrm{TiB}_2 + x\mathrm{TiC} + \mathrm{Ni}$. As a result, TiB_2 and TiC phases were generated in the sample with an average size of around 5 μm are uniformly distributed in the steel matrix. However, some micro-porosity can be detected in the microstructure of the sample with a Ni content of 20 wt%. As the Ni content increased to 30 wt%, micro-porosity is absent due to the reduction in the gas evaporation generated in the SHS reaction caused by the decreased combustion temperature.

Qiu et al. [132] investigated the microstructure, mechanical properties and wear resistance behavior of ZrO_2–$\mathrm{Al}_2\mathrm{O}_3$ (ZTA)/HCCI (High Cr casting iron) composite prepared by pressure infiltration process. Figure 12a shows the schematic illustration of this process. First, the raw materials, mold, and ZTA particles was heated to 1580 °C, 260 °C, and 1000 °C, respectively. The chamber was filled with liquid iron. Meanwhile, the preheated ZTA particles were introduced. Then, the pressure of 125 MPa (P1) was applied to push the molten steel and particles to fill the channel. Under the effect of high kinetic energy and viscosity of the molten steel, particles acquire uniform dispersion in the channel. A pressure of 130 MPa (P2) was exerted to the metal-particles mixture for achieving solidification and bonding between matrix and ZTA particles. After the solidification of composite, the mold was opened. Finally, composite was ejected under pressure (P3). They found that the ZTA particulates distribute uniform throughout the matrix, and the interface is tight bonding, as shown in Fig. 12b and c. Moreover, Fig. 12d demonstrates the dark and bright regions correspond the reinforcements and matrix, respectively. The matrix displayed a typical dendritic microstructure and composed of α-Fe, γ-Fe, and eutectic carbides $(\mathrm{Fe, Cr})_7\mathrm{C}_3$. The comparation of the cumulative volume loss of different materials, as shown in Fig. 12e, reveals significant differences in their wear resistance. It can be seen that the total volume loss of the pure HCCI was much higher than the other two composites at different impact energies. With an increase in energy to a higher level, the predominant wear mechanism comprised a synergistic combination of reinforced particles breaking and detachment, fragmentation of abrasives embedded in the matrix surface.

3.1.2 Squeeze Casting

Although infiltration is capable to produce a variety of IMMCs with complex shapes, it often suffers from porosity, which compromises the mechanical properties of the final product. Therefore, external high pressure is desirable and beneficial to eliminate the porosity or shrinkage,

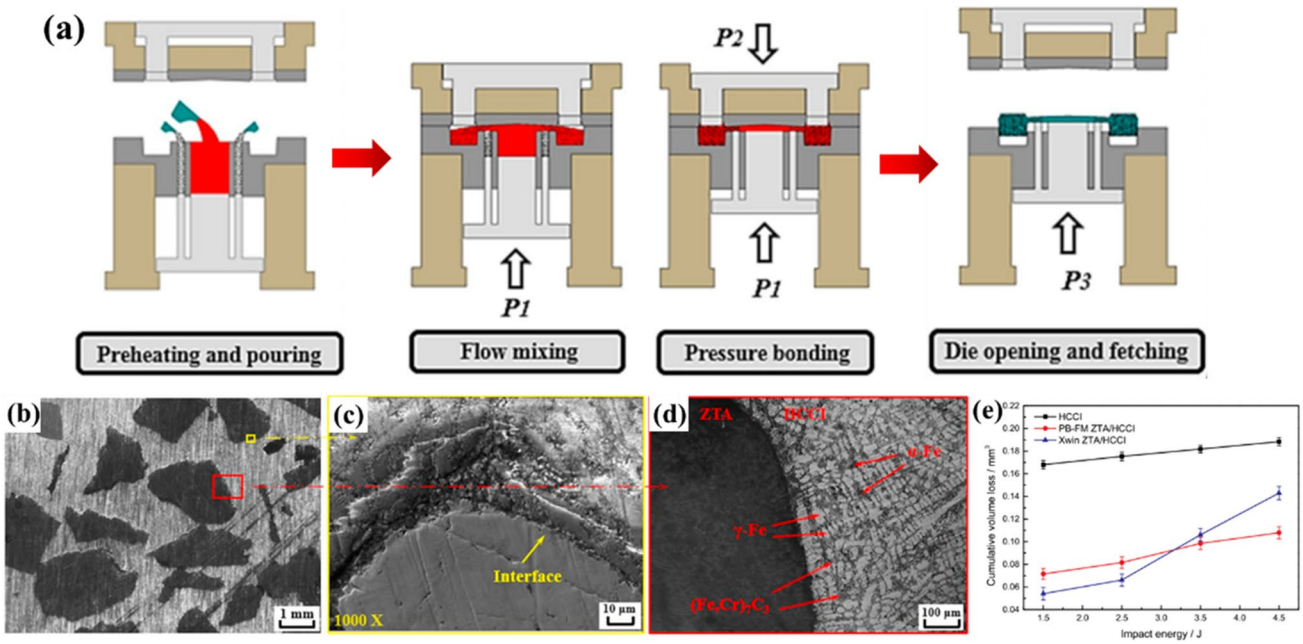

Fig. 12 **a** a schematic illustration of the pressure infiltration process for fabricating IMMCs, **b** distribution of ZTA particles throughout the Fe-matrix, **c** bonding state of ZTA/Fe, **d** Microstructure of the composite, **e** comparation of the cumulative volume loss of different materials [132]

leading to the development of the squeeze casting process. Squeeze casting, which was first used to fabricate copper alloy in 1937 [133], is one of the modern casting techniques. Squeeze casting technology has developed rapidly since the 1970s and is now applied to manufacture steel weapons components [134]. This technique is also called squeeze forming, liquid forging, liquid pressing, extrusion casting, liquid metal stamping, and pressure crystallization [52, 135]. Squeeze casting allows for fabrication of die forging products with fine grain [136], homogenous structure, and superior mechanical properties [137]. The basic idea of squeeze casting is organizing mold casting with die forging into a single procedure in which materials solidify under high pressure within a reusable mold. Squeeze casting is also regarded as a near net-shape route. This procedure shows a simple process and low cost [138]. However, this method has several drawbacks, such as a short mold life and a limited shape complexity.

A number of investigators have studied the effect of using squeeze casting to fabrication iron-based metal matrix composites on the mechanical properties and microstructure of the material. Yao et al. [139] produced steel/ZA8 composite through squeeze casting. The microstructural characteristics and wear resistance properties were investigated. The study found that the composites exhibit lower friction coefficients and significantly lower at 120 °C compared with the unreinforced alloy. Lu et al. [140] have added Ti into Al_2O_3 reinforced 5140 steel matrix composites. The microstructure, hardness, and strength of the composites have also been examined. The wetting angle between steel matrix and Ti–Al_2O_3 powders is clearly smaller than the wetting angle of 150° between steel and pure Al_2O_3 particle. The microstructure of composite is combined with black Al_2O_3 region and matrix. Due to the good wettability and interfacial bonding, the interface between reinforcement and matrix is intact, and there are few cracks.

Khodaverdizadeh et al. [141] investigated the effects of different applied pressure (25, 50, and 75 MPa) during squeeze casting process on the microstructure and mechanical properties of graphite nodules reinforced ductile iron. Figure 13a shows the schematic diagram of the squeeze casting process. Three processes are involved in this technique [142, 143]: placing a reheated Ti–Al_2O_3 preform in a mold, pouring molten steel into it, and infiltrating the molten steel into the preform to produce composites. Furthermore, in Fig. 13b, micrographs of non-etched surfaces of the ductile iron composite under 75 MPa are presented, along with size distributions of graphite nodules at these locations. It can be observed that the graphite particles in the castings are almost all spherical in shape, and the average size of graphite nodules decreases in comparison to the specimens under 0 to 50 MPa. In Fig. 13c, the etched microstructure of the specimen is depicted, featuring ferrite (light area), pearlite (dark area) and cementite (brown area), respectively. The percentage of ferrite phase decreases for the sample cast under 75 MPa applied pressure, while the pearlite and cementite content of the microstructures increase. These changes in the microstructures are attributed to the higher cooling rate and

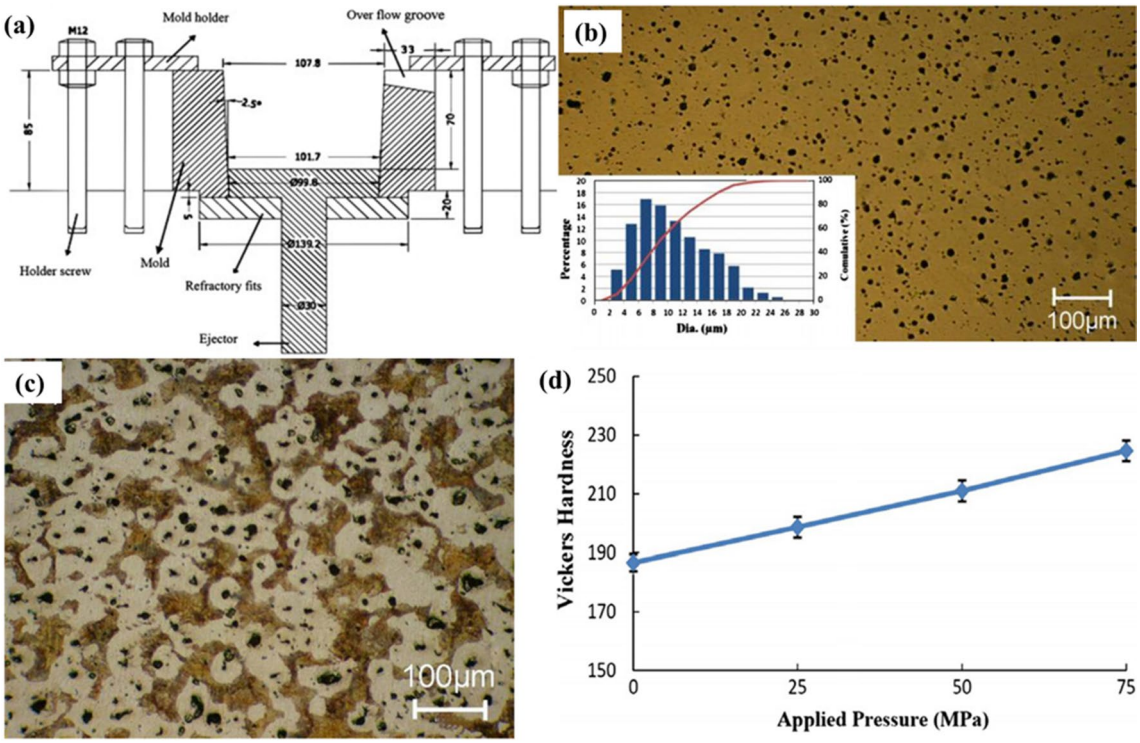

Fig. 13 **a** schematic diagram of a metallic die designed for the squeeze casting process. Micrographs of **b** etched surfaces and **c** etched surfaces of the castings solidified under different applied pressures of 75 MPa, **d** effects of applied pressure on hardness values of the specimens [141]

the facilitation of non-equilibrium eutectic transformation due to the decrease in the temperature interval between the equilibrium and non-equilibrium eutectic transformations when the applied pressure is increased. Finally, Fig. 13d presents the Vickers hardness values of the specimens, which indicate that the decreased ferrite content and increased pearlite and eutectic cementite contents of the matrices, at higher applied pressures, result in higher hardness of the castings. In summary, squeeze casting, provide excellent bonding characteristics between the matrix and reinforcements and allow for the production of high-performance composites. Nevertheless, they require complex setups and precise control of parameters to avoid defects.

3.1.3 Liquid Phase Sintering (LPS)

LPS is a sintering process that involves solid powders coexisting with liquid. It contributes to the formation of high-performance and multiple-phase composites [144]. The basic features of this method involve sintering under conditions where solid grains coexist with a wetting liquid [145]. This process is applied to a wide range of engineering materials. The high melting point reinforcement particles arrange around the metal matrix during LPS procedure, resulting in less porous and more homogeneous products [146]. LPS was found to be used frequently in manufacturing IMMCs due to its easier process, and the final composites fabricated by this method have customized properties [147, 148]. Liquid spreading, solution re-precipitation, and solid phase bonding have been identified as the three steps of liquid phase sintering. Low sintering temperatures, rapid densification, and great mechanical and physical material properties of composites are some of the benefits of this process. The main disadvantages of LPS include high distortion, deterioration of mechanical properties due to the brittle solidification, and grain growth during sintering. The disadvantages lead to the limitation of the final part in high-temperature applications.

The schematic illustration of the equipment and microstructure changes of LPS is shown in Fig. 14a [149]. In case of the liquid wet the solid, the solid-state sintering occurs and liquid penetrates between the solid during heating, which induces grain rearrangement. The target composites are created during solidification. Ninpetch et al. [150] investigated the BN reinforced Fe–Cr-Mo-BN-C steel composites through LPS. Several sets of experiments were carried out with different parameters (the cooling rates of 0.1, 4.0 and 5.4 °C/s). Figure 14b shows the typical micrograph of specimen with BN and 0.2–graphene, in which the obvious spherical pores and ferrite-bainite microstructure can be seen. The SEM micrograph of composite at cooling rate of 5.4 °C/s is shown in Fig. 14c. The thinner layer of liquid phase remained at grain boundary due to some boron atom

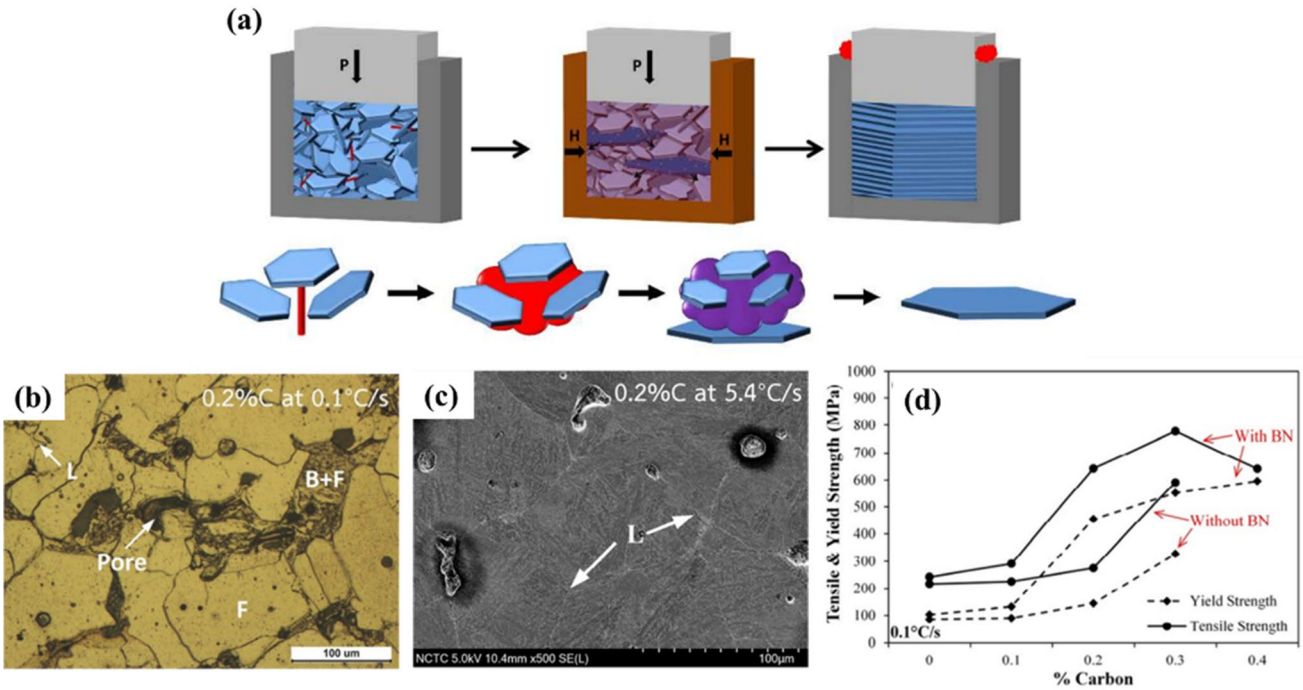

Fig. 14 **a** schematic of LPS equipment and microstructure changes during the process [149], **b** microstructure of the typical micrograph of specimen with BN and 0.2%-graphene, **c** SEM image of sintered samples at a cooling rate of 5.4 °C /s, **d** tensile and yield strength of sintered steels in 0.1 °C /s cooling rates [150]

dissolved in the steel matrix. Accordingly, the diffusion of boron resulted in improvement of hardness of composites. The addition of BN was found to improve the transformation of bainite due to some boron atoms dissolved in the composite at the high cooling rate, which resulted in bainite transformation. The tensile strength and hardness of sintered steel composites were improved because of the diffusion of boron nitride into the matrix, as shown in Fig. 14d. In addition, IMMCs built by LPS has more homogeneous microstructure compared with solid state sintering due to the high solubility between reactants during LPS process [148].

3.1.4 Selective Laser Melting (SLM)

SLM is a liquid state process of MMCs that is based on the local melting of a metal powder bed by a high-power laser beam [151, 152]. This method was first applied in the fabrication of 3D parts in 1995 at the Fraunhofer Institute ILT in Aachen [153] and has found a wide application in the fabrication of IMMCs nowadays. The procedure of SLM is generally described as follows: fine metal powders are spread over a substrate plate, followed by the layer-by-layer remelting of the powders using a high energy laser beam [154]. In comparison to other methods, SLM has a faster processing cycle and a higher flexibility in terms of fabrication IMMC parts with a complex geometry [155]. Moreover, the rapid solidification rate during SLM can effectively avoid the agglomeration of fine reinforcement particles [156].

Some scholars have successfully fabricated particle reinforced IMMCs through SLM [157]. Kang et al. [158] have manufactured in situ tungsten carbide (WC)-reinforced IMMC using SLM. The composites have high relative density and the WC particles are distributed homogeneously in the substrate. Regarding IMMCs, Mandal et al. [67] have fabricated graphene-reinforced 316 L stainless steel through SLM technique. Figure 15a and b illustrates a schematic representation of the SLM system and process. In this system, the mixed powders are melted layer by layer using high power laser in an argon atmosphere. Graphene and steel were first broken and mixed in a ball mill, after which the mixed powder was delivered to SLM system and formed. Figure 15c shows the optical images of etched 0.2%Gr/316 L steel, indicating a strong bonding between the layers. There is no trace of pores are found in the composites even at high magnification. This phenomenon reveals that powder particles fused successfully during melting. Moreover, the SEM image of the microstructure is shown in Fig. 15d, where very fine sub-grains show the cellular morphologies and random orientation. The true stress–strain curves of samples with different Gr contents are illustrated in Fig. 15e. The obtained YS of the composite with 0.2 wt% Gr was 850 ± 40 MPa, representing an approximate 70% increase compared to the bare SS 316 L sample (502 ± 25 MPa). The significant

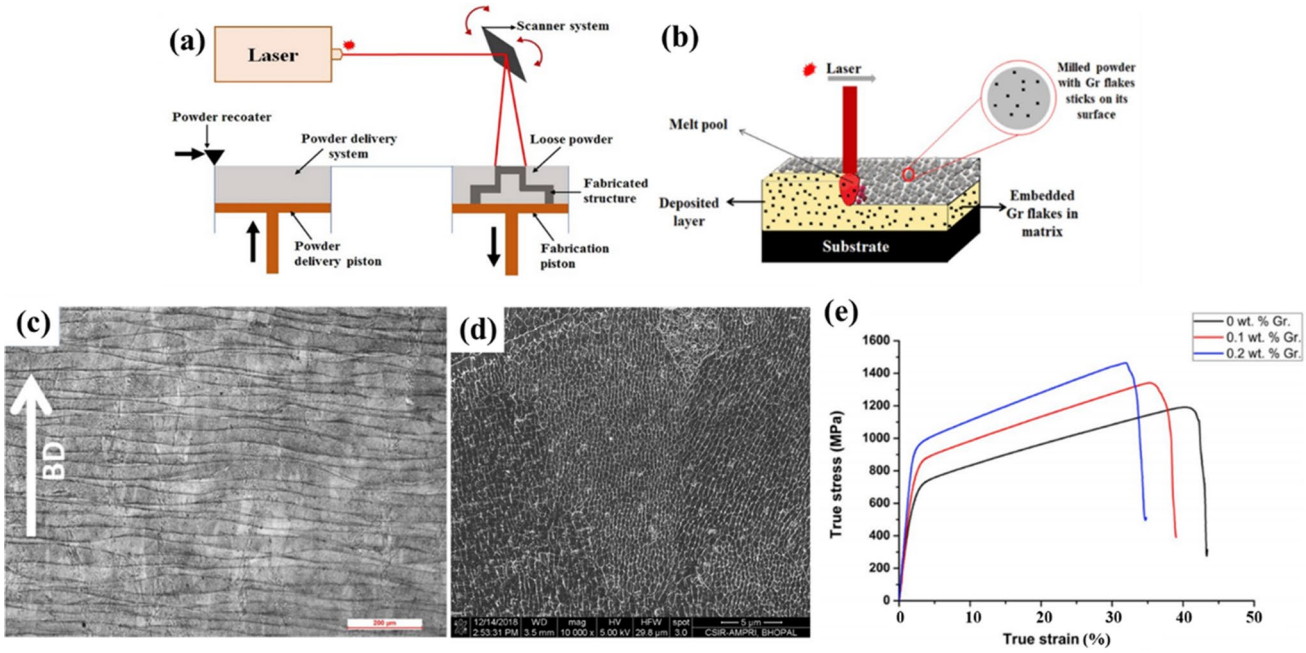

Fig. 15 Schematics of **a** SLM system and **b** SLM process. Microstructure of Gr/316L steel: **c** optical image and **d** FE-SEM image. **e** True stress–strain curve of samples with different Gr contents. [67]

enhancement in strength can be ascribed to the synergistic impact of Gr presence, increased dislocation density, grain refinement, and efficient load transfer from the matrix to the reinforcement.

3.1.5 Conventional Casting

Conventional casting is a method of pouring liquid metal into a mold, followed by cooling and solidifying to obtain an ingot or blank [159, 160]. Conventional casting is a metal hot working technology that human-beings have employed for almost 6,000 years [161]. The most significant advantage of conventional casting is economic benefits and the ability to fabricate large-scale. However, this process faces some problems, such as density-induced-floatation of reinforcements caused by the density differential between reinforcements and iron matrix.

Niu et al. [162] presented an in situ TiC reinforced gray cast iron-based composite by the conventional casting process. The results illustrated that the primary and secondary TiC particles, as well as pearlite, develop during rapid cooling. In comparison to unreinforced gray cast iron (19.35 mg/cm^2), the composite presents a promising wear rate of 5.34 mg/cm^2. Mei et al. [163] used the conventional casting method in a medium frequency induction furnace to fabricate iron composites reinforced by TiC particles. During an in situ synthesis reaction between liquid Fe–Ti and Fe–C, the reinforcements were produced. The microstructure of matrix was identified as pearlite, and the TiC particles dispersed in matrix uniformly due to electromagnetic force. Wang et al. [164] fabricated TiN-reinforced iron composite through conventional casting process. Due to the slow cooling rate, the precipitation of reinforcements in the matrix is fully developed. In addition, the shape of the precipitate is irregular and with sharp corners. Figure 16a and b presents the schematic illustration of the apparatus with stirring function and vacuum die casting [165]. The conventional casting processes involve pouring the molten steel into a mold cavity that takes the shape of the final part, cooling of molten steel with heat generally being transferred from the mold, and solidifying it into the desired shape finally.

Kan et al. [76] fabricated martensitic steel composites reinforced with in situ NbC particles by conventional casting process. The AISI 440C, graphite, and ferro-Nb powder, as the main raw material, were melted and poured into a graphite crucible using a vacuum induction casting furnace. The EBSD phase map of the composite with 10 vol% NbC is shown in Fig. 16c. The image shows the morphology of the martensitic structure, and the carbides in the composite form an interconnected eutectic network. A certain number of NbC particles (15–20 μm in diameter) were distributed in matrix uniformly. Figure 16d presents the continuous grooves along wear tracks, reveals that micro-cutting played the major role, as far as dominant wear mechanism is concerned. Figure 16e illustrates the results of Coriolis erosion wear test (Squares represent against medium sand, triangles represent against garnet). The wear resistance of each sample is dependent on its total carbide volume fraction.

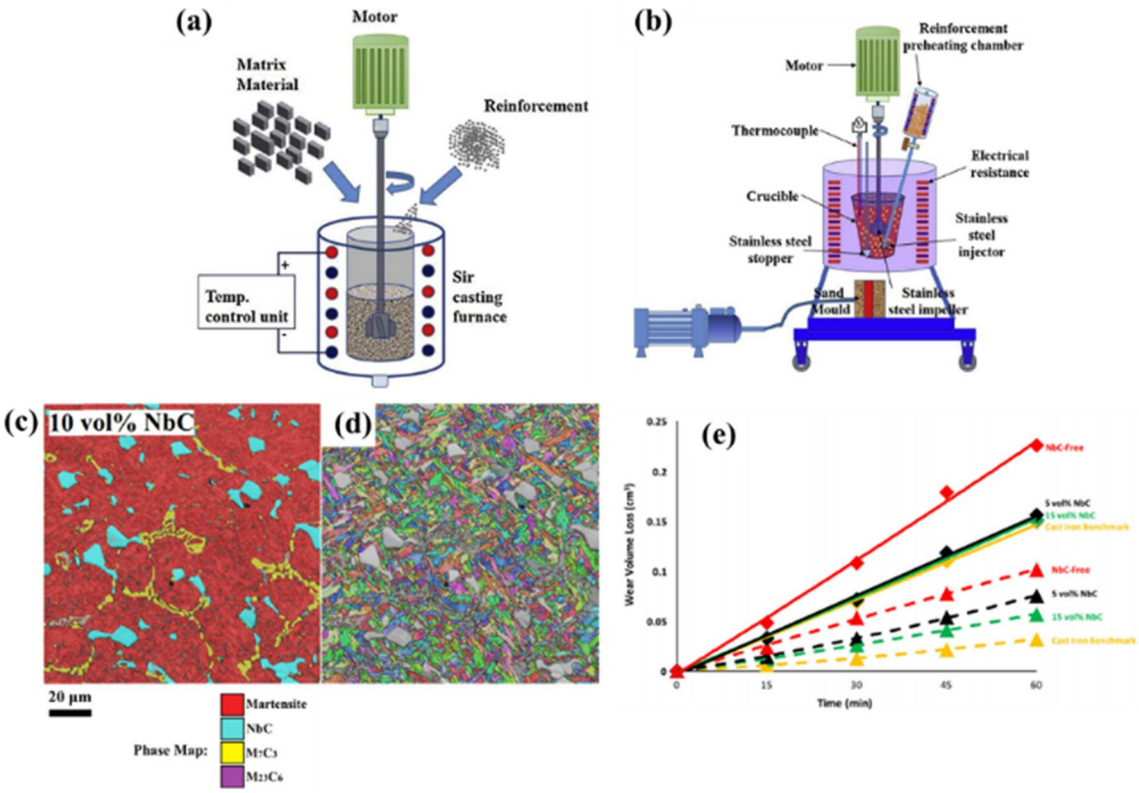

Fig. 16 Schematic illustration of **a** conventional casting apparatus with stirring function and **b** vacuum die casting [165]. EBSD maps of 10 vol% NbC reinforced AISI 440B composite: **c** phase present and **d** IPF map reveals the martensitic laths of the matrix. **e** Coriolis erosion wear test results [76]

However, the improvement of erosive wear performance was very marginal when NbC is increased to 15 vol%. These results also show that the garnet is expected to more effectively cut or fracture carbides in comparison to sand. NbC particles significantly enhance sliding wear performance of the steel by raising the adhesive wear resistance (when tested against SiC). Additionally, conventional casting offers a cost-effective method with relatively straightforward processing. It allows for a homogeneous distribution of reinforcements in the matrix. The disadvantages lie in the potential introduction of porosity and the tendency for reinforcement segregation.

3.2 Solid-State Processing Techniques

Incorporating reinforcements (fibers or particles) directly into the matrix and achieving uniform dispersion are extremely difficult. Instead, rather than introducing them directly, metal powder is utilized as the matrix metal. Reinforcements are mixed with the metal powder, and the resulting mixture is sintered to fabricate a composite. Numerous techniques have been advanced to execute these procedures, and some important methods are introduced in this section. The solid-state processing routes mainly include powder metallurgy (PM), spark plasma sintering (SPS), self-propagating high-temperature synthesis (SHS), diffusion bonding, exothermic dispersion (XD), and mechanical alloying (MA). The solid-state processing techniques could lead to a much more homogeneous distribution of reinforcements having a uniform size in iron matrix than the liquid-state processing techniques because the reinforcements usually show lower density than iron, density-induced-floatation cannot occur in the liquid-state process but it is almost inevitable in the liquid-state process.

3.2.1 Powder Metallurgy (PM)

PM is the technology of using powder as raw materials to manufacture metals, composites, and various types of products during forming and sintering [114]. The capacity to manufacture complicated geometry parts is one of the major advantages of the PM process. The majority process of this technique includes grinding raw materials into powder, pouring the powder into a certain mold, compressing it under a certain pressure, and sintering it into various types of products. The IMMCs fabricated by PM present good mechanical and physical properties with homogeneity [166]. Jha et al. [167] reported IMMCs by adding different weight

fraction (5, 10, 20, 30%) of ZrO_2 during PM procedure. Milling, compacting, and sintering the raw materials at a certain temperature range (900–1500 °C) for 1–3 h are the basic operations. The process parameters like sintering time and temperature have a significant impact on mechanical properties of the composite. Kumar et al. [168] synthesized iron-multiwalled carbon nanotubes (MWCNT) by PM technology. Several experiments were carried out in which the mixed powders, including Fe and MWCNTs, were pretreated using high-energy ball milling followed by conventional sintering. The results show that the high energy ball milling promotes uniform distribution of MWCNTs in the iron matrix. Furthermore, the carbides present at the MWCNT-iron interface due to high chemical affinity between carbon and iron. The conventional PM process is illustrated in Fig. 17a [169]. The general procedures of PM consist of mixing metal and reinforcement powders, compaction, and sintering [170]. Anal et al. [119] fabricated TiB_2 and Fe_2B particles reinforced IMMCs by mixing Fe_2O_3, TiO_2, B_2O_3, and Al powders and sintering them at high temperature. The composites show high hardness and density due to the reaction of composites formation is highly exothermic, essentially leads to self-propagating synthesis of composite.

Meher et al. [171] did some further work regarding MWCNTs reinforced IMMCs by milling in wet (toluene) and dry (argon atmosphere) conditions, followed by sintering. The effects of wet and dry milling on the microstructure and mechanical properties were investigated. Figure 17b and c show the SEM micrographs of wet-milled Fe-21MWCNT, with black arrows indicating the presence of porosity in case of wet milling. The number of porosities decreases when the sintering temperature changes from 900 to 1300 °C. Figure 17c illustrates the microstructure of wet-milled composite, with (Cr, oxide)-rich second phases that are spherical and black in the matrix. Cr is presented in composites due to the high chrome steel milling balls. Additionally, Cr plays an important role in hardening and strengthening of composites because of the strong bonding of Fe–Cr. Figure 17d shows compressive true stress–strain curves of both wet and dry milled composites sintered at 1300 °C. Obviously, the wet milled composite shows higher compressive strength compared to the dry milled composite due to higher densification. Due to uniform dispersion of reinforcement in matrix, the composite presents a maximum hardness and compressive strength of 450 VHN and 525 MPa, respectively.

As a common method among solid-state processing techniques, powder Metallurgy is celebrated for its precision in composition control and the capability of producing components close to their final dimensions, reducing the need for machining. However, it may not be the most economical choice for large-scale production due to the high costs of metal powders and necessary equipment [172].

3.2.2 Spark Plasma Sintering (SPS)

SPS is a novel sintering process in which the raw powders are first loaded in a conductive mold, after that the samples are immediately heated by a DC or AC current, and then

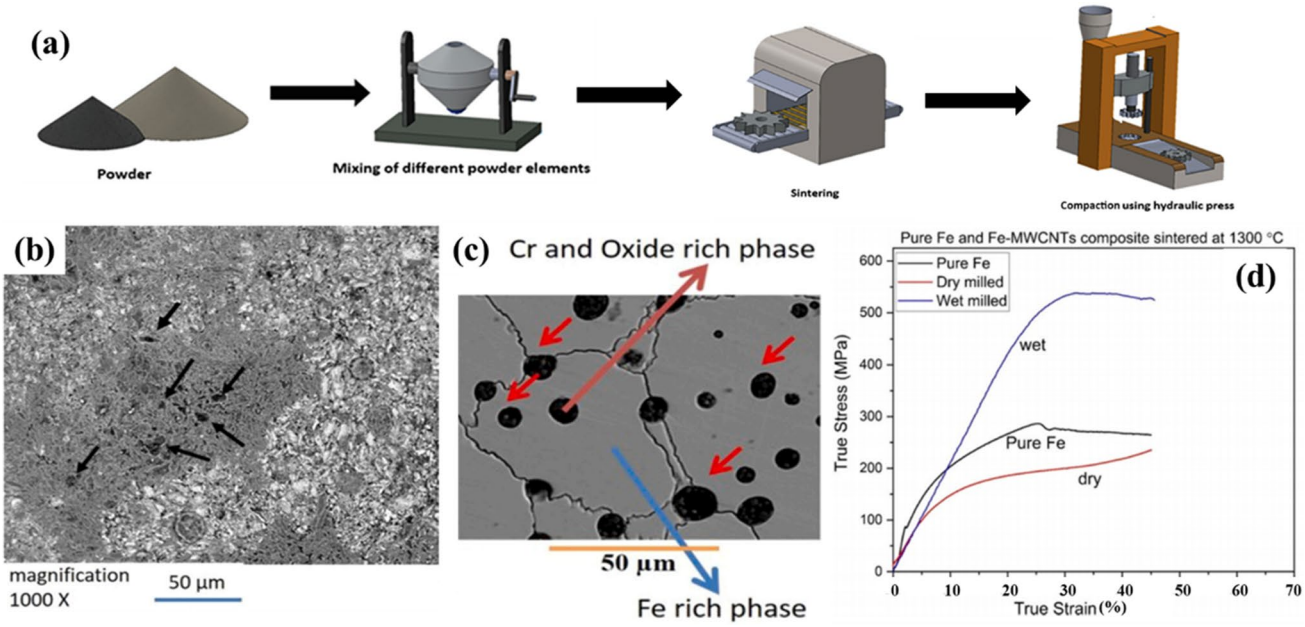

Fig. 17 **a** Powder metallurgy process [169]. **b** SEM micrographs of 21% MWCNT-Fe composite sintered at 900 °C, wet milling, black arrow showing the pores. **c** Distribution of the reinforcements in the Fe-matrix. **d** True stress–strain curves of both wet and dry milled composites sintered at 1300 °C [171]

sintered under a certain uniaxial pressure [173, 174]. SPS is also called field assisted sintering techniques (FAST) [175], pulsed electric current sintering (PECS) [176], and plasma pressure compaction (P2C) [177]. The main characteristics of SPS are the application of high heating or cooling rates, increasing material density, promoting diffusion mechanisms, and maintaining the intrinsic properties of nanoparticles in dense products [178]. SPS can result in achieving near-theoretical density at lower sintering temperature compared with conventional sintering techniques [173]. Due to the short sintering period, the prepared metal matrix composites can maintain a small grain size state. Although several studies have been carried out to reveal the details of SPS technology, the researches on microstructure and mechanical properties of IMMCs fabricated by SPS still lack.

A schematic illustration of the SPS configuration is shown in Fig. 18a [165]. The mixed powders are placed between an upper and lower punch connected with an on–off DC pulse generator, resulting in the generation of spark plasma, impact pressure, and joule heating. The powders were sintered and compacted as a result. The entire process can be divided into four stages according to the evolution of temperature and pressure. The combination of removing gases and creating vacuum is the first step. Afterward, to generate a compact and homogenous microstructure, sintering pressure is applied in the second stage, followed by heating in the third stage, and finally cooling in the fourth stage. Li et al. [179] fabricated TiC particulates reinforced Fe-based composite utilizing in situ SPS technique. Fe-Ti and carbon powders were first mechanically mixed before being sintered at high temperatures of 800–1200 °C through SPS system. Figure 18b shows the evolution of density and hardness with temperature during SPS process. The density and hardness of the material increased with the sintering temperature. The experimentally obtained composites can reach a dense density of 99.2% and a hardness of 790 HV as the sintering temperature increases to 1150 °C. Figure 18c shows the SEM image of microstructure of the fabricated specimen, in which the near-spherical TiC particulates with a size of ~ 1 µm are homogeneously distributed in the matrix. The TiC and BN-reinforced iron matrix composites fabricated by this method have been widely employed in tool steels, especially cutting tools, and have demonstrated remarkable wear resistance [30]. However, the IMMCs manufactured by SPS have small sizes and are limited by the tooling dimension, making them difficult to mass-produce in large quantities.

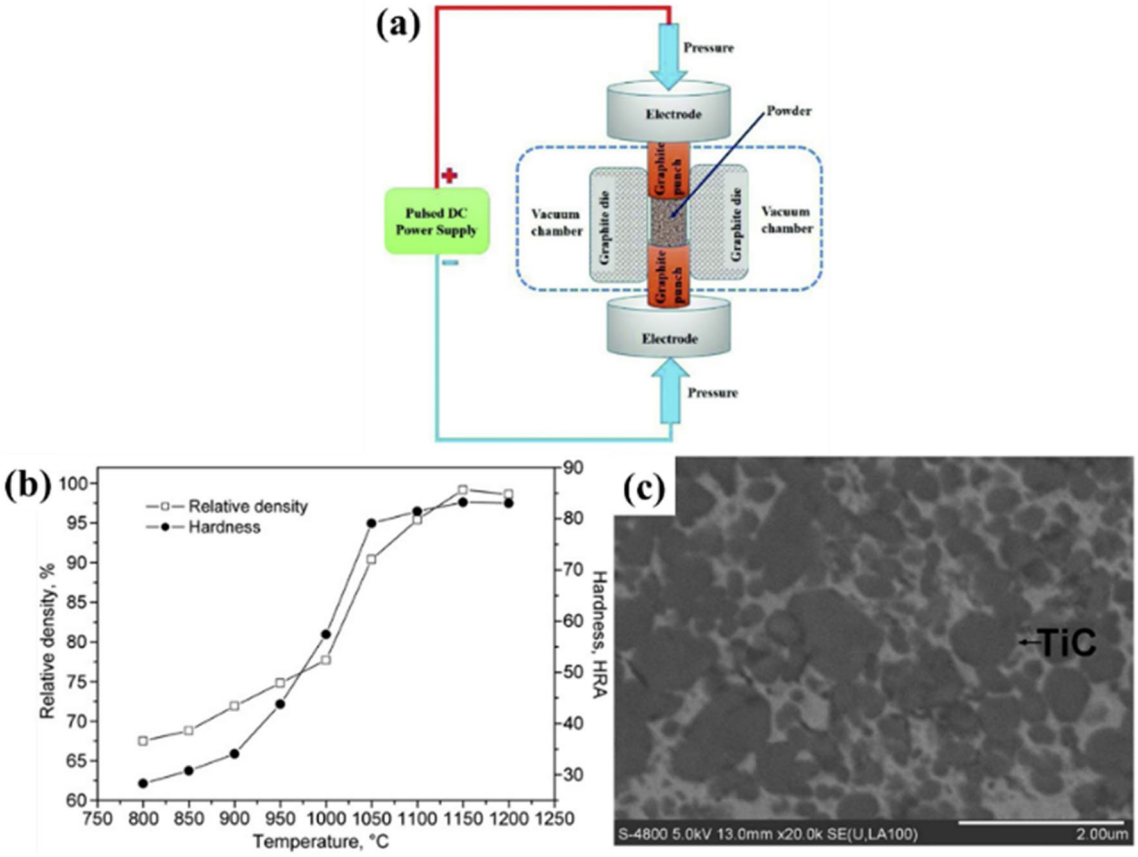

Fig. 18 **a** Schematic illustration of the SPS configuration [165], **b** the evolution of density and hardness with temperature during SPS process, **c** SEM image of the microstructure of the TiC reinforced IMMC [179]

3.2.3 Self-Propagating High-Temperature Synthesis (SHS)

SHS is a technique for synthesizing MMCs by exothermic combustion of reactants with different characteristics [180], also known as combustion synthesis [181]. This process involves exchanging exothermal reactions and self-conduction effect [111, 182]. The method can be briefly described as a process in which the initial reactants transform into products spontaneously when ignited, due to the exothermic heat of reaction. SHS process is ideally suitable for the fabrication of high purity composites due to the high reaction temperature generated through the sample [183]. Additionally, this procedure has several advantages compared with some traditional methods, such as simple equipment, fast productivity, and high purity of products [121]. However, SHS necessitates high costs, hardly controlled, and leads to problems with energy dissipation, thus it may not be suitable for mass production.

Zou et al. [184] used the SHS technique to create Fe-Al intermetallic/TiC–Al_2O_3 composites, focusing on the effects of preheating time, carbon sources, and heat treatment temperature on the synthesis. The reaction formula is: $3FeTiO_3 + 7Al + 3C \rightarrow 3Al_2O_3 + 3TiC + Fe_3Al$. They found that longer preheating times aid the formation of ordered intermetallic, and using graphite as a carbon source increases the reaction temperature. Heat treating at 750 °C effectively forms Fe_3Al intermetallic. Kalambaeva et al. [185] examined the effects of iron binder content on the structure of TiC reinforced IMMCs made using the SHS method. They noted that the burning rate and combustion temperature of SHS reaction, as well as the grain size of carbide particles, are influenced by the iron binder percentage. Higher combustion temperatures accelerate nucleus diffusion growth, requiring longer heating at high temperatures for effective diffusion mass transfer, which coarsens the composite structure. Additionally, the combustion temperature itself varies with the iron binder content, affecting the localized carbide distribution. Yang et al. [186] explored the impact of different molar ratios of in situ TiC/TiB_2 particles (2:1, 1:1, and 1:2) in IMMCs using the SHS method. Notably, at a 1:2 TiC/TiB_2 ratio, near-spherical TiC particles formed a framework structure. High reaction temperatures caused some gases and impurities to evaporate, leading to the formation of significant macro-porosity, which affected the density of the composites. The composite exhibited the highest hardness and wear resistance, at 46.3 HRC and a volumetric wear loss of 0.5463 10^{-10} m^3/m, respectively. This was attributed to the uniform distribution of TiC/TiB_2 particles within the steel matrix, enhancing the mechanical properties of IMMCs.

Figure 19a shows the schematic of the SHS process [46]. To fabricate IMMC using SHS, the iron and ceramic

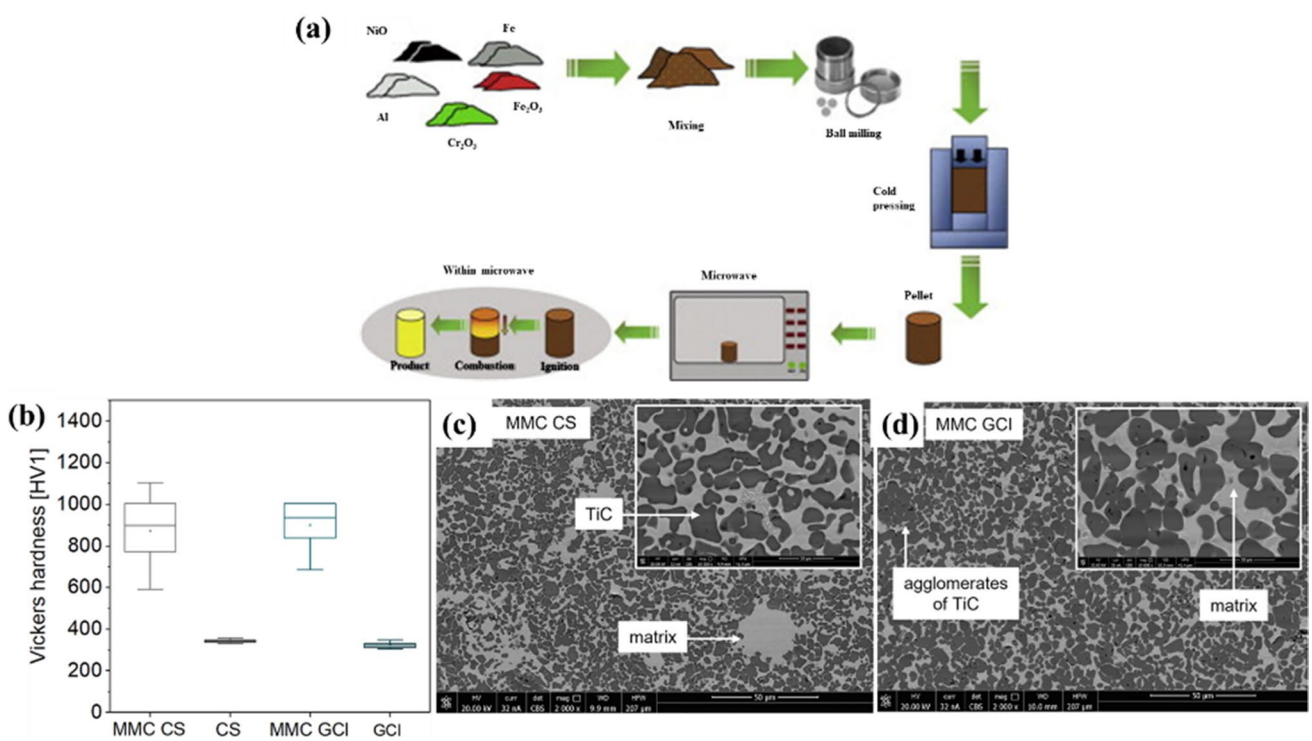

Fig. 19 **a** Schematic illustration of SHS processes [46], **b** results of Vickers hardness of composite layers and matrix. SEM images of **c** CS sample, **d** GCI sample [187]

powders are mixed together, compressed into a pellet, ignited with a high-energy heat source, and left to cool. As the procedure takes place at heightened temperatures, the method is superbly fitting for the creation of IMMC. The composites fashioned by SHS exhibit an absence of discernible cavities and pore structures, which alludes to the successful infiltration of the liquid metal into the green compact during the manufacturing process. TiC reinforced Fe-based composite were manufactured through the SHS process in order to enhance the abrasion resistance of low-carbon steel (CS) and gray cast iron (GCI) [187]. Figure 19b displays the outcomes of the hardness measurements performed within the in situ composite layers and chosen base alloys. Upon examination of the acquired hardness data, it can be inferred that the existence of TiC particles within the layer induced a hardness augmentation exceeding twofold in both instances. Figure 19c and d illustrates the infiltration of the base alloy into the region of the composite reinforcement, along with its partial fragmentation. In the instance of gray iron casting containing flake graphite, one can observe a microstructure that is representative of the hypoeutectic composition in close proximity to the composite layer (as depicted in Fig. 19c). The discrete TiC particles exhibit a size range of 2–4 μm and manifest coagulated morphologies in the form of agglomerates that are conjoined through an alloy.

3.2.4 Diffusion Bonding

Diffusion bonding is a novel manufacturing solid state process and one of the most widely employed techniques for facilitating IMMCs [188, 189], it is also called diffusion welding [190]. There is no contamination from the diffusion bonding process, and the composites endure very little deformation and residual stress [191]. The basic principle of this method includes three stages: two surfaces of reactants contact and plastically deform, raw materials migrate during the heating process, and materials diffuse across the boundary of adjacent surfaces and create a bond. The main characteristic of diffusion bonding is that it can fabricate composites with high-quality joints. The disadvantages of this method are also visible, such as the size of products being limited by the equipment, low productivity, and high requirements for preparation [192]. This process is commonly used to fabricate materials that are difficult to weld.

Avettand-Fènoël et al. [193] have studied the mechanical properties of graded IMMCs during brazing and diffusion bonding. There are some micrometers thick continuous oxides (TiO_2, $Fe_2Ti_3O_9$, and $FeTiO_3$) layers found at the joint of composite. The joint with good bending resistance was developed by brazing and diffusion bonding. Hasan et al. [194] investigated the bonding characteristics between WC-8Co and stainless steel matrix which are bonded by hot compaction diffusion bonding (HCDB). The schematic diagram of HCDB is presented in Fig. 20a, the WC-8Co powder and SS304 are placed in an insulated die mold, then an electrical current flows from one end to another and heats the sample in order to promote the compaction of two materials. The specimens were examined under SEM (Fig. 20b) for grain boundaries and grain size analysis, where it is difficult to identify the boundaries. The grains with different sizes are

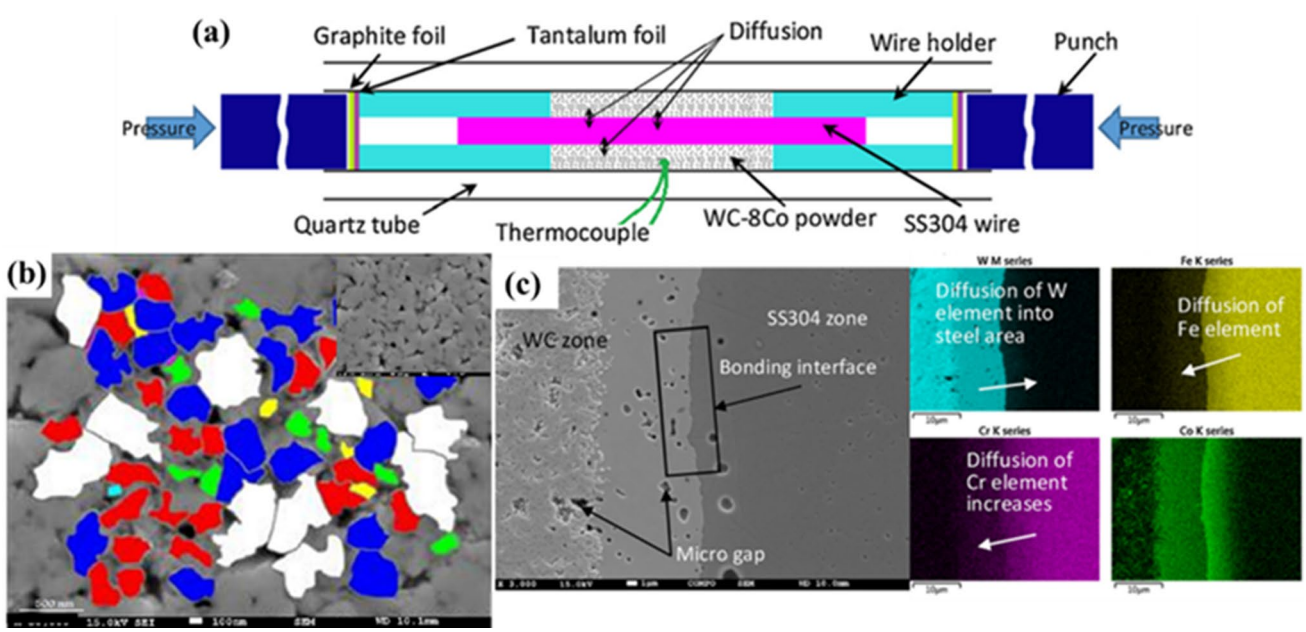

Fig. 20 **a** Schematic diagram of hot compaction diffusion bonding, **b** SEM graphic of grain boundaries and grain size, **c** SEM–EDS images of bonding interface of WC-8Co-steel sintered at 1220 °C [194]

marked in blue, white, and red. The WC-8Co sintered at 1220 °C has an average grain size of 271 nm and a maximum size of 543.3 nm. As a result, the final product with fine grain, and uniform morphology of bonding interface was produced in a short time, as evidenced by the SEM–EDS images of bonding interface in Fig. 20c. Diffusion of Fe and Cr into the WC area, and a small amount of W into the steel area can be observed significantly. The diffusion of elements proves the successful bonding between WC-8Co and SS304 during diffusion bonding. However, some micro-gaps are found in the interface. This phenomenon is common in sintering. The micro-gaps can be eliminated by increasing the sintering temperature.

They continued to investigate WC-10Co and high strength AISI 4340 steel using diffusion bonding process [195], where the ceramic was used in powder form and the steel as solid. The microstructure of the composite shows that the sample has no visual cracks and is densified with a bit of porosity. In this research, the bonding shear strength of the interface is slightly higher than in previous studies.

3.2.5 Exothermic Dispersion (XD)

XD is an in situ process that can fabricate IMMCs and is derived from the combustion synthesis process [122, 196]. The key of this technology is to control the size, shape, and volume fraction of the reinforcement phase. The interface bonding of composites synthesized by XD process is extremely strong. This technique is one of the effective processes for synthesizing IMMCs. The final products fabricated by this process, however, have large porosity and are often pressurized during the reaction process to increase the density.

The schematic diagram of XD technology is shown in Fig. 21a [197]. The reactants *X* and *Y*, as well as metal element *A*, are heated in this process. The reaction between *X* and *Y* is exothermic and reinforcement particles are formed in the metal matrix. Zhu et al. [198, 199] have studied the TiC/Fe composites fabricated by XD. The process of exothermic dispersion comprises four stages: a) mixing three kinds of powders (the pure Fe, Ti, and C), b) compacting and heating the mixed powder, c) the radiation reaction occurs, and the reactants absorb thermal energy from the melt, d) in situ TiC formation in composite. The reaction can be described as: $Ti + C \rightarrow TiC$. To comprehend the time-dependent of this reaction, the reaction rate was examined and compared based on differential scanning calorimetry (DSC) curves (Fig. 21b) obtained at different heating rate. In summary, the results indicate an increase in the reaction rate with the elevation of the heating rate. The SEM micrograph is shown in Fig. 21c, in which the fine TiC particles (black region) are distributed uniformly in the matrix. After the dry wear sliding test, the change in mass loss of the composite material with the applied load at a sliding speed of 0.6 m/s and sliding distance of 200 m. It can be observed that, under the same test conditions, the mass loss increases with the

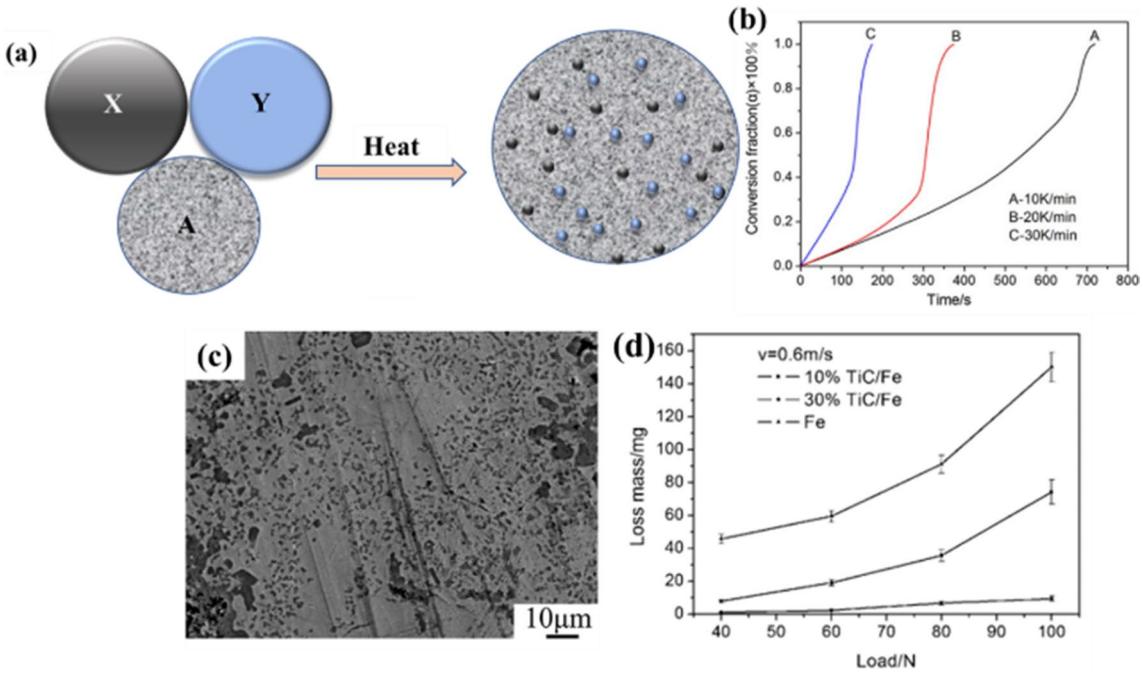

Fig. 21 **a** Schematic diagram of XD process [197], **b** DSC curves obtained at different heating rate, **c** SEM micrograph of the composite containing a volume fraction of 30% TiC, **d** the load-loss mass curves [198]

rising of the applied load, and greatly decreases with the increase of the reinforcement volume fraction, indicating that the wear resistance of the composites increases significantly (Fig. 21d).

3.2.6 Mechanical Alloying (MA)

Mechanical alloying (MA) is a complex powder processing technique in which solid-state alloying is achieved using high-energy grinder or ball mill. The procedure of this method involves repeated deformation, cold welding, and fracturing in a high-energy ball mill to achieve homogeneous material with atomic-level alloying. MA technique allows the oxides and carbides to coat the metal substrates directly, it has been used to produce a wide range of materials. Therefore, the high temperature strength and creep resistance of the composites are significantly improved through the MA process [200].

Saba et al. [201] used mechanical alloying (MA) to deposit a well-bonded TiC coating on AISI D2 steel substrates from titanium and carbon powders and elucidate the formation mechanism of deposited TiC coating by MA in detail. The mechanism of alloying during MA process is shown in Fig. 22a. First of all, various metal powders are mixed in the ball mill. Second, the powders fracture and bond together by diffusion under the impact of balls, resulting in alloy powders. Finally, the dispersed phase can result in strengthening of the particles or can impart special properties of the powder [202]. The microstructure, chemical composition, and nanocrystalline have been investigated through SEM, EDS, and TEM, respectively. Figure 22b illustrates the surface profile of the TiC coating on the hardened steel substrate at 35 h. The coating roughness is relatively low with the BPMR of 50:1. Figure 22c represents SEM image of the composite, which demonstrates that the TiC (black region) particles are distributed in the matrix uniformly. During MA process, the reinforcements are cold welded to the hardened substrate. A chemical reaction occurs during the mixing of powders and matrix materials, which can result in the formation of the composite layer. This intermixing can be attributed to the strong bonding between TiC and steel matrix.

3.3 Gas-Mixing Processing Techniques

3.3.1 Vapor–Liquid-Solid (VLS)

The gas-mixing processing technique was invented by Koczak in 1989 [203]. The basic principle of the method is typically described in three stages [204]: 1) using an inert

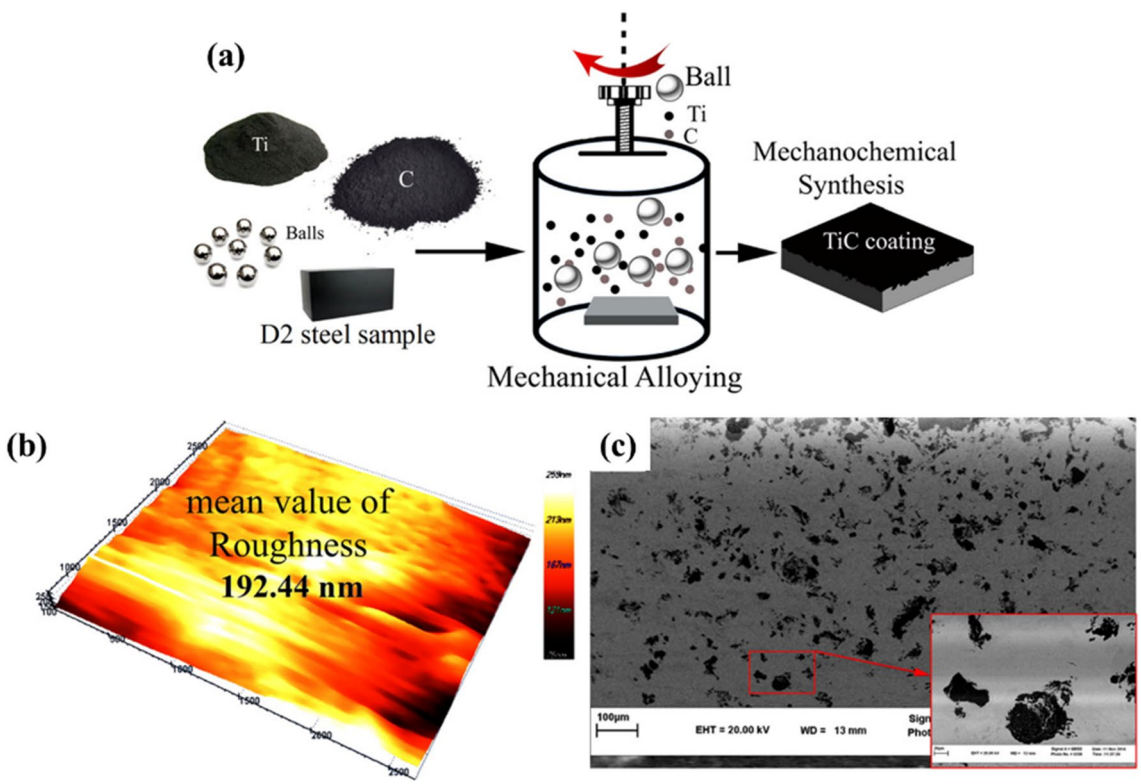

Fig. 22 **a** Schematic diagram of MA process, **b** surface profile of the TiC coatings at milling duration of 35 h, BPMR of 50:1, hard substrate, **c** SEM image of the composite [201]

gas as a carrier, passing reaction gas with components of reinforcement into high-temperature liquid metal; 2) the elements decomposed from the reaction gas react with metal; 3) the desired reinforcement produced in matrix. The reaction rate of reinforcement generation through adsorption of gas phase on solid phase is generally very slow during VLS process. The introduction of catalytic liquid alloy phase can circumvent this. There are many researchers investigated the MMCs fabricated by VLS method [205, 206]. However, the efficiency of this method is excessively low, and it has not attained widespread application.

The schematic diagram of the VLS process is shown in Fig. 23 [123]. The process generally includes the decomposition of the gas, chemical reaction of the gas and metal, and formation of reinforcements. Lu et al. [116] prepared in situ Al_2O_3 fiber reinforced Fe-Al composites by oxidizing oxygen to Fe and Al powder, and Al_2O_3 fibers were synthesized via the VLS process. The reaction of Al_2O_3 formation can be described as: $2Al_{(g)} + 3/2\ O_{2(g)} \rightarrow Al_2O_{3(s)}$ and $2Al_{(s)} + 3/2\ O_{2(g)} \rightarrow Al_2O_{3(s)}$. During the reaction, a part of Al will be transformed into gas state due to its low melting point. When the Al content is up to 60%, a great amount of Al_2O_3 fibers is formed. The excessive Al contents allow the generation of abundant Al_2O_3 fibers as there is enough gas and liquid Al present to participate in the in situ reaction. The microstructure of composite is denser and the shape of the crystals has a sheet microstructure because the alumina fibers appear in the pores of the materials.

3.3.2 Spray Deposition

Singer and Ozbek introduced spray deposition as a gas-mixing technique in 1985 [207]. This process consists of spraying semi-solid droplets and depositing onto shaped substrate. The specific procedures of this technique can be described as: a high-pressure gas is used to atomize alloy liquid into tiny droplets, which are then cooled in a high-velocity airflow before being deposited into a billet. Spray deposition offers various advantages, including fine grain size, uniform organization, and no macro-segregation of composite materials. Thermal spraying and cold spraying are two extensively utilized spray processes in the field of spray deposition technology [208, 209]. The use of smaller size of particles in cold-sprayed coatings resulted in increased reinforcement particle retention [210]. Lampke et al. [209] have developed particle reinforced high-alloyed steels in the field of thermal spraying and the deposited coating exhibit good wear resistance because of low porosity and high microhardness. The deposition efficiencies of different powders in cold spray process were measured by Chu, and discovered that the mixed powder had higher deposition efficiency [124]. The schematic diagram of cold spray deposition process is shown in Fig. 24a, in which the raw materials were fed separately, mixed before the spray gun to obtain desired compositions, and injected into high pressure region of the gun for co-deposition [124]. Ksiazek et al. [211] studied a WC–Co + Ni composite coating on ductile cast iron, applied via cold spray after sandblasting. Despite incomplete particle melting, the coating-maintained fracture resistance and cohesion during bending tests. Ni addition improved crack resistance and wear behavior, with TEM showing a nanocrystalline structure of elongated WC 50–100 nm-thick bands of WC particles arranged in parallel.

Chu et al. [212] crafted amorphous composite coatings of TiN/Fe-based with varying ratios through reactive plasma spraying. Furthermore, during the reactive plasma spraying process, TiN served as the reinforcing phase. The surface morphology of the 10% TiN/Fe-based amorphous composite coating is depicted in Fig. 24b. The gray region (marked A in Fig. 24b) denotes the Fe-based amorphous phase, while the black region (marked B in Fig. 24b) indicates TiN. TiN is uniformly distributed within the Fe-based metallic matrix. To delve deeper into the bonding microstructure between the Fe-based amorphous and TiN, TEM analysis was conducted on the coating. The bright-field image (as depicted in Fig. 24c) displays the morphology of the coating with two phases—the Fe-based amorphous phase and the TiN phase. From the figure, it can be observed that the two phases are intimately linked with no obvious structural defects. The TiN phase is made up of nano-scale grains owing to the rapid cooling of the TiN melted droplets during the coating preparation process. The high-resolution images (as depicted in Fig. 24d) indicate the presence of a transition layer between the Fe-base amorphous phase and the TiN ceramic phase, which suggests a robust bonding between the two phases. These findings further validate that no crystallization occurred in the amorphous phase during the plasma spraying process, and the amorphous characteristics are outstanding. In summary, gas-mixing methods for preparing IMMCs offer high purity and precise control over

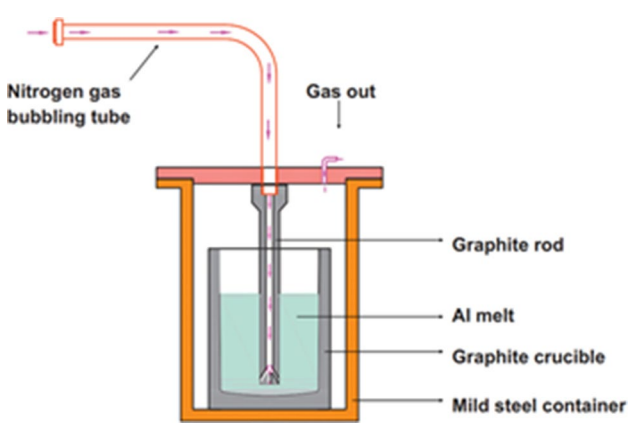

Fig. 23 Schematic diagram of VLS process [123]

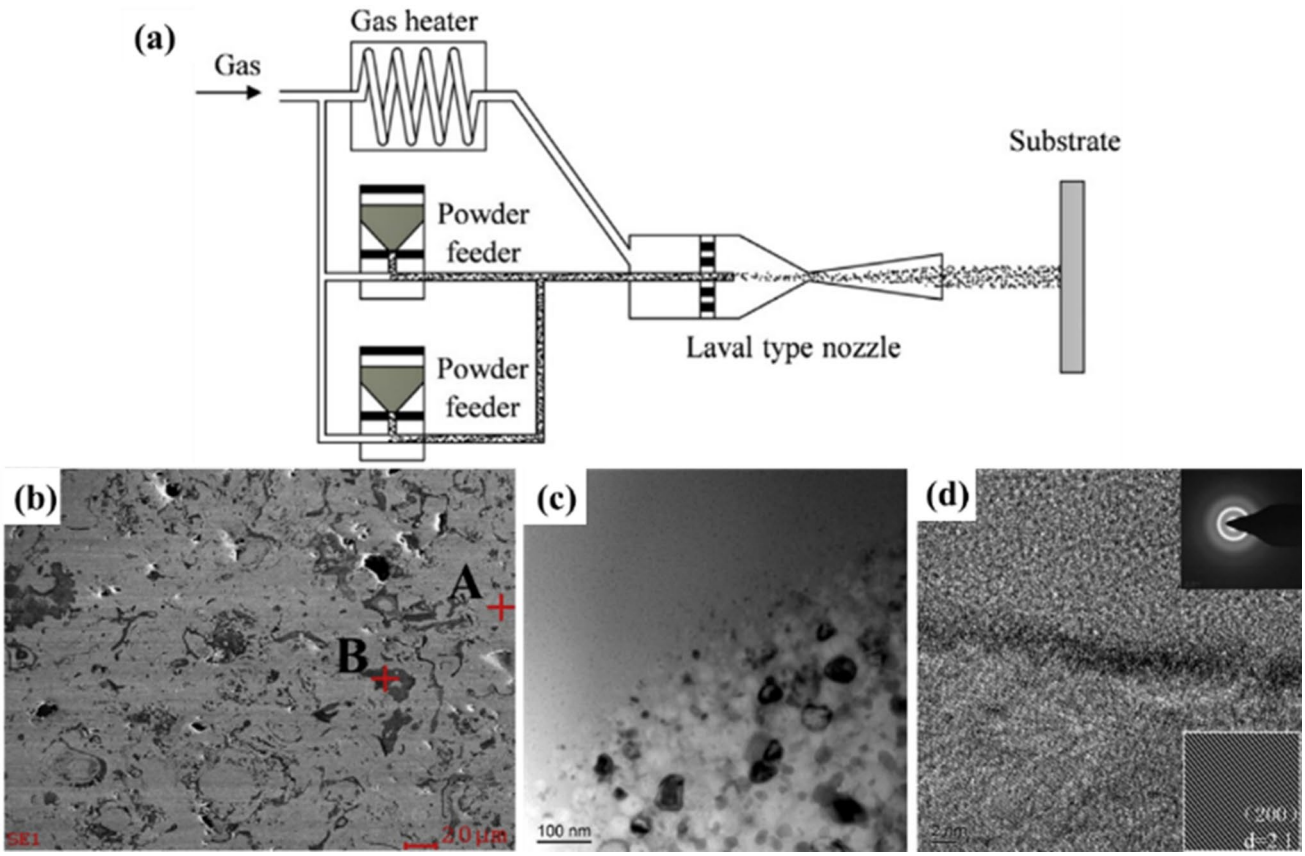

Fig. 24 **a** Schematic of the cold spray deposition process [124]. **b** Surface morphology of the coating with two phases. TEM images of Fe-based amorphous phase and TiN phase: **c** bright-field image, **d** high-resolution images [212]

microstructure. However, they are costly and complex, best suited for thin film applications rather than bulk production. These techniques provide uniform, defect-free coatings but require specialized equipment and are not ideal for large-scale manufacturing due to slow deposition rates.

4 Mechanical Properties of IMMC

Depending on the targeted applications, a balance must be struck between mechanical, chemical, and physical properties of IMMCs. The final mechanical properties of the IMMCs are determined by the shape and properties of the reinforcements, their distribution and volume fraction and the bonding strength of the reinforcement/matrix interface [213]. In the recent years, a great quantities of studies have been carried out about mechanical properties of IMMCs [214]. The elastic modulus, tensile behavior, hardness, and wear resistance are discussed in order to better understand how different reinforcements influence the mechanical properties of IMMCs. Some properties of IMMCs, such as tensile strength, are typically associated with the interface between constituents, rather than the performance of the matrix and reinforcements. Conversely, properties like hardness and wear resistance are determined by a weighted sum of the constituents [215, 216]. In this chapter, the mechanical properties, and fundamental principles of IMMCs are introduced in detail.

4.1 Elastic Modulus

In designing some engineering parts, the elastic strength is more essential than the ultimate tensile strength due to such mechanical parts should have high resistance to yielding [25]. The elastic modulus of an object is a parameter that measures its resistance to being elastically deformed when stress is applied to it [217]. The elastic modulus of MMCs is usually measured by Young's modulus [218], Bulk modulus [219], Rigidity modulus [220], and Poisson's ratio [221]. Equation (2) can predict the Young's modulus of composite reinforced by ceramics with regular shape. In addition, the Poisson's ratio (v) of IMMCs is influenced by the properties of both the matrix and the reinforcement. Specifically, Poisson's ratio is defined by Eq. (3):

$$\nu = -\frac{\varepsilon_{\text{transverse}}}{\varepsilon_{\text{axial}}}. \quad (3)$$

where $\varepsilon_{\text{transverse}}$ is the transverse (perpendicular to the loading direction) strain of the composite, $\varepsilon_{\text{axial}}$ is the longitudinal (loading direction) strain. It should be emphasized that, although the modulus prediction by equations aligns well with experimental data, there is no reason for expecting it to be highly accurate. Fabrication problems are anticipated to diminish the properties of composite, including factors such as fracture and degradation through chemical reactions of the reinforcement.

Chen et al. [222] fabricated high modulus steel reinforced with boride and carbide through the conventional casting process. The results demonstrated that Young's modulus of hot rolled composites increased from 216 to 248 GPa compared with unreinforced steel, due to the addition of a high modulus reinforcing phase. Xiong et al. [223] designed TiB_2–Fe metal matrix composite that showed a good combination of high modulus (~ 205 GPa), yield strength (881 MPa), and ductility (31%). However, the modulus of unreinforced steel of 190 GPa. The mechanical properties of the composite can be attributed to the impressive metallurgical bonding of the TiB_2/Fe interface and heterogeneous microstructures. Rana et al. [224] have investigated the effects of TiB_2 ceramic particles and alloying elements (Al and Mn) on the elastic modulus of IMMCs. The composites were fabricated by standard processing routes of liquid steel metallurgy. All of the results indicate that the composite has a significant density drop of 12.7%, and TiB_2 in the composite increased the elastic modulus by 19%, when the fraction of TiB_2 is 13 vol%.

Wang et al. [5] have studied the elastic modulus of high-modulus steels (HMSs) reinforced by different TiB_2 fractions. The authors designed possible solidification sequences by considering various morphologies and sizes of TiB_2 particles under different solidification paths. Figure 25a displays the SEM image of composite. Some Ti (CN) particles can be found at the center of the TiB_2 particles. In addition, these coarse TiB_2 particles may have nucleated at the Ti (CN) particles that had previously formed. Moreover, a more rapid solidification rate could lead to the finer size of TiB_2 particles and suppress the agglomeration of particles. It can be seen in Fig. 25b that the elastic modulus of HMS is indeed higher than pure iron ($E = 210$ GPa). The Young's modulus did not increase, and the TiB_2 fraction did not follow the calculated linear. The reason is that Young's modulus could be affected by the shape, distribution, and size of the particles, not only the particle faction.

4.2 Hardness and Wear Resistance

The hardness and wear properties are among the ultimate properties for IMMC considering its wide application as wear resistant materials [225]. The hardness of IMMC increases by adding the reinforcement particles with high hardness (TiC, SiC, WC, TiB_2, and so on). The IMMC possesses high hardness because of the intrinsic metallurgical bonding between the matrix and reinforcement phases [226]. Furthermore, wear resistance is one of the most important concerned properties of IMMCs in terms of their practical applications. Factors affecting the wear resistance of IMMCs include: the matrix, reinforcements, reinforcement/matrix interface, and morphology, size and volume fraction of the reinforcement phases in the composite [227, 228].

Razavi et al. [229] investigated the feasibility of the TiC particles reinforced IMMCs melted using the mechanical alloying technique. With the addition of 0.96% TiC, the hardness increases from 195 ± 2 to 205 ± 2 Brinell. Gupta et al. [230] reported the investigations on the hardness behavior of Fe-Al_2O_3 composites prepared by powder metallurgy. The results show that the nano iron aluminate

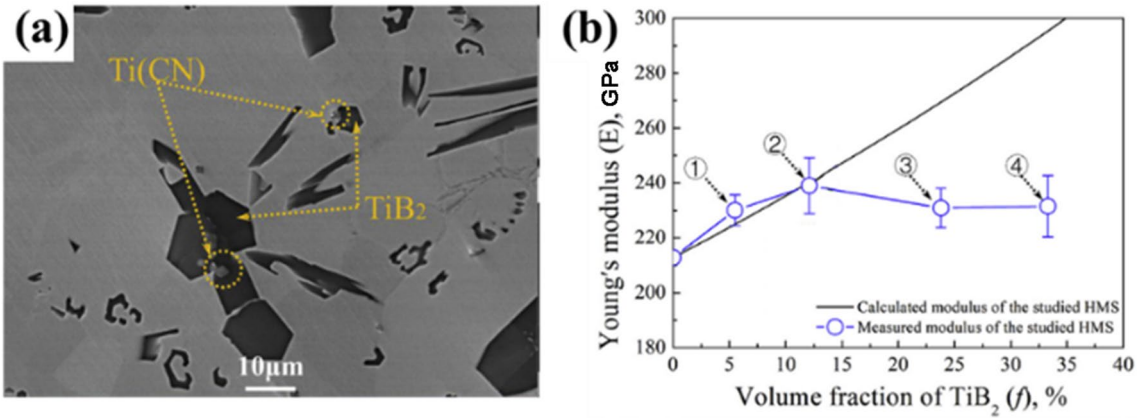

Fig. 25 **a** SEM image of the microstructure of the IMMC showing the distribution of Ti (CN) and TiB_2 particles in steel matrix, **b** comparison of the calculated and measured modulus of the studied HMS as affected by the volume fraction of TiB_2 [5]

($FeAl_2O_4$) forms in the matrix during sintering. The hardness of composites increases significantly when sintering temperature and volume fraction of Al_2O_3 increase. Additionally, it is noteworthy that the hardness value of cast iron was found to be 18 HRH which indicates that the hardness of composites was considerably higher than cast iron.

Bai et al. [231] designed a novel V–V_8C_7/Fe core–shell rod-reinforced iron-based composites, and fabricated the composites via a two-step in situ reaction. Ideally, the high strength and hardness of composite have been obtained, and its performance is derived from the mutually reinforcing impact arising from the substantial toughness exhibited by the metallic V-core and the gradient distribution structure of the V_8C_7/Fe-shell layer. Notably, a compact annular layer of V_8C_7/Fe enshrouds the residual V wire, thus giving rise to the V–V_8C_7/Fe core–shell rod. Hence, the iron-based composite reinforced with V–V_8C_7/Fe core–shell rods is comprised of gray cast iron and V–V_8C_7/Fe core–shell rods. In order to gain further insight into the microstructure and morphology of the composites as well as the different forms of vanadium, the distinct regions of the iron-based composite were examined through the utilization of EBSD and SEM techniques. Figure 26c presents the EBSD band-index micrographs of zone I, as exhibited in Fig. 26a. The principal phases present in the composite comprise V_8C_7, V_2C, V, α-Fe, and the phosphorus-rich phase. The microstructure of zone II, illustrated in Fig. 26d, displays elliptical V_8C_7 particles with an average size of approximately 7.2 µm. Figure 26e shows the microstructure of zone III, featured in Fig. 26a. Some V_8C_7 particles have developed into square shapes, with an average grain size of approximately 8 µm. Furthermore, the microstructure is notably distinct from the morphology of zones I and II. The distribution of hardness in the composite is presented in Fig. 26b. The V-core demonstrates a hardness of approximately 457 HV0.2. Moving from the interface between the V core and the V_8C_7/Fe-shell layer to the cast iron substrate, the hardness of the V_8C_7/Fe shell layer gradually decreased from around 1296–573 HV0.2. This gradual variation in hardness can be ascribed to the development of the gradient microstructure of the vanadium-carbide volume fraction and grain size in the V_8C_7/Fe-shell layer. Evidently, in comparison to the cast iron substrate (~418 HV0.2), the hardness has been significantly enhanced.

Zhang et al. [232] fabricated a IMMC with 30 vol% WC by SPS. The wear resistance tests results indicated that the specific wear rate of in situ composite decreased from 2.2×10^{-4} mm^3/Nm in the martensite steel matrix to 2.5×10^{-5} mm^3/Nm in the IMMCs. Srivastava et al. [74] prepared a Fe-17Mn austenitic steel composite by adding 10% TiC using conventional casting method and studied its wear resistance properties. Figure 27a and b shows the SEM micrograph of the microstructure of the IMMCs reinforced by TiC and (Ti, W)C, respectively. The plots of volume loss and wear rate versus sliding distance are shown in Fig. 27c and d, respectively. The TiC or (Ti, W)

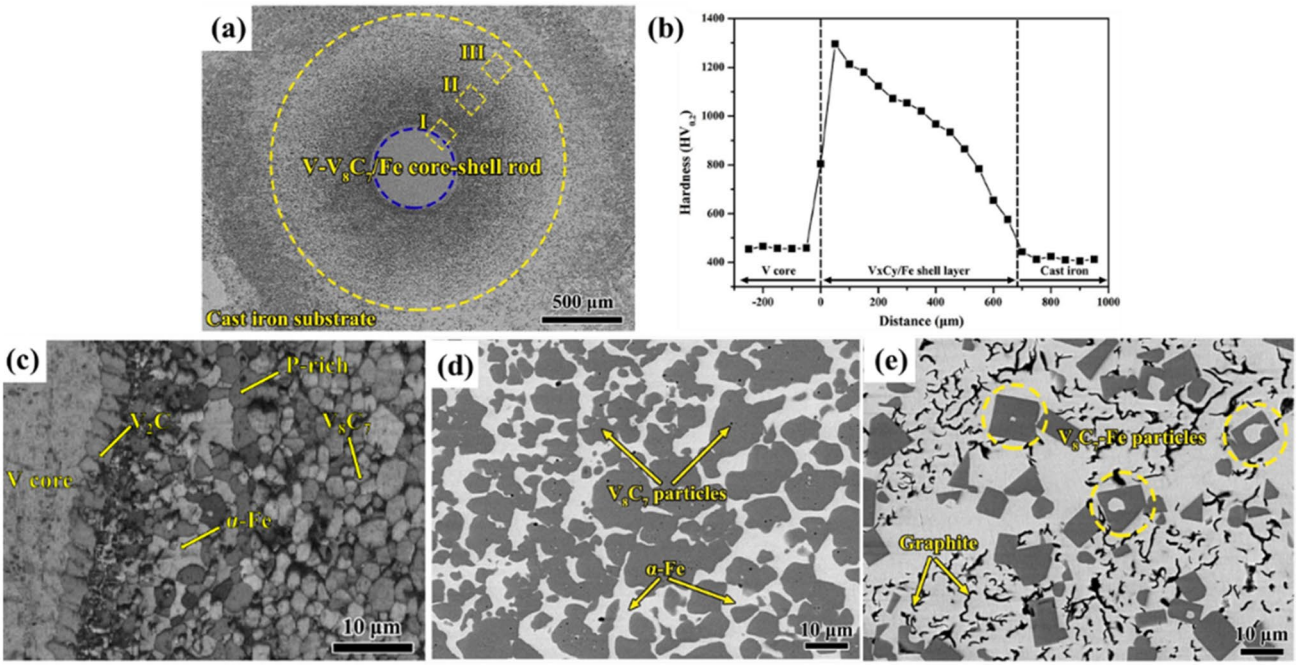

Fig. 26 **a** Overview of microstructure of the V-V_8C_7/Fe composite. **b** The distribution of hardness in the composite. **c** EBSD band-index micrographs of zone I. Microstructure of **d** zoon II, **e** zoon III [231]

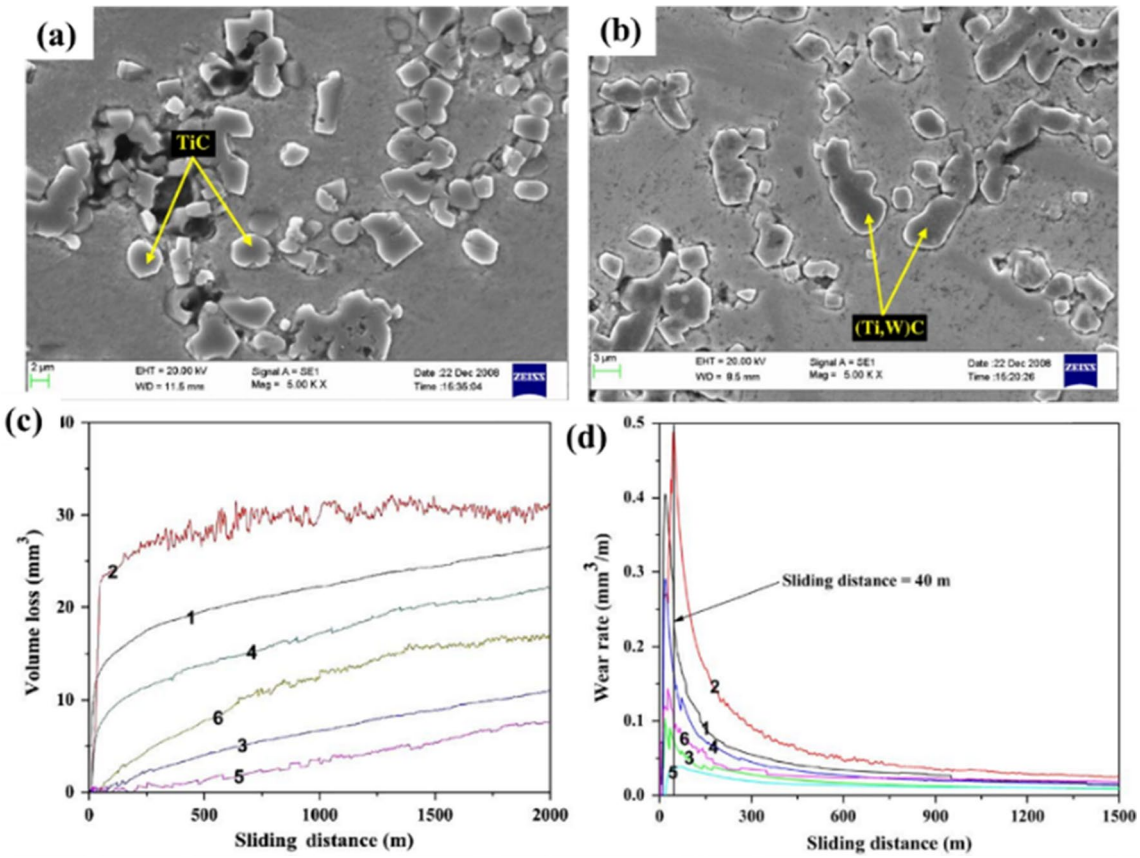

Fig. 27 SEM micrographs of the microstructure of the **a** TiC and **b** (Ti, W) C reinforced Fe-17Mn austenitic steel matrix composite. **c** Volume loss, **d** wear rate versus sliding distance for the unreinforced steel (1 and 2), TiC-reinforced composite (3 and 4), and (Ti, W) C-reinforced composite (5 and 6) [74]

C-reinforced composite materials exhibit lower volume loss and wear rates compared to that of the Fe–17Mn austenitic steel. The wear rates of high manganese austenitic steel and TiC or (Ti, W) C-reinforced composite are ~ 0.35 mm^3/mm and ~ 0.22 mm^3/mm, respectively, on the condition of the sliding distance of 100 m. The decrease of wear rate can be attributed to the load-bearing capability of the in situ formed TiC and (Ti, W) C particles as shown in Fig. 27d.

Liao et al. [233] prepared IMMCs with mass fraction of 30–50 wt% WC by gravity and infiltration and studied the wear properties of the composites comprehensively. Figure 28a and b shows the microscopic SEM morphology of the composites with WC content of 40%, the white and gray region correspond to the WC and matrix, respectively. The result of EBSD phase analysis for the WC is shown in Fig. 28c. The presence of 40% WC suggests that the particles interdiffusion with the metal matrix, forming an interface composed of Fe_6W_6C. This phenomenon arises from the decomposition of WC initiated by the metal liquid when the WC content is excessive. Then, the wear resistance of the composites was tested at room temperature. Figure 28d depicts the curves illustrating the coefficient of friction (COF) for the WC composites with varying contents over time. The average COF for WC content of 40% was 0.52, and the average friction coefficient exhibited a pattern of initially increasing and then decreasing with the rise in WC contents. The addition of 40% WC resulted in the highest average COF among all contents, attributed to its uniform dissipation and incomplete dissolution. Figure 28e shows the average wear rates of different composites. The results show a trend of increasing and then decreasing with the increase of WC contents, and are consistent with the findings from the friction tests.

4.3 Tensile Behavior

High strength is typically a target property of IMMCs development. Likewise, the main selection criterion for loading bearing materials is their strength which can be determined by tensile tests. Nevertheless, the strength of composites is subject to numerous influencing factors, making it exceedingly challenging to precisely estimate. The yield strength and ultimate strength are determined by network structure, microstructure, solution effects, and compatibility of

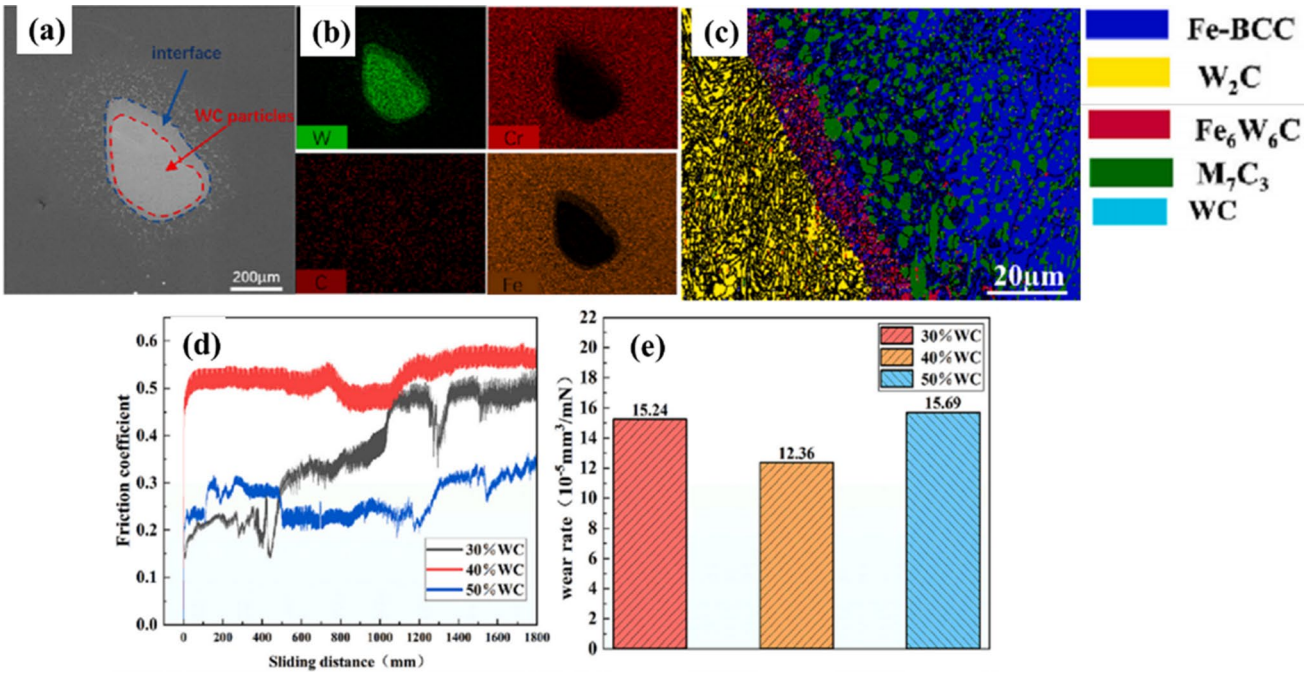

Fig. 28 **a** SEM, **b** EDS image, and **c** EBSD phase composition diagram of 40% WC, **d** friction coefficient, and **e** wear rates of all composites [233]

reinforcement and matrix [234, 235]. During deformation process, the movement of dislocations commonly causes the plastic deformation in composites [236]. Several theories have been proposed to explain the strengthening mechanism attributed to the increased dislocation density. For instance, the strengthening due to dislocation density leads to the yield strength of materials being proportional to the square root of the dislocation density (Eq. (4)):

$$\tau = \tau_0 + \alpha G b \rho^{-\frac{1}{2}}. \tag{4}$$

where τ is the stress at which the material begins to deform plastically, considering dislocation strengthening, τ_0 is the yield stress without considering dislocation strengthening, α is a constant of 0.5, G is the shear modulus, b is the Burgers vector, ρ is the dislocation density. The tensile strength of composites increases with a certain range of reinforcement phase content and reinforcement particle sizes [112, 237].

Li et al. [218] evaluated the impact of ceramic particles (SiC, Cr_3C_2, TiC, Ti(C, N)) on the mechanical properties of IMMCs. SiC particles notably enhanced composite strength due to their high hardness and minimal decomposition, which promotes pearlite formation in the ferrite matrix. The optimal yield strength was observed at 10 vol% reinforcement, with further increases leading to particle agglomeration and reduced effectiveness. Guan et al. [19] showed that the yield strength and ultimate tensile of 3 wt% SiC reinforced 316 L stainless steel increased significantly, 49.4% and 38.6% improvement, respectively. Zhao et al. [238] studied nanocrystalline TiC-reinforced 316L stainless steel composites, finding that 2 wt% of 40 nm TiC particles, with prolonged exposure time, increased tensile strength by 19% and microhardness by 27% compared to pure 316 L. Additionally, research on IMMCs with varying sizes of SiC particles via hot-press sintering [239] showed that denser composites with minimal voids and preserved particle size increase strength. SiC particles of 13 μm particularly enhanced yield stress and tensile strength more than other sizes.

Song et al. [240] fabricated the fully dense SiC reinforced IMMC via SLM process. TEM micrographs and corresponding SAD patterns of the specimens produced by selective laser melting (SLM) using Fe/SiC are illustrated in Fig. 29a. These micrographs provide evidence of the presence of sub-micron sized iron grains, amorphous iron, and retained micro-scaled and nano-sized SiC particles. The formation of nano-sized Fe can be explained by a preferential nucleation in the vicinity of the retained nano-SiC particles. In contrast to the as-fabricated pure iron sample, the as-fabricated composite specimen undergoes three obvious deformation stages, as depicted in Fig. 29b. The ultimate tensile strength (UTS) of the pure iron sample hardly reaches 357 ± 22 MPa after 9% strain, whereas that of the composite material increases dramatically from 357 ± 22 MPa to over 600 ± 13 MPa with only 5% strain. The tensile fracture surfaces of the as-fabricated Fe/SiC composite and the as-fabricated pure iron samples are illustrated in Fig. 29c and

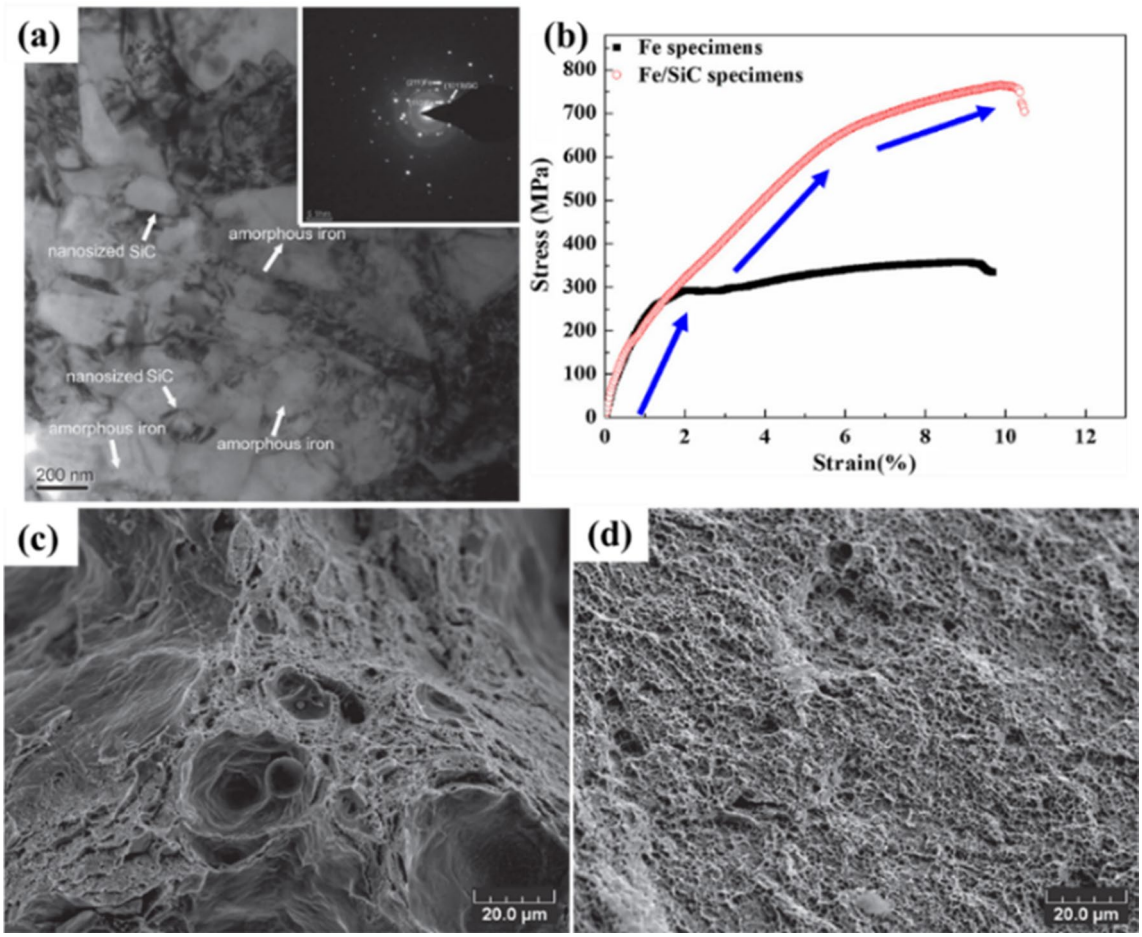

Fig. 29 **a** TEM image of cross section of SLMed Fe/SiC composite and the corresponding SAD patterns. **b** Stress–strain curves of as-fabricated Fe/SiC composite and pure Fe sample. SEM micrographs of the tensile fracture surfaces of SLMed: **c** Fe sample and **d** Fe/SiC sample [240]

d, respectively. The fracture surface of the Fe/SiC composite demonstrates a ductile failure, with evidence of plastic deformation, such as uniform dimples in the Fe matrix except for the brittle fracture of the scattered SiC particles (Fig. 29c). This behavior is quite different from the mixed failure mode of the pure iron specimen (Fig. 29d). The enhanced strength observed in the SLM-fabricated composite (compared to pure iron) is attributed to the role of hybrid nano-micro SiC particulates.

4.4 Fracture Behavior

The size and distribution, crack propagation after crack formation may influence the fracture behavior of the composites. The main types of fracture are trans-crystalline quasi-brittle, brittle fracture, inter-granular fracture, and ductile fracture [241]. The IMMC with high volume fraction of reinforcements may show the characteristic of brittle facture, because most of the load is taken by the reinforcements and the absorbed energy is small. There is no obvious deformation before a brittle fracture. In addition, ductile fractures develop following apparent deformation. Usually fracture strength, or breaking strength (the stress when the material fails or fracture) are used to measure the fracture behavior of metal [242]. The fracture characteristics of the IMMCs were found to significantly vary depending on the type and quantity of reinforcement additions in different stress and temperature [243]. Atomic structure and microstructure of matrix will also affect the fracture behavior of IMMCs [244]. In detail, dislocations traverse specific slip planes within a metal under the stress. In cases where obstacles, such as reinforcements or precipitates, penetrate the slip plane, a dislocation moving on this plane is compelled to interact with these obstacles [235, 245]. The dislocation, subjected to an applied shear stress τ, undergoes bowing between the obstacles within the slip plane, the shear stress required to bow the dislocation to a radius r is given by Eq. (5):

$$\tau = \frac{Gb}{2r}. \quad (5)$$

where G is the shear modulus, b is Burger's vector. This mechanism of dislocation bowing around particles is called Orowan bowing.

Feldshtein et al. [246] described influences of introduction of Al_2O_3 and ZrO_2 nano-particulates on the fracture stresses when flexing and compression. The results show that the ZrO_2 particles increase the stresses but Al_2O_3 particles are the opposite. The reason is that the ZrO_2 particles are distributed along the grain boundaries and inside the grains. Furthermore, the Al_2O_3 particles are distributed along the grain boundaries only and tend to form conglomerates. As a result, grain boundaries are weakened which lead to intergranular destruction. Moreover, intergranular fracture predominates in the composite with the addition of 1 mass% of Al_2O_3, but transcrystalline quasi-brittle fracture and viscous fracture in the ferrite component are also noted. The transcrystalline fracture predominates in the composite with the addition of 1 mass% of ZrO_2. Li et al. [247] investigated the influence of WC particle shape on the fracture mechanisms in WC-reinforced composites, emphasizing how particle morphology affects crack initiation. They found that cracks typically originate at the WC/Fe interface. The study noted that irregularly shaped WC particles, which contain bulges, transform into more spherical shapes under stress. These irregular shapes tend to concentrate stress, leading to brittle cracking. The interface between WC particles and the matrix was found to be extremely thin, ranging from 5 to 60 µm, which aids in stress transfer but also facilitates crack initiation at these points. The study concluded that composites with irregular WC shapes are more prone to stress-induced brittle cracking compared to those with spherical WC.

Moreover, the influence of different parameters on the mechanical properties of carbon nanotube (CNT) reinforced IMMCs was investigated by Ishraaq, using molecular dynamics methods [248]. A mathematical model was developed to predict that the mechanical properties of IMMCs change with the variation of CNT radius. Figure 30a shows

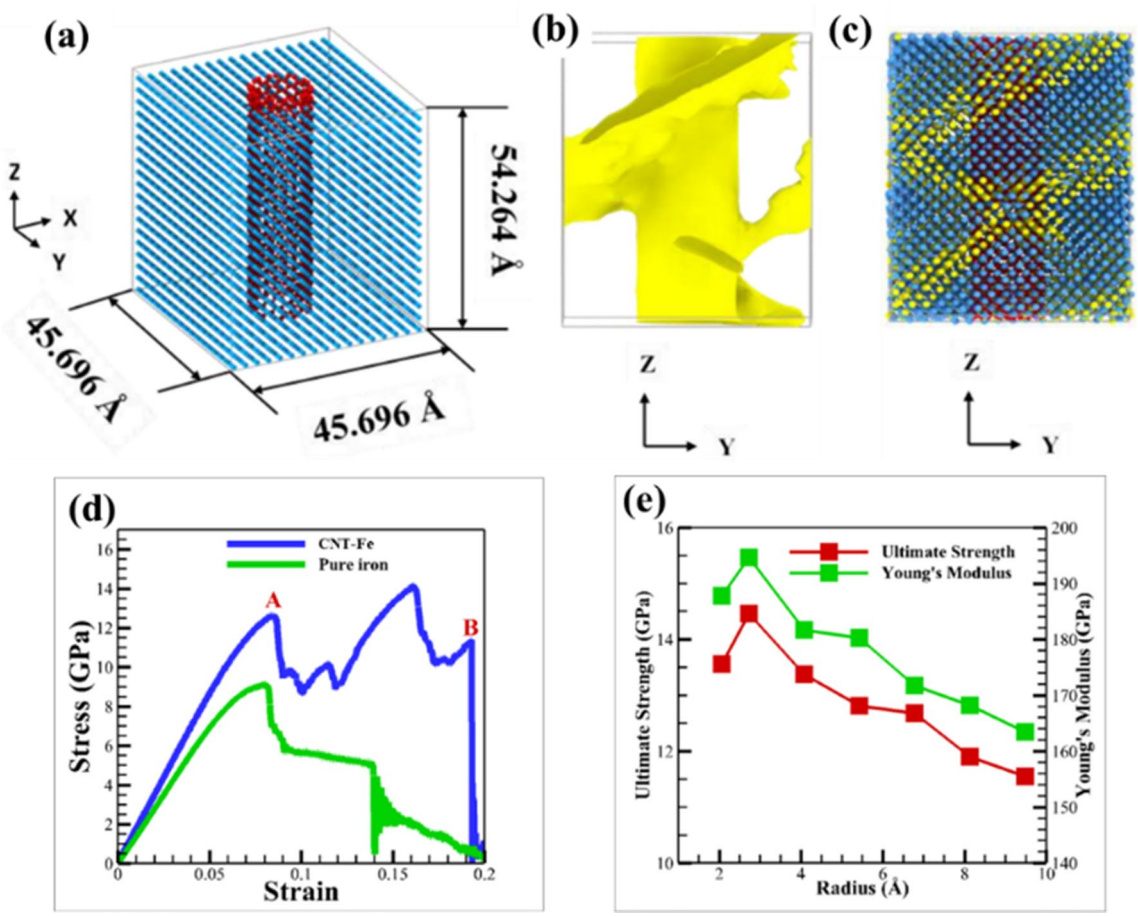

Fig. 30 **a** Schematic of CNT-IMMCs model (iron atoms are blue and carbon atoms are red), **b** state of the representative volume element (RVE) at 0.09 strain, **c** variation of atomic configuration along the slip direction, **d** stress–strain curves of the CNT-IMMC and pure iron, **e** change of ultimate strength and Young's modulus with different radius [248]

the overall view of the model, iron atoms are blue and CNT atoms are red. They found that 2.5 Å is the best size of CNT radius for fabricating IMMC having optimum combination of strength and stiffness through the simulation. Figure 30b and c explains the failure mechanical of the IMMC, the yellow covers all of the distorted unit cells form the bcc structure. From Fig. 30b, it can be seen that the Fe-matrix fails and the swelling propagates along the maximum shear stress plane (45°). This phenomenon demonstrates that the dislocations move near the interface and spread along the plane of 45°. In addition, the appearance of dislocations near the interface of matrix-fiber results in the failure of composites. Figure 30c demonstrates the atomic configuration change along the slip direction, and the blue atoms (bcc) change to yellow atoms (fcc or hcp). Figure 30d shows the tensile test simulation results of CNT-Fe and pure iron. The Fe-matrix and CNT fails at point A and B, respectively. The significant increase in strength of the IMMC is shown in this figure. Figure 30e illustrates the change of ultimate tensile strength and Young's modulus with different radius, and the data matches with the theoretical prediction closely. The optimum combination of mechanical properties reaches, when the radium of CNT is 2.73 Å.

5 Challenges and Future Directions

IMMCs have excellent mechanical properties that make them promising for various applications, whereas there some challenges that need to be addressed. The current challenges mainly include the agglomeration of reinforcement particles, the interfacial bonding problems between matrix and reinforcement phases, and material processing issue during their thermo-mechanical processing. Future research directions of IMMCs are expected to focus on developing novel manufacturing and processing methods, utilizing in situ reaction routines, and designing new alternative alloys.

5.1 Current Challenges

1. Achieving a uniform and dispersed distribution of reinforcement particles within the iron matrix is crucial for obtaining desirable mechanical properties. However, achieving a homogeneous distribution of reinforcements can be challenging due to the tendency of the agglomeration of reinforcement particles. This issue is rooted in the Gibbs free energy reduction in the whole system. Extensive research efforts need to be paid on tailoring the refinement and homogenization of the reinforcement phases.
2. The mechanical behavior and failure mode of IMMCs mainly depend on the bonding between reinforcement phase and the iron matrix. Therefore, achieving a strong interface between the reinforcement and the matrix is critical for efficient load transfer and avoiding debonding or particle pullout during mechanical loading. Developing effective bonding mechanisms and optimized processing techniques to enhance the interfacial bonding is a significant challenge.
3. IMMCs have shown promising properties at the laboratory scale, but scaling up production to industrial levels can be challenging. Thermo-mechanical processing of IMMCs in large scale remains a great challenge due to the high propensity of defects generated during processing. Moreover, ensuring consistent quality, reproducibility, and scalability of manufacturing processes for large-scale production is a significant obstacle that needs to be overcome for their widespread industrial applications.

5.2 Future Directions

Future work has to be carried out on three fronts (shown in Fig. 31):

1. Developing advanced manufacturing and processing techniques is crucial for the optimization of microstructure and mechanical properties of IMMCs. Novel manufacturing and material processing techniques are emerging as promising solutions to address the reinforcement phase agglomeration issue of IMMCs. Novel additive manufacturing technologies, such as selective laser melting, direct energy deposition, and liquid metal 3D printing can be applied to the fabrication of IMMCs. Moreover, ultrasonic dispersion technology, magnetic field and mechanical stirring can be applied during the fabrication of IMMCs.
2. Developing in situ fabrication processes (especially the liquid-state process) and producing reinforcement that is coherent or semi-coherent with the iron matrix are essential to improve the bonding quality between reinforcements and matrix. Designing suitable in situ reaction processes requires careful consideration of the system selection, the interface compatibility, and the reaction kinetics. Carbides, nitrides, oxides, and intermetallic compounds can be fabricated by identifying the possible reactions happening. Reactant's compositions and concentrations, temperature, and diffusion mechanism across reaction or bonding layers must be evaluated to determine the reaction kinetics. The distribution, quantity, size, and morphologies of the reinforcement phases should be tailored to realize the optimized mechanical properties of IMMCs.
3. Alternative alloy design integrated with machine learning technology would be a promising direction for the research of IMMCs. Machine learning models enable material space exploration only with a database repre-

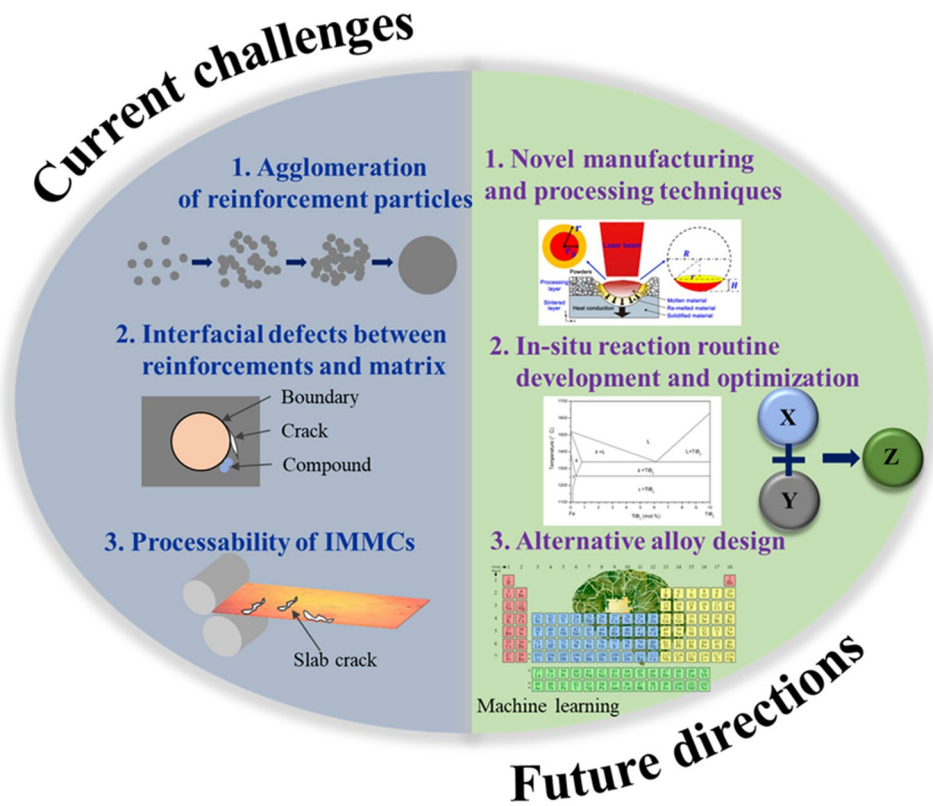

Fig. 31 Summary of current challenges and future directions of the research of IMMCs [112]

senting the relationship between descriptors of material and the properties. Gaussian process regression, radial basis function network, support vector machine, and deep neural network (DNN), can be utilized for finding desired combination of reinforcement and matrix phases within the vast material choices.

6 Summary and Conclusions

In this review paper, the available literature on IMMCs have been summarized and discussed to reflect the state-of-the-arts of the microstructural design strategies, fabrication methods, and engineering performance. Main conclusions can be drawn are:

1. Microstructural design of the IMMCs, including the selection of reinforcement, matrix phases, and the interface between them, play a critical role on their overall engineering performance and manufacturing processes. A variety of reinforcements can be incorporated into the iron matrix, including ceramic particles, fibers (carbon, ceramic, or metallic), and even 2D material such as graphene. Each type of reinforcement offers different advantages in terms of mechanical, thermal, and electrical properties. Microstructural features of the matrix, such as grain size, phase composition, and crystallographic texture, can be manipulated through strategies such as chemical alloying, heat treatment, and introduction of secondary phases. The interface between the reinforcements and matrix plays a crucial role in facilitating load transfer and determining the overall performance of composite. Interface type, geometry, and possible reactions happening should be controlled to ensure the overall performance of IMMCs.
2. The fabrication methods employed for IMMCs can be categorized into liquid-state processes, solid-state techniques, and gas-mixing methods. Liquid-state processes display attractive economic benefits and the potential for mass production. However, it is important to acknowledge that the floatation of reinforcements may occur during these processes due to their lower density compared to the iron, which deteriorates the strengthening effect of reinforcements. Solid-state processing techniques offer advantages in the production of complex structured materials and allow for specific combination of reinforcements and matrix. Additionally, the incorporating of powder processing techniques enables the fabrication of IMMC with a uniform distribution of reinforcements. Nevertheless, it is important to note that this type

of process faces certain challenges, including complex fabrication procedures, a higher incidence of material defects, increased costs, and reduced efficiency. The gas-mixing methods for preparing IMMCs have great potential for development due to their ability to control reaction kinetics. Generally, it is worth noting that the equipment utilized in this method is typically complex, and the preparation efficiency is relatively low. This suggests that further advancements are needed in the development of this method. By undertaking comparative analyses of various fabrication methods, valuable guidelines can be provided for the selection of appropriate processes, thereby achieving IMMCs with outstanding overall performance.

3. The mechanical properties (elastic modulus, tensile and fracture behavior, hardness and wear resistance) of IMMCs are reviewed. Essential factors, such as the volume fraction and distribution of the reinforcements, as well as the composition and microstructure of the composite, on the mechanical properties of IMMCs are discussed. In general, IMMCs exhibit improved mechanical properties compared to the unreinforced ones, primarily attributed to the presence of reinforcements. In detail, the presence of reinforcements in IMMCs can result in second phase strengthening and grain refinement strengthening effects, thereby enhancing the mechanical properties of IMMCs. Consequently, IMMCs exhibit a unique combination of mechanical properties that make them suitable for diverse applications, including automotive and aerospace components, cutting tools, and wear-resistant coatings.
4. The current challenges and future directions of IMMCs are summarized. The current challenges include issues such as the agglomeration of reinforcement particles, the presence of interfacial defects between reinforcements and matrix, as well as the vulnerability of cracking and sensitive processing window during the processing of IMMCs at industry scale. Consequently, future research directions are proposed to attempt these challenges. Novel manufacturing and processing techniques, in situ reaction fabrication methods, and machine learning assisted novel alloy and microstructure design may pave a way for resolving the current challenges and broadening the wide applications of IMMCs.

Acknowledgements Bo Mao acknowledges the funding support from the National Natural Science Foundation of China (No. 52101046). Shuangjie Chu appreciates the funding support from the National Key Research and Development Program of China (No. 2022YFB3705600).

Author contributions BM and SJC conceived the outline of the article and designed this study. SC searched for information. SC and BM wrote the manuscript. BM and SJC evaluated the data and revised the manuscript. All the authors have read and agreed to publish the manuscript.

Data Availability The raw/processed data required to reproduce these findings can be shared if necessary.

Declarations

Conflict of interest The authors declare that they have no known competing financial interests or personal relationships that could have appeared to influence the work reported in this paper.

References

[1] J. Morris Jr., Nat. Mater. **16**, 787 (2017)
[2] X. Li, Y.H. Tan, H.J. Willy, P. Wang, W. Lu, M. Cagirici, C.Y.A. Ong, T.S. Herng, J. Wei, J. Ding, Mater. Des. **178**, 107881 (2019)
[3] D. Raabe, B. Sun, A. Kwiatkowski Da Silva, B. Gault, H. Yen, K. Sedighiani, P. Thoudden Sukumar, I.R. Souza Filho, S. Katnagallu, E. Jägle, Metall. Mater. Trans. A **51**, 5517 (2020)
[4] Z.J. Xie, G. Han, W. Zhou, X. Wang, C. Shang, R. Misra, Scr. Mater. **155**, 164 (2018)
[5] X. Wang, H. Leng, B. Han, X. Wang, B. Hu, H. Luo, Acta Mater. **176**, 84 (2019)
[6] H. Zhang, H. Springer, R. Aparicio-Fernández, D. Raabe, Acta Mater. **118**, 187 (2016)
[7] R. Rana, *High-Performance Ferrous Alloys* (Springer, New York, 2021)
[8] Y. Wang, B. Mao, S. Chu, L. He, Y. Wang, H. Xing, G. Tian, H. Zhao, S. Wang, J. Zhang, Corros. Sci. **225**, 111592 (2023)
[9] Y. Wang, B. Mao, S. Chu, S. Chen, H. Xing, H. Zhao, S. Wang, Y. Wang, J. Zhang, B. Sun, J. Mater. Res. Technol. **24**, 8198 (2023)
[10] M. Commisso, C. Le Bourlot, F. Bonnet, O. Zanelatto, E. Maire, Materialia **6**, 100311 (2019)
[11] Z. Hadjem-Hamouche, K. Derrien, E. Héripré, J. Chevalier, Mater. Sci. Eng. A **724**, 594 (2018)
[12] Y. Li, M. Huang, J. Mech. Phys. Solids **121**, 313 (2018)
[13] B. Saha, G. Upadhyaya, J. Mater. Process. Technol. **36**, 363 (1993)
[14] M. Inoue, H. Nagao, K. Suganuma, K. Niihara, Mater. Sci. Eng. A **258**, 298 (1998)
[15] D. Lin, C.R. Liu, G.J. Cheng, Acta Mater. **80**, 183 (2014)
[16] B. Parveez, M. Wani, Tribol. Int. **159**, 106969 (2021)
[17] Y. Li, Y. Lu, W. Li, M. Khedr, H. Liu, X. Jin, Acta Mater. **158**, 79 (2018)
[18] M.S. Martínez, E.B. Becerril, J.L. Ruiz, A.C. Cuevas, *Metal Matrix Composites: Wetting and Infiltration* (Springer, New York, 2018)
[19] D. Guan, X. He, R. Zhang, X. Qu, Mater. Sci. Eng. A **705**, 231 (2017)
[20] B. Song, Z. Wang, Q. Yan, Y. Zhang, J. Zhang, C. Cai, Q. Wei, Y. Shi, Mater. Sci. Eng. A **707**, 478 (2017)
[21] A. Grairia, N.E. Beliardouh, M. Zahzouh, C. Nouveau, A. Besnard, Mater. Res. Express **5**, 116528 (2018)
[22] L. Zhong, F. Ye, Y. Xu, J. Li, Mater. Des. **54**, 564 (2014)
[23] K. Parashivamurthy, R. Kumar, S. Seetharamu, M. Chandrasekharaiah, J. Mater. Sci. **36**, 4519 (2001)
[24] K. Das, T.K. Bandyopadhyay, S. Das, J. Mater. Sci. **37**, 3881 (2002)
[25] F. Akhtar, Can. Metall. Q. **53**, 253 (2014)
[26] S. Xiang, S. Ren, Y. Liang, X. Zhang, Mater. Sci. Eng. A **768**, 138459 (2019)

[27] Y. Nishida, *Introduction to Metal Matrix Composites: Fabrication and Recycling* (Springer Science and Business Media, Berlin, 2013)
[28] D. Abolhasani, S.M.H. Seyedkashi, T.W. Hwang, Y.H. Moon, Mater. Sci. Eng. A **763**, 138161 (2019)
[29] U. Gökmen, Z. Özkan, U. Taşcı, S.B. Ocak, Phys. Scr. **97**, 055307 (2022)
[30] G. Hammes, K.J. Mucelin, P. da Costa, C.B. Gonçalves, R. Binder, R. Janssen, A.N. Klein, J.D.B. de Mello, Wear **376–377**, 1084 (2017)
[31] X.L. Li, C.H. Wang, L. Lu, J. Iron. Steel Res. Int. **19**, 60 (2012)
[32] Y. Zou, C. Tan, Z. Qiu, W. Ma, M. Kuang, D. Zeng, Addit. Manuf. **41**, 101971 (2021)
[33] Y. Lyu, Y. Sun, F. Jing, Ceram. Int. **41**, 10934 (2015)
[34] H. Chen, D. Gu, K. Kosiba, T. Lu, L. Deng, L. Xi, U. Kühn, Addit. Manuf. **35**, 101195 (2020)
[35] T. Gualtieri, A. Bandyopadhyay, Mater. Des. **139**, 419 (2018)
[36] J.C. Betts, J. Mater. Process. Technol. **209**, 5229 (2009)
[37] L. Zhong, Y. Xu, M. Hojamberdiev, J. Wang, J. Wang, Mater. Des. **32**, 3790 (2011)
[38] A. Farid, S. Guo, F.E. Cui, P. Feng, T. Lin, Mater. Lett. **61**, 189 (2007)
[39] B.P. Sharma, G. Rao, U.K. Vates, *In Advances in Industrial and Production Engineering* (Springer, New York, 2019), p.303
[40] J. Ru, H. He, Y. Jiang, R. Zhou, Y. Hua, J. Alloys Compd. **786**, 321 (2019)
[41] F.G. Alabtah, E. Mahdi, Compos. Struct. **266**, 113740 (2021)
[42] D. Min, W. Zhou, Y. Qing, F. Luo, D. Zhu, J. Alloys Compd. **744**, 629 (2018)
[43] R. Ishraaq, M. Rashid, S.M. Nahid, arXiv preprint arXiv:2102.05025 (2021)
[44] Y. Sui, M. Zhou, Y. Jiang, J. Alloys Compd. **741**, 1169 (2018)
[45] R. Aparicio-Fernández, H. Springer, A. Szczepaniak, H. Zhang, D. Raabe, Acta Mater. **107**, 38 (2016)
[46] J. Feizabadi, J.V. Khaki, M.H. Sabzevar, M. Sharifitabar, S.A. Sani, Mater. Des. **84**, 325 (2015)
[47] M. Hussain, V. Mandal, V. Kumar, A. Das, S. Ghosh, Opt. Laser Technol. **97**, 46 (2017)
[48] Y. Liang, Z. Han, Z. Zhang, X. Li, L. Ren, Mater. Des. **40**, 64 (2012)
[49] M. Dammak, M. Gaspérini, D. Barbier, Mater. Sci. Eng. A **616**, 123 (2014)
[50] H. Bai, L. Zhong, Z. Shang, Y. Xu, H. Wu, J. Bai, B. Cao, J. Wei, J. Alloys Compd. **768**, 340 (2018)
[51] P.W. Peters, J. Hemptenmacher, H. Schurmann, Compos. Sci. Technol. **70**, 1321 (2010)
[52] T. Vijayaram, S. Sulaiman, A. Hamouda, M. Ahmad, J. Mater. Process. Technol. **178**, 34 (2006)
[53] B.D. Agarwal, L.J. Broutman, K. Chandrashekhara, *Analysis and Performance of Fiber Composites* (Wiley, New Jercy, 2017)
[54] G. Garmong, L. Shepard, Metall. Trans. **2**, 175 (1971)
[55] L. Lassila, S. Garoushi, P.K. Vallittu, E. Säilynoja, J. Mech. Behav. Biomed. Mater. **60**, 331 (2016)
[56] S.A. Suarez, R.F. Gibson, C. Sun, S. Chaturvedi, Exp. Mech. **26**, 175 (1986)
[57] S. Bahl, Mater. Today: Proc. **39**, 317 (2021)
[58] H. Sueyoshi, T. Maruno, M. Asano, Y. Hirata, S. Sameshima, S. Uchida, S. Hamauzu, S. Kurita, Mater. Trans. **43**, 2866 (2002)
[59] H. Sueyoshi, K. Kume, R. Kurose, K. Hashinokuchi, S. Uchida, T. Inoue, Mater. Sci. Technol. **27**, 1347 (2011)
[60] M. Sakamoto, H.N. Liu, M. Nomura, K. Ogi, Wear **251**, 1414 (2001)
[61] S. Sahoo, Reinf. Plast. **65**, 101 (2021)
[62] A. Radhamani, H.C. Lau, S. Ramakrishna, Compos. Pt. A **114**, 170 (2018)
[63] R.J. Young, M.F. Liu, I.A. Kinloch, S.H. Li, X. Zhao, C. Valles, D.G. Papageorgiou, Compos. Sci. Technol. **154**, 110 (2018)
[64] Ö. Güler, N. Bağcı, J. Mater. Res. Technol. **9**, 6808 (2020)
[65] Y.C. Zhao, Y. Tang, M.C. Zhao, L. Liu, C. Gao, C. Shuai, R.C. Zeng, A. Atrens, Y. Lin, Adv. Eng. Mater. **21**, 1900314 (2019)
[66] L. Wang, J. Jin, P. Yang, S. Li, S. Tang, Y. Zong, Q. Peng, Comput. Mater. Sci. **191**, 110309 (2021)
[67] A. Mandal, J.K. Tiwari, N. Sathish, A.K. Srivastava, Mater. Sci. Eng. A **774**, 138936 (2020)
[68] F. Essa, A.H. Elsheikh, J. Yu, O.A. Elkady, B. Saleh, J. Mater. Res. Technol. **12**, 283 (2021)
[69] Y. Han, Y. Zhang, H. Jing, D. Lin, L. Zhao, L. Xu, P. Xin, Addit. Manuf. **34**, 101381 (2020)
[70] M. Liu, Y. Li, Z. Cui, Q. Yang, Mater. Charact. **156**, 109828 (2019)
[71] Y. Wang, J. Sun, T. Jiang, Y. Sun, S. Guo, Y. Liu, Acta Mater. **158**, 247 (2018)
[72] S. Oke, O. Ige, O. Falodun, M.R. Mphahlele, P. Olubambi, 2018 IOP Conference. Ser.: Mater. Sci. Eng. p. 012034
[73] A.K. Srivastava, K. Das, ISIJ Int. **49**, 1372 (2009)
[74] A.K. Srivastava, K. Das, Tribol. Int. **43**, 944 (2010)
[75] M. Huang, B. He, X. Wang, H. Yi, Scr. Mater. **99**, 13 (2015)
[76] W.H. Kan, G. Proust, V. Bhatia, L. Chang, K. Dolman, T. Lucey, X. Tang, J. Cairney, Wear **420**, 149 (2019)
[77] C. Loayza, D. Cardoso, D. Borges, A. Castro, A. Bozzi, M. Dos Reis, E. Braga, Mater. Des. **223**, 111169 (2022)
[78] K. Das, T. Bandyopadhyay, S. Chatterjee, J. Mater. Sci. **40**, 5007 (2005)
[79] E. Pagounis, V. Lindroos, M. Talvitie, Metall. Mater. Trans. A **27**, 4183 (1996)
[80] H. Besharatloo, M. Carpio, J.M. Cabrera, A.M. Mateo, G. Fargas, J.M. Wheeler, J.J. Roa, L. Llanes, Metals **10**, 1352 (2020)
[81] D. Gowtam, M. Ziyauddin, M. Mohape, S. Sontakke, V. Deshmukh, A. Shah, Int. J. Self-Propag. High Temp. Synth. **16**, 70 (2007)
[82] A.K. Srivastava, K. Das, Mater. Sci. Eng. A **516**, 1 (2009)
[83] B. Mao, S. Chu, S. Wang, Metals **10**, 1246 (2020)
[84] Z. Ni, Y. Sun, F. Xue, J. Bai, Y. Lu, Mater. Des. **32**, 1462 (2011)
[85] X. Wang, X. Sun, C. Song, H. Chen, S. Tong, W. Han, F. Pan, Acta Metall. Sin.-Engl. Lett. **32**, 746 (2019)
[86] B. Wang, G. Wang, R. Misra, H. Yi, Mater. Sci. Eng. A **812**, 141100 (2021)
[87] R. Han, G. Yang, X. Sun, G. Zhao, X. Liang, X. Zhu, Acta Metall. Sin.-Engl. Lett. **58**, 1589 (2022)
[88] H. Chen, D. Gu, H. Zhang, L. Xi, T. Lu, L. Deng, U. Kuehn, K. Kosiba, J. Mater. Process. Technol. **289**, 116959 (2021)
[89] B. Erice, C.C. Roth, D. Mohr, Mech. Mater. **116**, 11 (2018)
[90] A.K. Srivastava, K. Das, Mater. Lett. **62**, 3947 (2008)
[91] V. Pustovoit, Y.V. Dolgachev, Y.M. Dombrovskii, V. Duka, Met. Sci. Heat Treat. **62**, 369 (2020)
[92] X. Li, A. Ramazani, U. Prahl, W. Bleck, Mater. Charact. **142**, 179 (2018)
[93] D.J. Thomas, Int. J. Adv. Manuf. Technol. **64**, 1297 (2013)
[94] A. Do Nascimento, V. Ocelík, M. Ierardi, J.T.M. De Hosson, Surf. Coat. Technol. **202**, 4758 (2008)
[95] A. Kumar, K. Das, Open J. Met. **5**, 11 (2015)
[96] C. Tan, J. Zou, D. Wang, W. Ma, K. Zhou, Compos. Pt. B **236**, 109820 (2022)
[97] R. Guicheteau, J.L. Bobet, T. Miyasaki, A. Kawasaki, Y. Lu, J.F. Silvain, J. Alloys Compd. **724**, 711 (2017)
[98] R. Chen, B. Li, Y. Li, Z. Liu, X. Long, H. Yi, X. Wang, C. Jiang, M. Huang, Int. J. Fatigue **130**, 105276 (2020)
[99] A. Kennedy, D. Weston, M. Jones, Mater. Sci. Eng. A **316**, 32 (2001)
[100] S. Wu, Y. Qin, D. Fu, L. Fan, H. Chen, H. Hong, Ceram. Int. **46**, 15972 (2020)

[101] S. Lartigue-Korinek, M. Walls, N. Haneche, L. Cha, L. Mazerolles, F. Bonnet, Acta Mater. **98**, 297 (2015)
[102] R. Chen, B. Li, Y. Li, X. Wang, C. Jiang, M. Huang, Mater. Sci. Eng. A **823**, 141736 (2021)
[103] Q. Cen, Y. Jiang, R. Zhou, Y. Xu, J. Wang, J. Mater. Eng. Perform. **20**, 1447 (2011)
[104] J. Pelleg, Mater. Sci. Eng. A **269**, 225 (1999)
[105] Z. Li, H. Wei, Q. Shan, Y. Jiang, R. Zhou, J. Feng, J. Mater. Res. **31**, 2376 (2016)
[106] T. Sritharan, L. Chan, L. Tan, N. Hung, Mater. Charact. **47**, 75 (2001)
[107] Z. Luo, B. He, Y. Li, M. Huang, Metall. Mater. Trans. A **48**, 1981 (2017)
[108] D. Janicki, Surf. Coat. Technol. **406**, 126634 (2021)
[109] A. Safarian, M. Subaşi, Ç. Karataş, Int. J. Adv. Manuf. Technol. **89**, 2165 (2017)
[110] X. Zhao, Q. Wei, N. Gao, E. Zheng, Y. Shi, S. Yang, J. Mater. Process. Technol. **270**, 8 (2019)
[111] R. Licheri, R. Orru, G. Cao, A. Crippa, R. Scholz, Ceram. Int. **29**, 519 (2003)
[112] B. Li, Y. Liu, L. He, H. Cao, S. Gao, J. Li, Int. J. Cast. Metals Res. **23**, 211 (2010)
[113] H. Springer, R.A. Fernandez, M.J. Duarte, A. Kostka, D. Raabe, Acta Mater. **96**, 47 (2015)
[114] G. Manohar, A. Dey, K. Pandey, S. Maity, In AIP Conference. Proceedings. (AIP Publishing LLC, 2018), p. 020041
[115] M. Alsawat, T. Altalhi, N. Alotaibi, Z. Zaki, Results Phys. **13**, 102292 (2019)
[116] C. Lu, S. Ren, J. Wang, G. Yu, Key Eng. Mater. **562**, 837 (2013)
[117] M.R. Ghomashchi, A. Vikhrov, J. Mater. Process. Technol. **101**, 1 (2000)
[118] P. Li, X. Li, Y. Li, M. Gong, C. Tian, W. Tong, J. Mater. Eng. Perform. **28**, 7816 (2019)
[119] A. Anal, T. Bandyopadhyay, K. Das, J. Mater. Process. Technol. **172**, 70 (2006)
[120] Y. Pan, A. Liu, L. Huang, Y. Du, Y. Jin, X. Yang, J. Zhang, J. Alloys Compd. **784**, 519 (2019)
[121] A. Amosov, A. Samboruk, I. Yatsenko, V. Yatsenko, Int. J. Self-Propag. High-Temp. Synth. **28**, 10 (2019)
[122] H. Zhu, H. Wang, L. Ge, C. Shi, S. Wu, Trans. Nonferrous Met. Soc. China **17**, 590 (2007)
[123] S.S. Kumari, U.T.S. Pillai, B.C. Pai, J. Alloy. Compd. **509**, 2503 (2011)
[124] X. Chu, H. Che, P. Vo, R. Chakrabarty, B. Sun, J. Song, S. Yue, Surf. Coat. Technol. **324**, 353 (2017)
[125] E. Castrodeza, C. Mapelli, M. Vedani, S. Arnaboldi, P. Bassani, A. Tuissi, J. Mater. Eng. Perform. **18**, 484 (2009)
[126] S. Suresh, *Fundamentals of Metal-Matrix Composites* (Elsevier, Amsterdam, 2013)
[127] A. Kennedy, J. Wood, B. Weager, J. Mater. Sci. **35**, 2909 (2000)
[128] E. Carreno-Morelli, T. Cutard, R. Schaller, C. Bonjour, Mater. Sci. Eng. A **251**, 48 (1998)
[129] R. Voytovych, V. Bougiouri, N. Calderon, J. Narciso, N. Eustathopoulos, Acta Mater. **56**, 2237 (2008)
[130] L. Zhong, M. Hojamberdiev, F. Ye, H. Wu, Y. Xu, Ceram. Int. **39**, 731 (2013)
[131] H. Wang, Q. Jiang, B. Ma, Y. Wang, F. Zhao, J. Alloys Compd. **391**, 55 (2005)
[132] B. Qiu, S. Xing, Q. Dong, H. Liu, Tribol. Int. **142**, 105979 (2020)
[133] S. Rajagopal, J. Appl. Metalworking. **1**, 3 (1981)
[134] D. Stawarz, K. Kulkarni, R. Miclot, K. Iyer, Cast. Steel Weapon Compon. (1976)
[135] H. Uozumi, K. Kobayashi, K. Nakanishi, T. Matsunaga, K. Shinozaki, H. Sakamoto, T. Tsukada, C. Masuda, M. Yoshida, Mater. Sci. Eng. A **495**, 282 (2008)
[136] A. Maleki, B. Niroumand, A. Shafyei, Mater. Sci. Eng. A **428**, 135 (2006)
[137] R. Li, L. Liu, L. Zhang, J. Sun, Y. Shi, B. Yu, J. Mater. Sci. Technol. **33**, 404 (2017)
[138] S.J.S. Chelladurai, R. Arthanari, Surf. Rev. Lett. **26**, 1850125 (2019)
[139] B. Yao, Z. Zhou, Z. Chen, J. Wang, Steel Res. Int. **63**, 543 (2020)
[140] D. Lu, J. Wang, J. Yu, Y. Jiang, J. Wuhan, Univ. Technol.-Mat. Sci. Edit. **33**, 164 (2018)
[141] H. Khodaverdizadeh, B. Niroumand, Mater. Des. **32**, 4747 (2011)
[142] J. Zhu, W. Jiang, G. Li, F. Guan, Y. Yu, Z. Fan, J. Mater. Process. Technol. **283**, 116699 (2020)
[143] W. Jiang, J. Zhu, G. Li, F. Guan, Y. Yu, Z. Fan, J. Mater. Sci. Technol. **88**, 119 (2021)
[144] M. Vattur Sundaram, K. B. Surreddi, E. Hryha, A. Veiga, S. Berg, F. Castro, L. Nyborg, In European Powder Metallurgy Congress and Exhibition, Euro PM 2018; Bilbao Exhibition Centre (BEC) Bilbao; Spain; 14 October 2018 through 18 October 2018; Code 1568752020)
[145] R.M. German, P. Suri, S.J. Park, J. Mater. Sci. **44**, 1 (2009)
[146] J. Liu, X. Zhou, P. Tatarko, Q. Yuan, L. Zhang, H. Wang, Z. Huang, Q. Huang, J. Adv. Ceram. **9**, 5 (2020)
[147] P. Li, X. Li, Y. Li, M. Gong, W. Tong, In AIP Conference Proceedings (AIP Publishing LLC, 2018), p. 020012
[148] P. Persson, A.E. Jarfors, S. Savage, J. Mater. Process. Technol. **127**, 131 (2002)
[149] Y. Liu, Y. Zhang, S. Ortega, M. Ibáñez, K.H. Lim, A. Grau-Carbonell, S. Martí-Sánchez, K.M. Ng, J. Arbiol, M.V. Kovalenko, Nano Lett. **18**, 2557 (2018)
[150] P. Ninpetch, A. Luechaisirikul, M. Morakotjinda, T. Yotkaew, R. Kratait ong, N. Tosangthum, S. Mahathanabodee, R. Tongsri, Mater. Today Proc. **5**, 9409 (2018)
[151] A. Mertens, S. Reginster, Q. Contrepois, T. Dormal, O. Lemaire, Mater. Sci. Forum **783**, 898 (2014)
[152] S. Dadbakhsh, R. Mertens, L. Hao, J. Van Humbeeck, J.P. Kruth, Adv. Eng. Mater. **21**, 1801244 (2019)
[153] M. Wilhelm, K. Wissenbach, A. Gasser, D.E. Patent, 19649865C1, (1996)
[154] C.Y. Yap, C.K. Chua, Z.L. Dong, Z.H. Liu, D.Q. Zhang, L.E. Loh, S.L. Sing, Appl. Phys. Rev. **2**, 041101 (2015)
[155] B. AlMangour, Y.K. Kim, D. Grzesiak, K.A. Lee, Compos. Pt. B-Eng. **156**, 51 (2019)
[156] B. AlMangour, D.J.M. Grzesiak, Mater. Des. **104**, 141 (2016)
[157] S. Huang, Q. Chen, L. Ji, K. Wang, G. Huang, Acta Metall. Sin.-Engl. Lett. **37**, 196 (2024)
[158] N. Kang, W. Ma, L. Heraud, M. El Mansori, F. Li, M. Liu, H. Liao, Addit. Manuf. **22**, 104 (2018)
[159] E. Kim, K. Lee, Y. Moon, J. Mater. Process. Technol. **105**, 42 (2000)
[160] F. Qiu, H. Zhang, C.L. Li, Z.F. Wang, F. Chang, H.Y. Yang, X. Han, Q.C. Jiang, Mater. Sci. Eng. A **819**, 141485 (2021)
[161] C.L. Atwood, Rapid Prototyping J. **102**, 103 (1997)
[162] L. Niu, M. Hojamberdiev, Y. Xu, J. Mater. Process. Technol. **210**, 1986 (2010)
[163] Z. Mei, Y. Yan, K. Cui, Mater. Lett. **57**, 3175 (2003)
[164] C. Wang, H. Gao, Y. Dai, X. Ruan, J. Shen, J. Wang, B. Sun, J. Alloys Compd. **490**, L9 (2010)
[165] A. Ramanathan, P.K. Krishnan, R. Muraliraja, J. Manuf. Process. **42**, 213 (2019)
[166] S. Sahoo, B.B. Jha, A. Mandal, Mater. Sci. Technol. **37**, 1153 (2021)
[167] P. Jha, P. Gupta, D. Kumar, O. Parkash, J. Compos. Mater. **48**, 2107 (2014)
[168] A. Kumar, M. Banerjee, U. Pandel, Powder Technol. **331**, 41 (2018)

[169] R. Bhattacharyya, A. Iqbal, T. Gaur, P. Gupta, Mater. Today Proc. **38**, 305 (2021)
[170] A.A. Cavalheiro, Powder Metallurgy, (Intechopen, London, 2018), pp. 45–63
[171] B. Meher, R. Saha, D. Chaira, J. Alloys Compd. **872**, 159688 (2021)
[172] M. Godec, B.Š Batič, D. Mandrino, A. Nagode, V. Leskovšek, S.D. Škapin, M. Jenko, Mater. Charact. **61**, 452 (2010)
[173] K. Sairam, J. Sonber, T.C. Murthy, C. Subramanian, R. Fotedar, P. Nanekar, R. Hubli, Int. J. Refract. Met. Hard Mater. **42**, 185 (2014)
[174] B. Li, Y. Liu, J. Li, H. Cao, L. He, J. Mater. Process. Technol. **210**, 91 (2010)
[175] M. Radajewski, S. Decker, L. Krüger, Measurement **147**, 106863 (2019)
[176] A. Mercier, F. Adam, D. Labrousse, B. Revol, A. Pasko, F. Mazaleyrat, EPE J. **29**, 161 (2019)
[177] B. Klotz, K. Cho, R. J. Dowding, R. D. Sisson Jr, in *25th Annual Conference on Composites, Advanced Ceramics, Materials, and Structures: B: Ceramic Engineering and Science Proceedings*, (Wiley Online Library, 2001), p. 27
[178] L. Huang, Y. Pan, J. Zhang, A. Liu, Y. Du, F. Luo, J. Mater. Res. Technol. **9**, 6116 (2020)
[179] B. Li, Y. Liu, H. Cao, L. He, J. Li, Mater. Lett. **63**, 2010 (2009)
[180] I.P. Borovinskaya, A.A. Gromov, E.A. Levashov, Y.M. Maksimov, A.S. Mukasyan, A.S. Rogachev, *Concise Encyclopedia of Self-Propagating High-Temperature Synthesis: History, Theory, Technology, and Products* (Elsevier, Amsterdam, 2017)
[181] E. Levashov, A. Mukasyan, A. Rogachev, D. Shtansky, Int. Mater. Rev. **62**, 203 (2017)
[182] M.K. Ziatdinov, I. Shatokhin, L. Leont'ev, Steel Transl. **48**, 269 (2018)
[183] G. Wang, Y. Li, Y. Gao, L. Niu, Wuhan Univ. Technol.-Mater. Sci. Ed. **34**, 769 (2019)
[184] Z. Zou, Y. Wu, C. Yin, X. Li, Wuhan Univ. Technol.-Mater. Sci. Ed. **22**, 706 (2007)
[185] S. S. Kalambaeva, E. Korosteleva,G. Pribytkov, in *2014 International Conference on Mechanical Engineering, Automation and Control Systems (MEACS)*, (IEEE 2014), p. 1
[186] Y. Yang, H. Wang, Y. Liang, R. Zhao, Q. Jiang, Mater. Sci. Eng. A **445**, 398 (2007)
[187] E. Olejnik, J. Sobczak, M. Szala, P. Kurtyka, T. Tokarski, A. Janas, J. Mater. Process. Technol. **308**, 117688 (2022)
[188] M. Aydin, R. Gürler, M. Türker, Phys. Metals Metallogr. **107**, 206 (2009)
[189] Ö. ESKi, M.A.M. Elhemsheri, J. Glob. Sci. Research **6**, 1128 (2021)
[190] H. Klaasen, J. Kübarsepp, A. Laansoo, M. Viljus, Int. J. Refract. Met. Hard Mater. **28**, 580 (2010)
[191] H. Kejanli, Adv. Compos. Lett. **29**, 2633366X20917983 (2020)
[192] E. Akca, A. Gürsel, Period. Eng. Nat. Sci. **3** (2015)
[193] M.N. Avettand-Fènoël, K. Naji, P. Pouligny, J. Manuf. Process. **45**, 557 (2019)
[194] M. Hasan, J. Zhao, Z. Huang, L. Chang, H. Zhou, Z. Jiang, Fusion Eng. Des. **133**, 39 (2018)
[195] M. Hasan, J. Zhao, Z. Huang, D. Wei, Z. Jiang, Int. J. Adv. Manuf. Technol. **103**, 3247 (2019)
[196] A. Rahimi-Vahedi, M. Adeli, H. Saghafian, Surf. Coat. Technol. **347**, 217 (2018)
[197] S. Dayanand, B. S. Babu, in *IOP Conf. Ser.: Mater. Sci. Eng.* (IOP Publishing, 2020), p. 012038
[198] H. Zhu, K. Dong, H. Wang, J. Huang, J. Li, Z. Xie, Powder Technol. **246**, 456 (2013)
[199] H. Zhu, B. Hua, J. Huang, J. Li, G. Wang, Z. Xie, Tribol.- Mater. Surf. Interfaces **8**, 165 (2014)
[200] R. Shashanka, D. Chaira, Powder Technol. **278**, 35 (2015)
[201] F. Saba, E. Kabiri, J.V. Khaki, M.H. Sabzevar, Powder Technol. **288**, 76 (2016)
[202] S.R. Oke, O.O. Ige, O.E. Falodun, A.M. Okoro, M.R. Mphahlele, P.A. Olubambi, Int. J. Adv. Manuf. Technol. **102**, 3271 (2019)
[203] M.J. Koczak, K.S. Kumar, U.S. Patent 4,808,372, 28 (1989)
[204] P. Sahoo, M.J. Koczak, Mater. Sci. Eng. A **131**, 69 (1991)
[205] C. Cui, R. Wu, Y. Li, Y. Shen, J. Mater. Process. Technol. **100**, 36 (2000)
[206] J. Haibo, K. Chen, Z. Heping, S. Agathopoulos, O. Fabrichnaya, J. Ferreira, J. Cryst. Growth **281**, 639 (2005)
[207] A. Singer, S. Ozbek, Powder Metall. **28**, 72 (1985)
[208] R. Della Gatta, A. Viscusi, A.S. Perna, A. Caraviello, A. Astarita, Mater. Manuf. Process. **36**, 281 (2021)
[209] T. Lampke, B. Wielage, H. Pokhmurska, C. Rupprecht, S. Schuberth, R. Drehmann, F. Schreiber, Surf. Coat. Technol. **205**, 3671 (2011)
[210] S.A. Alidokht, P. Vo, S. Yue, R.R. Chromik, Wear **376**, 566 (2017)
[211] M. Ksiazek, L. Boron, M. Radecka, M. Richert, A. Tchorz, J. Mater. Eng. Perform. **25**, 502 (2016)
[212] Z. Chu, F. Wei, X. Zheng, C. Zhang, Y. Yang, J. Alloys Compd. **785**, 206 (2019)
[213] R. Sekhar, T. Singh, J. Mater. Res. Technol. **4**, 197 (2015)
[214] W.H. Kan, C. Albino, D. Dias-da-Costa, K. Dolman, T. Lucey, X. Tang, L. Chang, G. Proust, J. Cairney, Mater. Charact. **136**, 196 (2018)
[215] G. Tian, Y. Xu, L. Fu, B. Mao, S. Zhao, Y. Wang, A. Shan, Mater. Sci. Eng. A **893**, 146133 (2024)
[216] Y. Zhang, Y. Wu, Y. Tang, J. Ma, B. Mao, Y. Xue, H. Xing, J. Zhang, B. Sun, J. Mater. Sci. Technol. **177**, 1 (2024)
[217] D.R. Askeland, P.P. Phulé, W.J. Wright, D. Bhattacharya, *The Science and Engineering of Materials* (Springer, London, 2003)
[218] J. Li, B. Zong, Y. Wang, W. Zhuang, Mater. Sci. Eng. A **527**, 7545 (2010)
[219] L. Sun, Y.M. Wu, Z.P. Huang, J.X. Wang, Acta Mech. Sin. **20**, 676 (2004)
[220] X. Zhang, T. Yang, J. Liu, X. Luo, J. Wang, J. Mater. Sci. **45**, 3457 (2010)
[221] Y. Hua, L. Gu, Compos. Pt. B **45**, 1464 (2013)
[222] S. Chen, P. Seda, M. Krugla, A. Rijkenberg, Mater. Sci. Technol. **32**, 992 (2016)
[223] R. Xiong, H. Kwon, G. Karthik, G.H. Gu, P. Asghari-Rad, S. Son, E.S. Kim, H.S. Kim, Mater. Lett. **303**, 130510 (2021)
[224] R. Rana, C. Liu, Can. Metall. Q. **53**, 300 (2014)
[225] B. Mao, X. Zhang, P.L. Menezes, Y. Liao, Materialia **8**, 100444 (2019)
[226] P. Zhang, S. Zeng, Z. Zhang, W. Li, Res. Dev. **10**, 374 (2013)
[227] A. Siddaiah, B. Mao, Y. Liao, P.L. Menezes, Surf. Coat. Technol. **351**, 188 (2018)
[228] B. Mao, A. Siddaiah, P.L. Menezes, Y. Liao, J. Mater. Process. Technol. **257**, 227 (2018)
[229] M. Razavi, M.R. Rahimipour, A.H. Rajabi-Zamani, Mater. Sci. Eng. A **454**, 144 (2007)
[230] P. Gupta, D. Kumar, O. Parkash, A. Jha, J. Compos. **2014**, 1 (2014)
[231] H. Bai, L. Zhong, P. Cui, Z. Shang, Z. Lv, Y. Xu, Vacuum **176**, 109302 (2020)
[232] Z. Zhang, Y. Chen, Y. Zhang, K. Gao, L. Zuo, Y. Qi, Y. Wei, J. Alloys Compd. **704**, 260 (2017)
[233] Z. Liao, X. Huang, F. Zhang, Z. Li, S. Chen, Q. Shan, Int. J. Refract. Met. Hard Mater. **114**, 106265 (2023)
[234] S. Wang, D. Shu, P. Shi, X. Zhang, B. Mao, D. Wang, P.K. Liaw, B. Sun, J. Mater. Sci. Technol. **187**, 72 (2024)
[235] X. Zhang, B. Mao, Y. Liao, Y. Zheng, J. Mater. Res. **35**, 1 (2020)

[236] M. Liu, H. Hu, J. Tian, G. Xu, Acta Metall. Sin. **57**, 749 (2020)
[237] K. Parashivamurthy, P. Sampathkumaran, S. Seetharamu, Proceedings of International and INCCOM-6 Conference on Future Trends in Composite Materials and Processing, 665 (2008)
[238] S. Zhao, X. Shen, J. Yang, W. Teng, Y. Wang, Opt. Laser Technol. **103**, 239 (2018)
[239] Y. Wang, C. Zhang, Y. Zong, H. Yang, Adv. Compos. Mater. **22**, 299 (2013)
[240] B. Song, S. Dong, P. Coddet, G. Zhou, S. Ouyang, H. Liao, C. Coddet, J. Alloys Compd. **579**, 415 (2013)
[241] R.E. Smallman, R.J. Bishop, *Modern physical metallurgy and materials engineering*, (Butterworth-Heinemann, 1999)
[242] B. Rabin, R. German, Metall. Trans. A **19**, 1523 (1988)
[243] G. Królczyk, E. Feldshtein, L. Dyachkova, M. Michalski, T. Baranowski, R. Chudy, Materials **13**, 2892 (2020)
[244] M. Şimşir, J. Mater. Sci. **42**, 6701 (2007)
[245] B. Mao, Dissertation, University of Nevada, (2020)
[246] E.E. Feldshtein, L.N. Dyachkova, G.M. Królczyk, Mater. Sci. Eng. A **756**, 455 (2019)
[247] Z. Li, P. Wang, Q. Shan, Y. Jiang, H. Wei, J. Tan, Materials **11**, 984 (2018)
[248] R. Ishraaq, S.M. Nahid, S. Chhetri, O. Gautam, A. Afsar, Comput. Mater. Sci. **174**, 109486 (2020)

Springer Nature or its licensor (e.g. a society or other partner) holds exclusive rights to this article under a publishing agreement with the author(s) or other rightsholder(s); author self-archiving of the accepted manuscript version of this article is solely governed by the terms of such publishing agreement and applicable law.